Investigations of the Ionospheric Alfvén Resonator at High Latitudes of both Northern and Southern Hemisphere

A Thesis submitted for the degree of Doctor of Philosophy

in the Department of Physics and Astronomy

The University of Leicester, UK

By

Kai Yuan

October 2011

ABSTRACT

Investigations of the Ionospheric Alfvén Resonator at High Latitudes of both Northern and Southern Hemisphere

Kai Yuan

In order to characterize the features of the Ionospheric Alfvén Resonator (IAR) at high latitudes in both northern and southern hemispheres, both data interpretation and numerical computation are presented. Four IAR events observed by the pulsation magnetometer at Sodankylä in a single month were statistically analysed. It was found that the IAR eigenfrequency separations fluctuate with time. The fluctuation was dominated by plasma density perturbation in the ionosphere. Also, a single IAR event observed by five pulsation magnetometers simultaneously was analysed. The analysis showed the eigenfrequencies of the single IAR detected at different locations are different. Additionally, the eigenfrequency shifts were found to differ at different locations. It indicates that the horizontal scale of a single IAR event could be up to thousands of kilometres. The horizontal structure of the IAR in a large scale is non-uniform. Also, the study has revealed that the visibility of the Spectrum Resonance Structure (SRS) strongly depends on the fluctuation rate of the eigenfrequency separations. Moreover, the first study of IARs in Antarctica was carried out. The IAR occurrence and the relation with the solar activities were investigated statistically.

In addition, a numerical model was introduced in this thesis. Based on this model the boundary condition dependence of the IAR was investigated. According to the study the detected eigenfrequencies, the spatial structures of the field and the ratio between the intensities of the total current and the source current strongly depend on the ratio between the wave conductivity and the height integrated Pedersen conductivity in the E region. Also, the numerical study in this thesis has revealed that the eigenfrequency shifts respond to the different features of plasma density perturbations in different ways. The possibility of estimating the plasma density perturbation continuously from the IAR eigenfrequencies observed on the ground is illustrated.

CONTENTS LIST

Chapter 1. Introduction

1.1 The Solar-Terrestrial System

Physical processes in Solar-Terrestrial system are important for human technologies, especially for communications and radio techniques [Lanzerotti et al., 1997; Song et al, 2001]. Also, space weather could affect human health. For example, the ultraviolet radiation intensity could enhance when the Sun is more active. The enhanced ultraviolet radiation could lead to skin cancer. Thus in order to develop communication technologies, protect electronic equipment against bad space weather and investigate how space weather affects human health, it is necessary to explore and study the Solar-Terrestrial system.

Fig 1.1 illustrates the main features of Solar-Terrestrial system. It can be seen that the whole system is strongly affected by solar activities, e.g., the climate responds to solar activity variations [Bond et al., 2001; Laut, 2003; Haigh, 1996]. Also, the geomagnetic field responds to solar activity.

Normally the sunspot number is utilized to denote the level of the activity of the Sun. When the Sun becomes more active, the sunspot number rises, and vice versa. The

sunspot number variation was monitored systematically since the 17^{th} century. According to the observation and the long-term record of the sunspot number, there is a periodic variation of solar activities. The period of the variation is about 10.7 years. It is considered to be 11-year period approximately.

The periodic solar variation is called the ‘solar cycle’ or ‘solar activity magnetic cycle’. During a solar cycle, there is a solar minimum and solar maximum. Solar minimum means the Sun reaches the quietest phase of a solar cycle. In the year of a solar minimum, the sunspot number reaches the minimum of the solar cycle. Solar maximum means the Sun reaches the most active phase of a solar cycle. In the year of solar maximum, the sunspot number reaches the maximum. Fig 1.2 illustrates a very well-known plot called ‘butterfly diagram’. The diagram shows the latitudes of sunspots versus time. The solar cycles are quite clear on the diagram. Each solar cycle, which looks like a butterfly, lasts about 11 years. However, it could be shorter or longer. For a single ‘butterfly’, the solar minimum occurs at the end of the 11 years, and the solar maximum occur in the brighter zone of the butterfly, which is in a year around the middle of the butterfly. The solar-terrestrial system responds periodically to solar cycles.

The Sun keeps ejecting charged particles into space from its upper atmosphere. The stream of the charged particles is called ‘solar wind’. The geomagnetic field responds to solar activities via solar wind and interplanetary magnetic field. Due to the solar radiation and the interaction between the geomagnetic field and the solar wind, the magnetosphere and the ionosphere are formed.

1.2 Magnetosphere, Ionosphere and Magnetosphere-Ionosphere Coupling

Without any external forcing the geomagnetic field would be approximately dipolar.

However, as the solar wind flows towards the earth it compresses the magnetic field lines on the sunward side and causes the geomagnetic field to stretch out into a comet-like tail on the anti-Sunward side. This process creates a cavity called the magnetosphere. The cavity shelters the planet surface from high-energy charged particles from both the Sun and outside the solar system. Charged particles in the solar wind or interplanetary space are able to be trapped in the modified geomagnetic field and this is one of the sources of the plasma of the magnetosphere. The structure of Earth's magnetosphere is shown in Fig 1.3. Various and complex space plasma processes occur in the magnetosphere, e.g., particle accelerations related to nonlinear processes during the magnetic reconnection.

Below the magnetosphere there is another ionised layer named 'ionosphere'. UV radiation from the Sun partially ionizes the neutral gas in the upper atmosphere of the Earth. The ionized gas mixed with neutral gas forms the ionosphere. Approximately the ionosphere lies in the altitude range, 70km-1500km. Generally the ionosphere could be divided into D layer, E layer and F layer. Furthermore, the F layer is divided into F1 layer and F2 layer in daytime. F1 layer deforms at night, F2 layer remains. The percentage of charged particles increases with altitude, while the percentage of the neutral particles decreases with altitude up to the F peak. There is no clear boundary between the magnetosphere and the ionosphere. Normally the magnetosphere is considered to be fully ionized and the ionosphere is partially ionized. The ionosphere exchanges mass and energy with the magnetosphere and the lower layers of the atmosphere. Also, the high frequency radio waves for distant communications could be reflected in order to reach the destination far beyond its place of departure. The ionospheric conditions dominate the reflection of the radio waves. Also, the ionosphere involves climate change [Gulyaeva and Gulyaev, 1993; Lastovicka et al., 2008], e.g., thermal contraction in the ionosphere caused by the increase of the greenhouse gas increase. Thus the physical processes in the ionosphere are quite important for space weather forecast, communications and scientific research on climate change.

There are several techniques that are used to monitor the ionosphere. Generally those techniques could be divided into two types, one is remote sensing, and the other one is in-situ observation. Rocket and low-orbiting satellites are in-situ observation methods.

There are several frequently used methods of remote sensing including ionosonde, ground based radar observations, satellite tomography, cosmic ray absorption and pulsation or searchcoil magnetometers. Ionosondes are utilized to detect the plasma density below the peak of F2 layer; ground based radars detect ionospheric electrodynamics; satellites tomography detects the plasma density profile on the path between the ground station and the satellite; searchcoil and pulsation magnetometers detect the magnetic field on the ground, some ionospheric parameters could be worked out from the magnetometer data, such as calculating the effective plasma density or size of Ionospheric Alfvén Resonators (IAR) based on the eigenfrequencies detected by pulsation magnetometers [Hebden et al., 2005], thus it is an indirect remote sensing method.

Since Alfvén first predict the existence of Alfvén waves theoretically [Alfvén, 1942], Alfvén waves were found to be quite important in dynamic processes in space plasma physics. Alfvén waves are involved a lot of space dynamic processes including solar activities, magnetospheric processes, interplanetary processes, planetary processes and ionospheric dynamics [Velli and Pruneti, 1997; Cummings, 1969; Belcher, 1969; Goertz, 1984; Orlowski, 1992].

According to traditional theories of magnetohydrodynamics (MHD), Alfvén waves just propagate in magnetized plasma. The plasma particles oscillate perpendicular to the magnetic field line, which is like acoustic waves. However, the restoring force for Alfvén waves is provided by magnetic tension force [Boyd, 1969].

In recent decades, the traditional MHD theories of Alfvén waves were challenged by both theories and observations. In traditional theories, the mass of electrons was ignored. The electrons were treated as massless fluid. Kinetic effects of the electrons were neglected in the traditional MHD theory. The initial effects of the electrons were not taken into account. Thus there is no electric field components parallel to the magnetic field to balance the force on the electrons. In other words, the electrons could accelerate without any force. However, parallel electric field components were detected with

Alfvén waves simultaneously by satellites. Those Alfvénic waves were named Kinetic Alfvén Waves (KAW) and Inertial Alfvén Waves (IAW). For non-parallel propagations, the parallel electric field forces of KAW and IAW are balanced by thermal pressures and electron inertial, respectively. Those waves play very important roles in coupling the ionosphere and the magnetosphere via IARs [Lysak and Song, 2008]. Thus IARs attracted a lot of interests in studying the coupling mechanics and dynamics.

According to theories of waves [Hiroes and Lonngren, 1985], waves are reflected at the interface between two different media. In an inhomogeneous medium, the wave could be reflected everywhere due to the gradient of the wave velocity. Ideally the plasma density profile above the F2 peak of the ionosphere decrease exponentially. According to equation 1.1, the Alfvén velocity increases with altitude above the F2 peak.

$$V_A = \frac{B}{\sqrt{\mu_0 m_i n_i}} \tag{1.1}$$

where μ_0 is the vacuum permeability, B is the intensity of the geomagnetic field, m_i is the mean mass of ions and n_i is the ion number density. Thus the Alfvén waves could be reflected above the F2 peak of the ionosphere. When the Alfvén waves travelling downwards reach the Pedersen conductive layer, the wave field drives the Pedersen current in the conductive layer. The Pedersen current could stimulate Alfvén waves propagating upwards. Thus the Pedersen conductive layer could reflect Alfvén waves. The two reflective layers and the space in between form a resonance cavity which could trap the Alfvén waves. Resonances occur in the resonance cavities when the energy feed into the cavity is greater than the energy loss.

The Earth's atmosphere and outer space continuously exchange mass and energy with each other. Most of the exchange processes occur in the ionosphere and the magnetosphere. The ionosphere and the magnetosphere form a whole dynamic system. Thus the coupling processes and dynamics between the magnetosphere and the ionosphere are important for the interaction between the Earth and the space. The geomagnetic field lines connect the ionosphere and the magnetosphere at high latitudes.

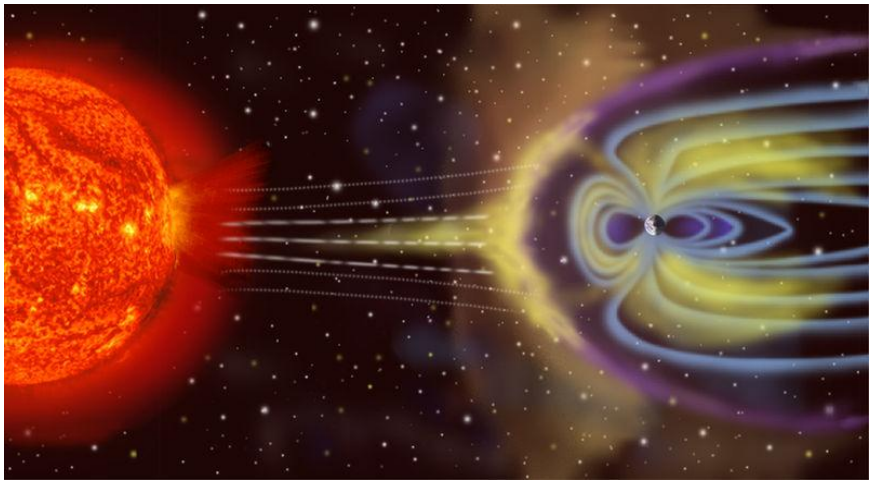

Fig 1.1 The structure of Solar-Terrestrial system. (http://sec.gsfc.nasa.gov/popscise.jpg)

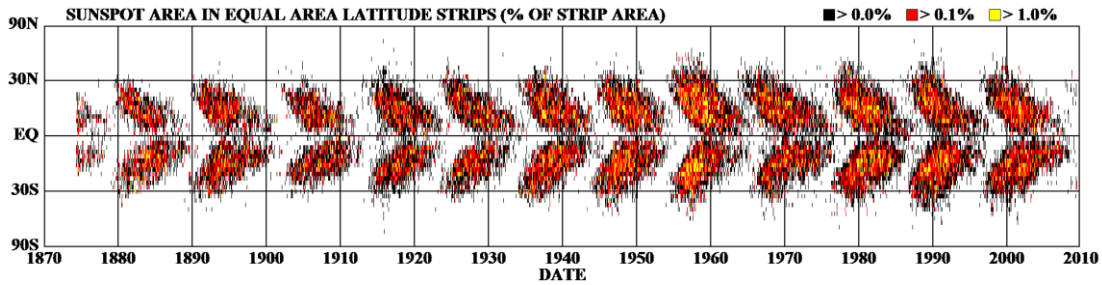

Fig 1.2 Butterfly diagram. The plot shows the latitudes of sunspots versus time.

(Author: David Hathaway, NASA Marshall Space Flight Center, http://solarscience.msfc.nasa.gov)

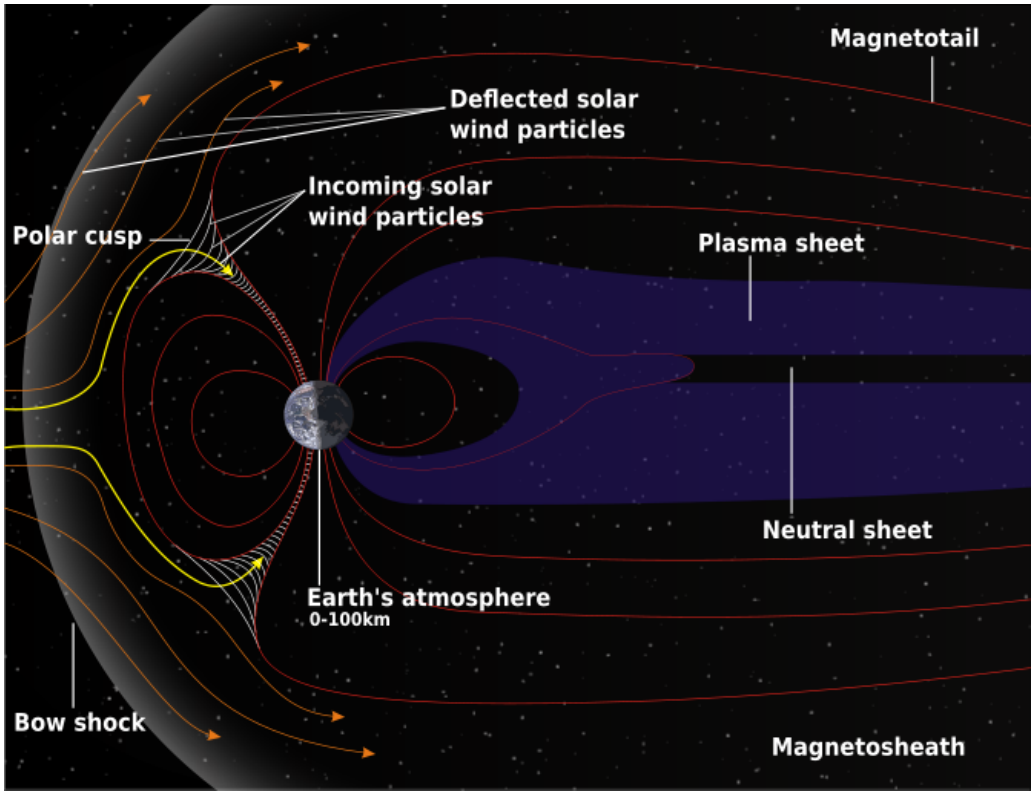

Fig 1.3 The structure of Earth's magnetosphere. The plot was created by NASA. (http://science.nasa.gov/newhome/headlines/guntersville98/images/mag_sketch_633.jpg).

Thus various magnetosphere-ionosphere coupling (M-I coupling) processes occur along the field line in high latitude regions. The ionospheric Alfvén resonator (IAR) which is the focus of this thesis plays a very important role in M-I coupling. For example, the IAR accelerates the charged particles in the magnetosphere at high latitudes [Chaston et al., 2002]. Also, the IAR could reflect the change of ionospheric condition caused by certain processes, e.g., substorms [Parent et al., 2010].

1.3 Scientific Aims and Outlines

Basically there are two parts of study in the thesis. The one is data interpretation and the other one is numerical modelling. The data collected by the Finnish pulsation magnetometer network will be surveyed and statistically investigated to study the IAR eigenfrequency separation variations as well as the dominant factors influencing the variations. The data obtained by the pulsation magnetometer at Halley Bay Station in Antarctica was also surveyed to characterize the features of IARs occurred at high latitudes of southern hemisphere. The features were qualitatively compared with the features of the IARs of northern hemisphere.

In order to investigate how the eigenfrequency separation variations respond to the local ionospheric plasma density perturbations, a one dimensional numerical model will be introduced. The boundary condition dependence of the IAR will be investigated based on this model. Also, the relation between the IAR eigenfrequency shifts and the plasma density perturbations will be investigated qualitatively by numerical computation.

The main scientific aim for the studies in this thesis is characterizing the features of IARs at high latitudes in both northern and southern hemisphere. Additionally, this thesis is trying to develop a new skill to estimate the plasma density profile variation

above the F2 peak based on the data obtained on the ground. The current methods to detect the plasma density profile above the F2 peak are incoherent scatter radar, satellite in-situ observation, rocket observation and satellite beacon tomography. However, all of those methods have some limitations, e.g., the costs. If a cheaper skill based on detecting the IAR eigenfrequency separation variations can be developed to estimate the density profile above the F2 peak, it would be helpful for not only scientific research but also space weather forecast and space exploration. Also, almost all the study on IARs to date focused the northern hemisphere. It is necessary to investigate whether the skill can be utilized at high latitudes of southern hemisphere. The study on IARs of Antarctica in the thesis is the initial work for this aim.

Chapter 2. An Overview of IAR Studies

2.1 Introduction

This thesis will concern the resonators which trap the Alfvén waves between the ionosphere and the magnetosphere. The resonance cavities between the ionosphere and the magnetosphere were studied since 1960s [Cummings et al., 1969]. Later on, in 1980s, Polyakov and Rapoport [1981] pointed out that the Alfvén waves could be trapped within the resonance cavities between the E region of the ionosphere and the magnetosphere. Also, the resonance cavities which could trap the Alfvén waves were named Ionospheric Alfvén Resonator (IAR). Gradually, it was realized that IARs played very important roles not only in the physical processes in the ionosphere but also in coupling the ionosphere and the magnetosphere. The IAR is related to not only linear but also nonlinear processes [Lysak, 1991]. Thus the IAR attracted a lot of interest.

In order to study the IAR, many theoretical models were developed including both linear and nonlinear models. There are two ways to solve those models, one is the analytical solution, and the other one is the numerical solution. Both of the two methods were used frequently. Many IAR events were observed and analysed. There are two ways to detect IAR events, one is observing IARs by pulsation magnetometers on the ground, and the other one is detecting the IARs by spacecraft. Some of the observations

were compared with the theoretical models. Additionally the observations on natural IAR events, ionospheric heating experiments to stimulate artificial IARs were utilized. This becomes a more and more important method to study the IAR and the related physical processes.

2.2 Theories and Models of Ionospheric Alfvén Resonators

Equation 2.1 is the relation of the Alfvén velocity.

$$V_A = \frac{B}{\sqrt{\mu_0 m_i n_i}} \tag{2.1}$$

where μ_0 is the vacuum permeability, B is the intensity of the geomagnetic field, m_i is the mean mass of ions and n_i is the ion number density. The Alfvén waves can be trapped between the E region of the ionosphere and the top ionosphere (see Chapter 1).

The first model of the Ionospheric Alfvén Resonator (IAR) was developed by Polyakov and Rapoport [1976], and then the model was further developed by Lysak [1988, 1991], and Belyaev et al [1990]. In order to simplify the model, the plasma density profile between the E peak and the F2 peak was supposed to be uniform. Equation 2.2 illustrates the Alfvén velocity profiles.

$$V_A^2(z) = \frac{V_{AI}^2}{\varepsilon^2 + e^{-z/h}} \tag{2.2}$$

where $V_A(z)$ is the Alfvén velocity at the altitude of z, V_{AI} is the Alfvén velocity below the F2 peak, z is the altitude, h is the effective length of the IAR and the ε is the ratio between the Alfvén velocity in the magnetosphere and the V_{AI}. Normally the typical effective length along the field line of the IAR is 1000km. The Alfvén velocity becomes a constant near the upper boundary of the resonance cavity. The Alfvén velocity profile

of equation 2.2 can be seen in Fig 2.1. Based on equation 2.2, the model equation of the IAR can be obtained, which is shown in equation 2.3 [Lysak, 1991].

$$\frac{d^2\Phi}{dz^2} + \frac{(\omega - \vec{k}_\perp \cdot \vec{v}_0)^2}{V_{AI}^2}(\varepsilon^2 + e^{-z/h})\Phi = 0 \qquad (2.3)$$

where Φ is the scalar potential, ω is the angular frequency, $\vec{k}_\perp$ is the perpendicular wave vector of Alfvén waves, and $\vec{v}_0$ is the local Alfvén velocity. This equation could be transformed into a Bessel function. Therefore, theoretically the eigenfrequencies of the IAR should be distributed as a Bessel function.

Based on this model, Belyaev et al [1990] investigated the hourly variation of the quality factors (Q factor) of IARs theoretically. It was found that the ratio between the Alfvénic wave conductivity and the height integrated Pedersen conductivity in the E region of the ionosphere varies in the range of 0.1 to 10 in a single day. The variation of the ratio leads to the change of the reflective coefficient at the bottom boundary of the IAR. Ideally the reflective coefficient of the top boundary is quite close to 1. Thus it leads to the variation of the Q factor of the IAR. However, in order to solve the model analytically, this model was idealized. In realistic cases, the Alfvén velocity between the F2 peak and the E peak is not a constant. That could lead to some errors, e.g., on the calculating the eigenfrequencies of the IAR.

There is a further simplified theoretical model of the IAR [Trakhtengerts et al, 2000a]. In this model the plasma density was supposed to be uniform within the whole resonance cavity. Based on this model the expected eigenfrequencies of the IAR are distributed uniformly in the frequency domain. This model revealed that the signals detected on the ground significantly depend on the ratio between the Alfvénic wave conductivity and the height integrated Pedersen conductivity in the E region of the ionosphere. It can be seen in Fig 2.2, which illustrates the signals in frequency domain detected by pulsation magnetometers on the ground. It can be seen that the both the phase and the signal intensities are significantly affected by the value of Σ_W / Σ_P, where

Σ_W and Σ_P are the Alfvénic wave conductivity and the Pedersen conductivity in the E region, respectively.

Both of these two models are linear and one dimensional. Additionally, the two models are solved in frequency domain. There are other IAR models, e.g., the model developed by Chmyrev et al [1988], which is a two dimensional model and can be solved in time domain. Some of the models could be utilized to investigate not only IARs but also Field Line Resonances (FLR) [Streltsov and Lotko, 2004]. Also, there is a model named full wave model, which could simulate the eigenfrequencies of the IAR quite well [Prikner et al, 2004]. Based on these models, the characteristic of IARs could be investigated theoretically.

According to the electron density and the ion mass density profiles detected by EISCAT (European Incoherent SCATter) Tromsø radar, Prikner et al investigated the effective altitudes of the IAR using the full wave model [Prikner et al, 2007]. The profiles were detected on 7 March 2001 when the EISCAT Tromsø radar was working on CP1 and CP7 (Common Programme 1 & 7) mode. The altitude range of the detection extended up to 2300km. Also, there were Pc1 pearl structures detected by the pulsation magnetometer on the ground, which was considered to be the resonance on the fundamental eigenfrequency of the IAR. Using the full wave model, it was found that the maximum effective altitudes for the IAR on that day were about 1200km to 1500km. The altitude could be greater than 1500km for other IAR events. In other words, in order to numerically investigate the eigenfrequencies of the IAR, the effective altitude that needs to be considered should be greater than 1500km to reduce the numerical errors.

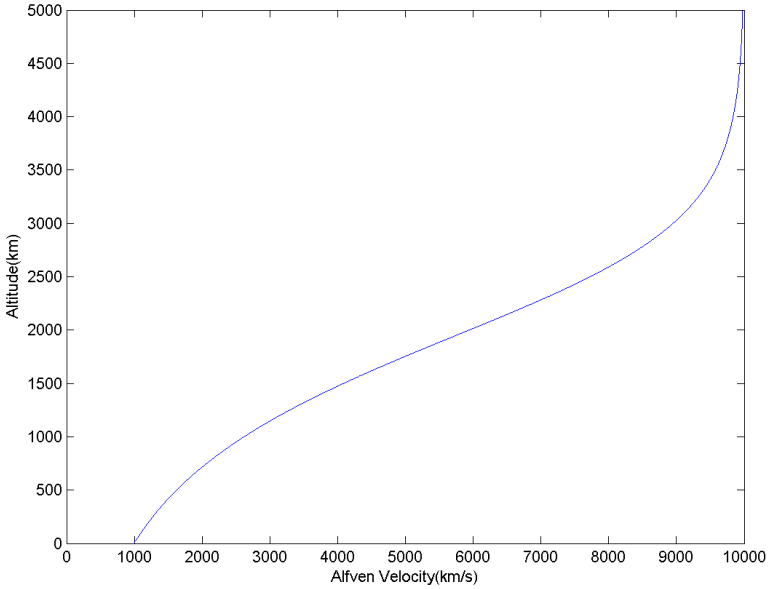

Fig 2.1 The idealized Alfvén velocity profile in the model developed by Lysak [1988, 1991], Belyaev et al [1990].

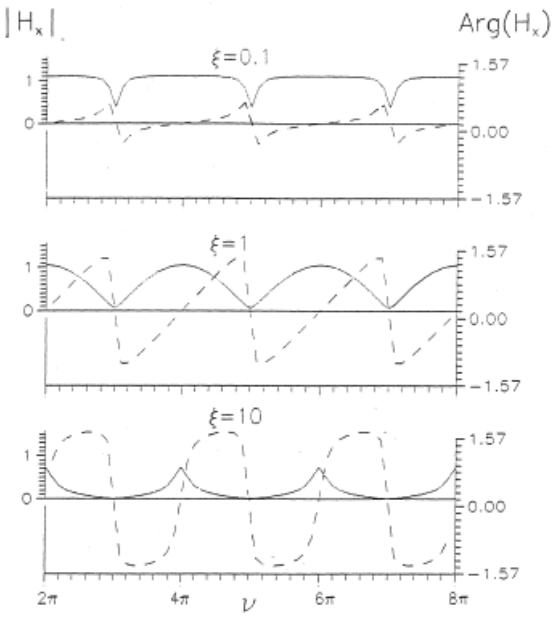

Fig 2.2 The signals that can be detected on the ground according to Trakhtengerts' model [Trakhtengerts et al, 2000a]. ξ is the ratio between the wave conductivity and the height integrated Pedersen conductivity.

2.3 Observations and Data Interpretations of IARs

Normally there are two ways to observe IARs, which are remote detection by pulsation magnetometers on the ground and the in-situ observation by space crafts. Both of the two ways were utilized to observe the IARs frequently. The concerned resonance frequencies of IARs are normally Spectrum Resonance Structures (SRS) in the band of 0.1Hz-5Hz in dynamic spectra observed by pulsation magnetometers are normally considered to be the signs of IAR events [Hebden et al., 2005]. Most of observations of IAR events were based on the SRS signals. Fig 2.3 shows an example of SRS signal in the dynamic spectrum obtained on the ground by a pulsation magnetometer [Hebden et al, 2005]. The data was obtained by the pulsation magnetometer at Sodankyl ä on 4 October 1998. The SRS signal is the periodic structures in the period of 16 UT to 21 UT.

For in-situ observations, due to the high speed of satellites, it is difficult to see SRS signals on the dynamic spectrum. Thus the periodic oscillation of the field is an important criterion to find IARs [Chaston et al, 2002; Robinson et al, 2000]. There is also other criterion for finding IARs from satellite data, e.g., electron acceleration. Fig 2.4 illustrates an example [Robinson et al, 2000]. Clear oscillation on the perpendicular electric field can be seen in the top panel. The oscillating period is about 0.34s, which means the oscillating frequency is about 3Hz. The oscillation lasted for just about 4s. Electron acceleration related to the field oscillation can be seen in the middle panel. Additionally, there were joint observations on IARs by satellites and ground-based pulsation magnetometers simultaneously [Yeoman et al, 2008]. The joint observation also illustrated the electron acceleration related to the IAR.

There were also joint IAR observations by multiple pulsation magnetometers in a same period [Ermanova and Kotik, 2008]. Ermanova and Kotik [2008] have investigated the global and local IAR properties based on the spectrum data collected at two stations, which are the New Life Station and the Lovozero Station. The distance between the two stations is more than 1000km. According to the study it was found that the SRS

characteristic observed at the two stations are different. The eigenfrequencies of the IARs observed at the two stations are different. Additionally, the IAR occurrence at New Life station was 80% to 90%, which is quite high and typical for mid- latitudes. However, the IAR occurrence at the Lovozero station, which is at high latitudes, was just 20% to 30%. The different characteristics were caused by the differences of the latitudes of the two stations. The study revealed that the characteristic of the IAR strongly depend on the latitude.

Additionally, there are a lot of studies on the IAR occurrence of the northern hemisphere. The diurnal, daily, monthly, seasonal and annual variations of the IAR occurrences were statistically investigated based on ground observations at different latitudes. During 2002 to 2006, the diurnal occurrence of the IAR at Barentsburg (L=15) was found to higher than 15% during the period of 18 UT to 3 UT, which reached the maximum. The lowest occurrence was during the period of 9 UT to 12 UT, which was zero [Semenova and Yahnin, 2008]. In this paper it was mentioned that the IAR occurrence at Barentsburg was much lower than at mid- and low- altitudes. Belyaev et al [2000] statistically investigated the IAR occurrence against the solar activity based on the data obtained in 1985 to 1995 at mid-latitudes. An anti-correlation between the IAR occurrence at mid-latitudes and the solar activity was found. The IAR occurrence was practically absent during the solar maximum, and reach the maximum during the solar minimum. For the seasonal IAR occurrence at mid-latitudes, the occurrence reached the maximum in the period of September to January and the minimum in the period in March to June during 2000 to 2002 at Karimshino, Russia (L=2.1) [Molchanov et al, 2004]. Also, the maximum daily occurrence was found at 21 LT to 23 LT, and almost all the IARs were observed at local night time. According to Bosinger et al [2002], there was not any IAR observed at local day time at Crete station (L=1.3), which is at low-latitudes. Both data interpretations and theoretical studies revealed that the IAR occurrence strongly depends on the solar activities. Solar activities could change the ionospheric conditions, which lead to the variation of the reflective coefficients. The source of oscillations depends on the reflective coefficients. Also, the variation of the ionospheric conditions could change the Q factor of the Alfvénic resonance cavities, which is a very important factor for the IAR occurrence [Trakhtengerts et al, 2000b].

All of those studies focused on the IAR occurrence in northern hemisphere. In this thesis, the IAR occurrence at high latitudes of southern hemisphere will be statistically studied in Chapter 4.

As a resonance phenomenon, the eigenfrequencies are a very important characteristic of an IAR. The eigenfrequencies of an IAR can be used to diagnose the ionospheric conditions, e.g., calculate the effective size or plasma density [Hebden, 2005]. In some studies, the ionospheric plasma density profile was simplified to be a uniform profile. The distance between the upper and lower boundaries of the uniform profile was defined as the effective size of the IAR, and the plasma density of the uniform profile was defined as the effective plasma density of the IAR. Thus there were lots of studies on the eigenfrequencies of IARs, particularly the statistical studies at different altitudes. Also, there are many methods developed to find the eigenfrequencies of the IAR. At low altitudes, it was found that the IAR eigenfrequency separations Δf is quite small, typically around 0.2Hz. Additionally, it does not change too much with time [Bosinger et al, 2002]. However, on the high latitudes, the IAR eigenfrequency separations could change from about 0.24Hz to more than 0.6Hz in a single day in autumn [Hebden et al, 2005]. The IAR eigenfrequency separation at mid-latitudes varies with season. In autumn the averaged Δf is about 0.2Hz to 0.5Hz; in winters the averaged Δf increased to 0.5Hz to 0.7Hz [Molchanov et al, 2004]. Those indicate that the IAR eigenfrequency separations and the variations of the separations strongly depend on time at high and mid- latitudes. However, they do not change too much at low latitudes. Additionally, those studies revealed the latitude dependence of Δf. Based on those results, the effective size of the Alfvénic resonance cavities could be found. For example, the average effective size of the IAR at Sodankylä in October 1998 was about 530km [Hebden et al, 2005].

Also, it should be noticed that there are several methods to calculate the Δf based on the dynamic spectrum data. An automatic method to find the separations of IAR eigenfrequencies involves comparing the amplitude of each component of frequency with the two adjacent frequencies. If the amplitude is higher than the two adjacent frequencies, then it could be identified as a "peak" [Odzimek et al, 2006]. Additionally, there are some other methods introduced by Hebden et al [2005]. The first method

introduced in this paper is based on the slices of dynamic spectrum. This method is quite similar to the method introduced in Odzimek's paper [2006]. The difference is that, in Odzimek's paper the peaks on a dynamic spectrum slice are found automatically by a computer programme; in Hebden's paper the peaks and troughs on a dynamic spectrum slice are defined manually. The second method is named 'pseudo frequency'. A Fast Fourier Transform (FFT) is utilized in a single dynamic spectrum slice. According to Trakhtengerts's model [Trakhtengerts et al, 2000a], the eigenfrequencies of the IAR are distributed uniformly in frequency domain. Thus the peaks and troughs appear to be a periodic structure in a single spectrum slice. By doing FFT on the data of a single spectrum slice, if a clear peak is founded in the FFT result, it indicates that there is a periodic structure in the spectrum slice. The periodic structure indicates the existence of the IAR. This peak in the FFT result corresponds to the IAR eigenfrequency separations in that dynamic spectrum slice. The third method is manually clicking the periodic structures on the dynamic spectrum by cursor. Then each click highlights a point on a resonance frequency. By linking those points, the trend of the IAR eigenfrequency variation could be seen on the dynamic spectrum directly. In Chapter 3 of this thesis, a new method which is similar to the first method in Hebden's paper will be introduced.

2.4 Numerical Studies

For a specified theoretical model of space plasma physics, there are two methods to solve the model. One method is solving the model analytically. The one dimensional models introduced in section 2.3 are solved in this way. The other method is solving the model numerically. Numerical computation becomes more and more important in scientific research, particularly with the development of parallel computations. For example, three dimensional global M-I Coupling models can be solved numerically to study the dynamics of global space plasma dynamics [Pang et al, 2010].

For the studies of IARs, numerical computations are also frequently utilized. The effective altitude of the IAR calculated based on the data obtained by EISCAT Tromsø

radar and the pulsation magnetometer was worked out numerically based on the full wave model [Prikner et al, 2007]. Additionally, some nonlinear models are difficult to solve analytically, however, approximate solutions can be obtained by utilizing numerical computations [Streltsov and Lotko, 2004].

In the one dimensional models introduced in section 2.3, the Alfvén velocity profiles were idealized in order to solve the models analytically. The models are very difficult to solve with realistic Alfvén velocity profiles. In order to compare the theoretical model and the observed data, it is necessary to utilize the realistic profiles. Thus in this thesis, a numerical model will be introduced.

2.5 Artificial Heating Experiments

Almost all the IAR observations introduced in section 2.5 are natural IARs. However, IARs could be stimulated or strengthened by artificial ionospheric heating experiments [Robinson et al, 2000; Yeoman et al, 2008; Scoffield et al, 2006]. Artificial heating experiments became a very important way to investigate the coupling processes between the ionosphere and the magnetosphere.

There are two frequently used artificial heating facilities at high latitudes of Europe. In late 1960s EISCAT established a heating facility at Tromsø, Norway. Later on, a heating facility was constructed in Longyearbyen, Svalbard, Norway. The later heating facility was named SPEAR (Space Plasma Exploration by Active Radar). Both of the two heating facilities did a lot of heating experiments to stimulate artificial IARs.

On 2 December 2005 an artificial heating experiments was carried out using the SPEAR heating facility [Scoffield et al, 2005] on the frequency of 3Hz. The enhancement of the signal intensities at 3Hz was detected on the ground by pulsation magnetometers. Based

on this experiment the artificially enhanced IAR and natural IARs were compared [Yeoman et al, 2008]. Additionally, on 8 October 1998 an artificial heating experiment was carried out by EISCAT Tromsø heating facility [Robinson et al, 2000]. The response signals were detected by FAST satellite. Also, the related electron accelerations were observed. That implied feedback instability might be stimulated by the artificial heating experiment. Feedback instability is a nonlinear process related to IARs. The particle precipitation related to the IAR change the plasma density in the Pedersen conductive layer. As the results the Pedersen conductivity enhances. The enhanced Pedersen conductivity could accelerate the particle precipitation and further change the Pedersen conductivity. That is defined as the feedback instability.

Those successful artificial heating experiments have shown that the artificial heating techniques are quite useful and helpful in exploring the physics of the M-I coupling and the ionosphere at high latitudes.

2.6 Summary

Ionospheric Alfvén Resonators are important physical processes at high latitudes. They play a very important role, not only in the ionosphere but also in coupling the ionosphere and the magnetosphere. For example, IARs relate to the particle precipitations from the magnetosphere into the ionosphere, which could significantly change the plasma density profile in the ionosphere and the low altitude magnetosphere. It is necessary to investigate IARs in order to understand the physics of space plasma dynamics. There were several theoretical models of IARs developed in past decades. Some of the models could be solved analytically, but some of them have to be solved by numerical computations. Also, there are many works on IAR observations and data interpretations. The IAR could be detected by satellites or pulsation magnetometers on the ground or both. According to previous works the characteristic of the IAR were found to differ at different latitudes. Additionally, there are also seasonal and annual variations of the characteristic of the IAR. However, all of those works were on the

IARs observe at northern hemisphere. Additionally, artificial heating experiments are quite useful in understanding the physics of IARs. In this thesis, all the studies of the IAR will be based on the previous works introduced in this chapter.

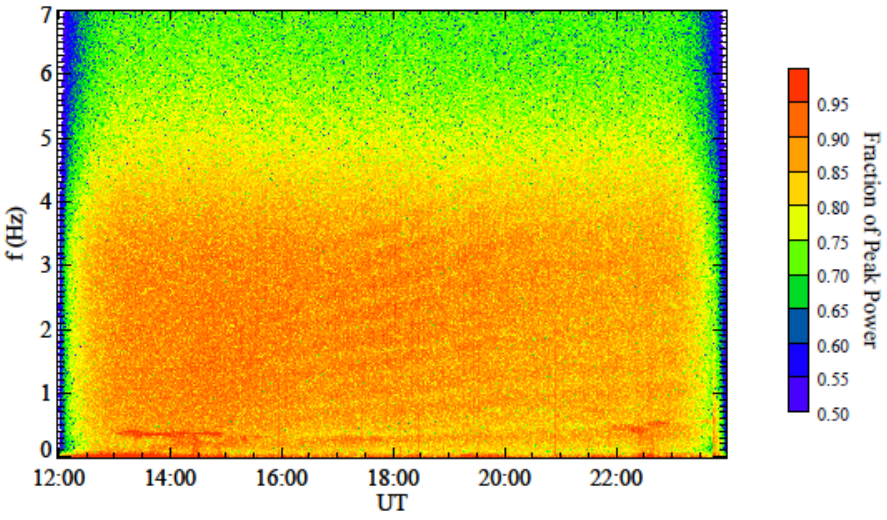

Fig 2.3 The dynamic spectrum of 04/10/98 at Sodankyl ä is shown in the figure [Hebden et al, 2005].

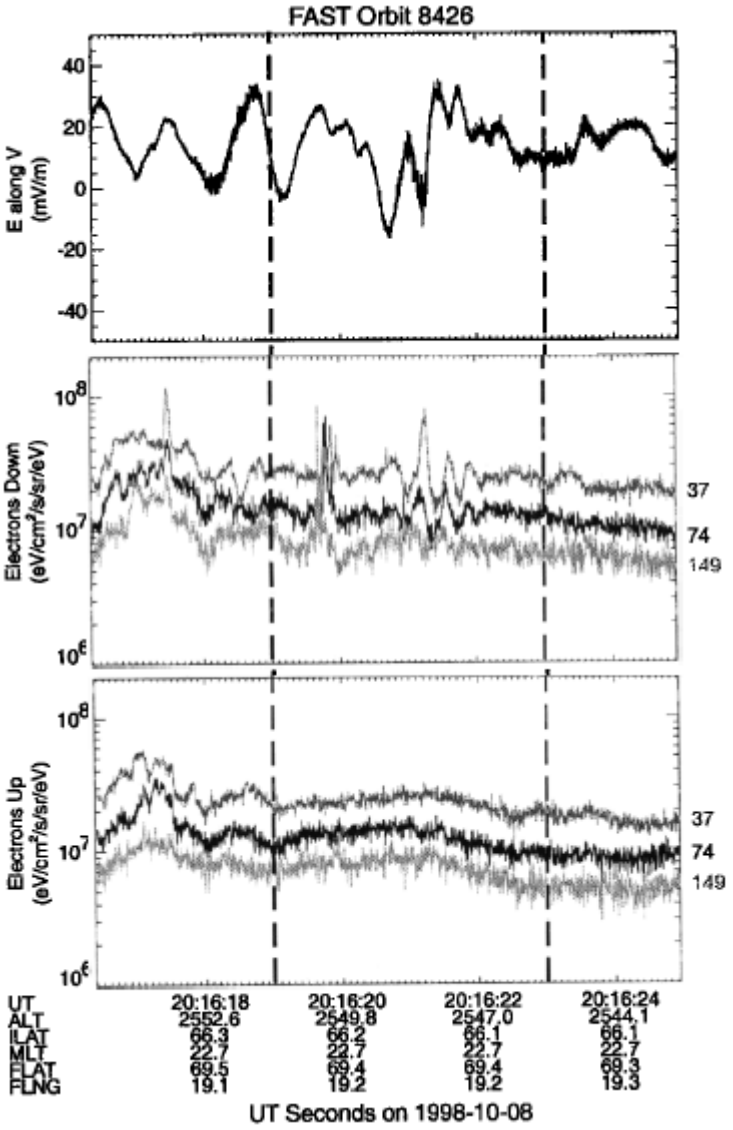

Fig 2.4 The data collected for the artificial heating experiment carried out on 08/10/98 at Tromsø [Robinson et al, 2000]. The top panel illustrates the electric field strength perpendicular to the magnetic field; the middle and the bottom panel illustrate the electrons go downwards and upwards, respectively.

Chapter 3. Observations of IARs at High Latitude Regions of Northern Hemisphere

3.1. Introduction

The effective size of the Ionospheric Alfvén Resonator (IAR) is less than 2000km [Prikner, et al., 2007], and the maximum of the Alfvén wave velocity within the IAR is no more than ten thousand km/s. Thus the detectable eigenfrequencies of the IAR is less than 10Hz. Due to the limited sensitive frequency band of pulsation magnetometers, the Spectrum Resonance Structures (SRS) in the band of 0.1Hz-5Hz in dynamic spectra observed by pulsation magnetometers are normally considered to be the signs of IAR events. Most observations of IAR events are based on the SRS signals.

In order to analyse IAR events quantitatively, it is necessary to analyse the spectral data observed by pulsation magnetometers. However, there is a lot of noise in the obtained magnetometer data. It is difficult to remove the noise from the total signal. Thus it is not easy to analyse an IAR event data quantitatively.

However, there are several methods to identify the eigenfrequencies or eigenfrequency separations of IARs (see Chapter 2). In this chapter, the quantitative analysis of IAR events was carried out based on the eigenfrequencies and the variations of eigenfrequencies of the IARs. There have been previous studies of the IAR eigenfrequency properties at low latitudes [Bosinger et al, 2002]. All the IAR events investigated in this chapter were detected at high latitudes in the northern hemisphere. The study was aimed at characterizing the IAR eigenfrequency variations at high

latitudes, particularly the time and spatial scale of the variations. In addition, the factors that give rise to the variations were investigated.

In order to investigate the time scale of IAR eigenfrequency variations, the data collected at Sodankylä in October 1998 was utilized. There were 13 IAR events identified at Sodankylä in October 1998 [Hebden et al., 2005]. In this chapter, four events which occurred on 04/10, 05/10, 14/10 and 30/10 in 1998 were selected to be analysed. The SRS of the four events were clearer than others. Also, the dates of the events covered the beginning, the middle and the end of the month. That means those events could illustrate the features of the IARs occurred during the whole October in 1998.

In order to investigate the spatial structure of IARs, a single IAR events observed by 5 magnetometers at different locations was analysed. More details will be discussed in section 3.2 and 3.4.

For the study presented in this chapter, the eigenfrequencies were defined by the periodic structures on dynamic spectrum slices. Basically the eigenfrequencies of an IAR were considered to be distributed uniformly in the frequency domain [Hebden et al., 2005; Trakhtengerts, 2000a; Belyaev et al., 1990]. That means for an individual IAR dynamic spectrum slice, the eigenfrequency separation is a constant. Thus the eigenfrequencies correspond to the peaks on dynamic spectrum slices. On the other hand, the noise is not periodic on dynamic spectrum. Thus the noise does not have significant impact on the results of the analysis of eigenfrequencies. In such a case it is not necessary to remove the noise signals from the total signal.

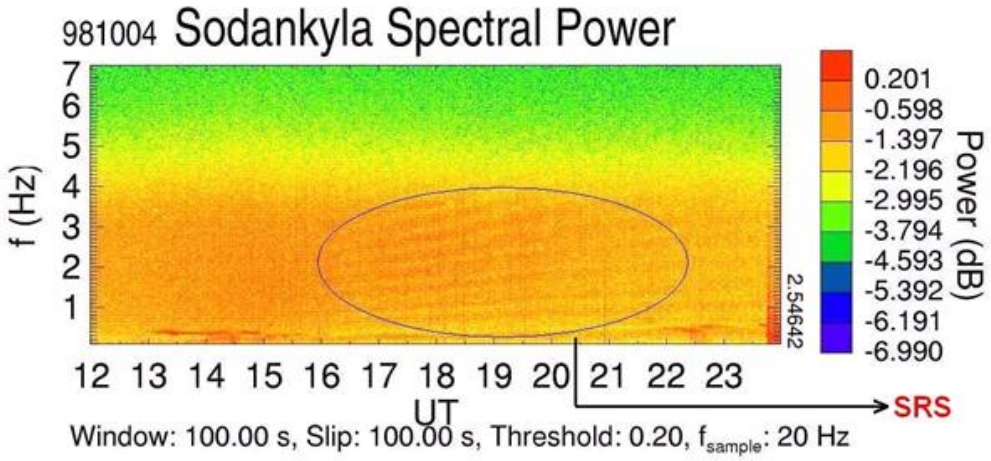

Fig 3.1 The figure shows the dynamic spectrum of the H components, which was observed at Sodankyl ä on 4 Oct 1998. The SRS was highlighted with the oval.

3.2. Brief Introduction to the Events

In October 1998 there were 13 IAR events observed by the pulsation magnetometer in Sodankylä Geophysical Observatory (SGO). The dynamic spectrum of the H component of the event observed on 04/10 is showed as an example in Fig 3.1.

Fig 3.1 illustrates the dynamic spectrum of the time interval from 12 UT to 24 UT. A clear SRS signal can be seen. The SRS was highlighted by the oval. The sampling rate of the pulsation magnetometer was 20Hz. That means the time resolution of measurements was 0.05s. The dynamic spectrum showed in Fig 3.1 was obtained from the time series of the pulsation data by using a running Fast Fourier Transform (FFT). The width of the sliding window was 100.00 seconds. That means there were 2000 measurements in each sliding window. Basically the 2^n (n is an integer) data points are used most frequently in FFT. Otherwise, there would be errors generated by the FFT process. However, according to Hebden [2005], for those events, the quality of the results of 2000 data points' window is good enough. The SRS signals are clearly visible in Hebden's results. The same IAR events will be analysed in this chapter. Thus the same window will be utilized for those events in this chapter. The sliding distance was also 100.00s. That means there was no overlap between every two neighbouring sliding windows. A threshold that can be seen at the bottom of the figure was set to plot the dynamic spectrum. The value of the threshold to plot the spectrum was 0.2, which means that the components were not plotted on the spectrum plot if their power was lower than 20% of the peak power. The peak power frequency was artificially selected to be 3Hz [Hebden et al., 2005]. The mean power of 3Hz components was showed vertically as digits on the right hand side of the dynamic spectrum. Levels of fractional powers were illustrated in the colour bar on the right. The response curve of the magnetometer was not known due to the limited data support, thus the impact caused by the response curve was not taken into account in this study.

There were 13 IAR events observed during the whole October in 1998 at Sodankylä. Four events were selected for the study in this chapter. The dynamic spectra of those 4

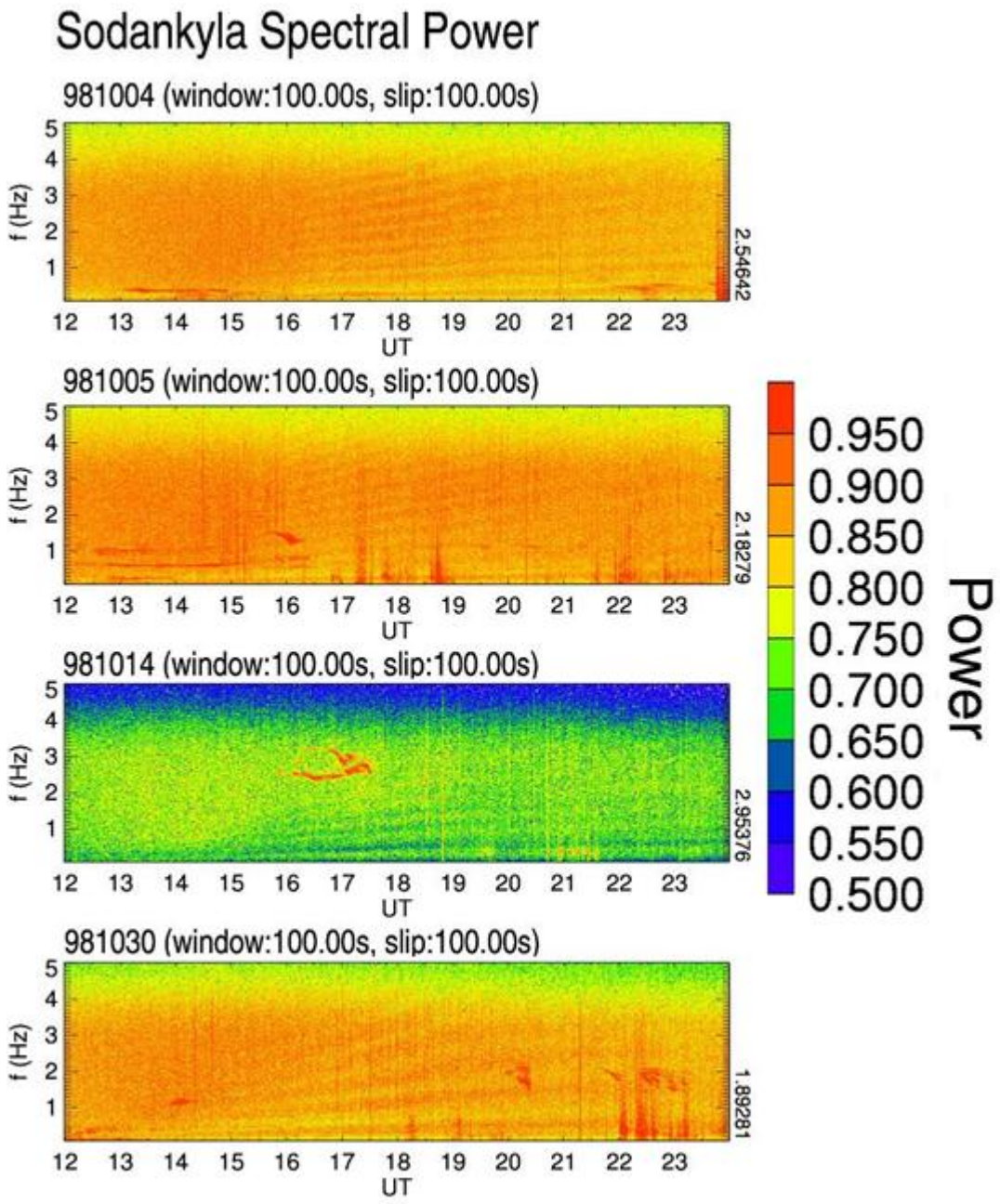

Fig 3.2 The dynamic spectra of 04/10/98, 05/10/98, 14/10/98 and 30/10/98. Fractional powers which referred to the component of 3Hz were showed in the colour bar. The power of 3Hz was showed vertically at the right of each panel. The time for the plot is the universal time.

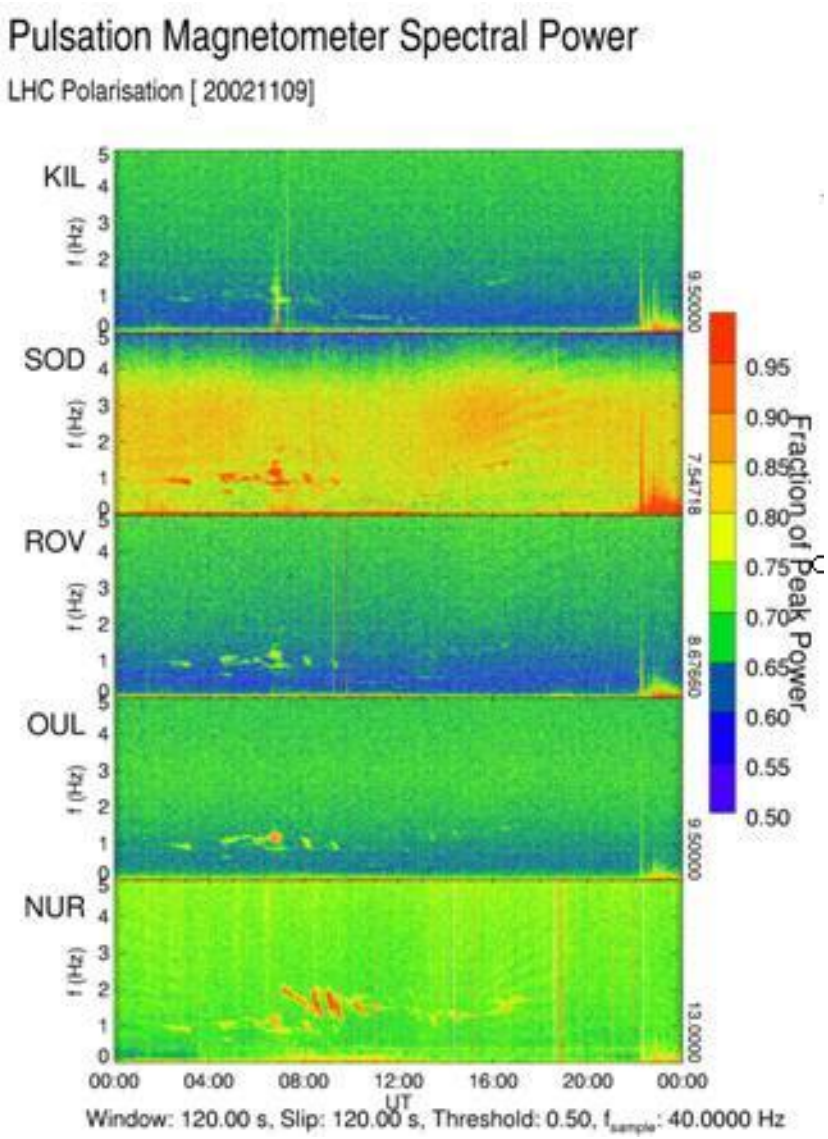

Fig 3.3 The dynamic spectra observed at the five stations. The five stations are Kilpisjärvi, Sodankylä, Rovaniemi, Oulu and Nurmijärvi, respectively.

Fig 3.4 The map of the five stations. Ivalo station was not working on 9 Nov 2002. Kilpisjärvi station is in arctic region. (http://www.sgo.fi/Data/Pulsation/pulDescr.php)

Station	***Mag. Lat.***	***Mag. Long.***	***L Shell***
Kilpisjärvi	65.9N	103.8E	6.0
Sodankylä	64.0N	107.1E	5.2
Rovaniemi	63.4N	106.3E	4.9
Oulu	61.6N	104.9E	4.4
Nurmijärvi	56.9N	102.1E	3.3

Table 3.1 The details of the locations of the five Finnish stations.

events can be seen in Fig 3.2. SRS signals are quite clear in all of the four panels. The dates of the events are 04/10/98, 05/10/98, 14/10/98 and 30/10/98, respectively. The fractional powers, which referred to the component of 3Hz, are showed in the colour bar. The powers of 3Hz component are showed vertically at the right of each panel.

In addition, on 9 November 2002 an IAR event was observed by five Finnish pulsation magnetometers simultaneously. Fig 3.3 illustrates the Left Hand Circular (LHC) polarized spectra of the IAR event observed at the five stations. The frequency of the peak power was also selected to be 3Hz. Also, the intensity of the components at 3Hz was listed vertically at the right hand side of each panel.

The five stations are located in Finland, which are Kilpisjärvi (KIL), Sodankylä (SOD), Rovaniemi (ROV), Oulu (OUL) and Nurmijärvi (NUR), respectively. In addition, there is a pulsation magnetometer in Ivalo, which is between KIL and OUL. However, the magnetometer in Ivalo was not working on 9 November 2002, thus the data of the magnetometer in Ivalo was not utilized in this study.

Due to the limited data support this is the only recorded event observed by multiple stations. The five magnetometers are part of Finnish magnetometer chain. The sampling frequency of those magnetometers was 40Hz in 2002. The five stations form a chain from north to south in Finland. The locations of the five stations are showed in Fig 3.4, and more details are listed in Table 3.1. The Sodankylä station was included. The local time of the five stations was 2 hours prior the universal time in November.

There have been previous studies on multiple station observation and data interpretation on IAR events [Ermakova and Kotik, 2008]. However, there were only two stations used in the previous study, and the two stations were widely separated (over 1000km). In this chapter, the stations are much closer. Also, there were five stations utilized for the study.

The SRS signals are clearly visible in SOD and NUR, but less clear in ROV, although it is still visible. It is difficult to see SRS features in KIL or OUL. In order to make sure the IAR event was detected at KIL and OUL on 9 Nov 2002, a spectrum slice of 18UT was selected from the whole dynamic spectrum. The five panels in Fig.3.5 show spectrum slices at 18UT of the five stations respectively. Data displayed in those panels has been smoothed by running average over the data of the single spectrum slice. Similar harmonic structures (troughs and peaks) can be seen in all of the five panels. The plot shows the five stations detected the quite similar IAR event simultaneously though SRS signals on the dynamic spectra of KIL and OUL are not visible. The peaks and troughs observed at the five stations are quite similar.

The width of the FFT sliding window for the event was 120 seconds; the sliding distance was 120 seconds. That means there was no overlap between any two neighbouring sliding windows. It should be noticed that the sampling frequency of SOD station in 2002 was higher than in 1998.

It can be seen that the SRS signals started at about 15:30UT, and ended at about 20:00UT. Generally the eigenfrequencies of the IAR kept increasing during this period. Pearl structures can be seen earlier than the IAR events. For example, in NUR station the pearl structure started at the morning and ended before the start of the SRS. The pearl structures could represent the oscillation in the magnetosphere and strengthened by the resonator [Prikner et al., 2004].

3.3. Methodology

The noise is partly removed by the method introduced in more details next. The numerical errors caused by FFT processes just occurred at low frequency bands. Generally the errors just occurred below 0.1Hz, which is beyond the band that should be concerned in this study.

A double running average method and a sinusoidal curve fitting method were used to find the eigenfrequencies of the IAR events at certain periods precisely. The double running average method removed the pulsation noise from the total pulsation signals. It made the sinusoidal curve fitting method work better. Double running average method means using the standard moving average process twice on a single spectrum slice. Fig 3.6 illustrates the process of the double running average. The spectrum slice showed in panel a is the raw dynamic spectrum slice of the period of 17:50:00UT to 17:51:40UT on 4 Oct 1998. It can be seen that the harmonic structures are almost invisible. Panel b illustrates the data that has been smoothed once with moving average method on every 20 data points. The harmonic structures are visible and quite clear in the panel. However, there are still a lot of small fluctuations on the curve showed in panel b. Normally the running average method just utilized once over the data in a single spectrum slice, which is a single FFT window. However, those fluctuations can significantly influence the results of the sinusoidal curve fitting process in this study. The fluctuations could lead to incorrect results of the curve fitting. By comparing with the results of Hebden et al [2005], the double running average method is good enough for finding the eigenfrequencies of the IAR. Additional test details can be seen in A4 of APPENDIX. In such a case, the data showed in panel b was smoothed once again using the same method on every 10 data points. The final result was showed in panel c. It can be seen that almost all the small fluctuations on the curve showed in panel b had been removed. Thus the curve showed in panel c will be used to do the curve fitting.

In practice, the eigenfrequencies separations were normally treated to be equivalent, which means $\Delta f \approx f$, where Δf is the separation between every two neighbouring eigenfrequencies, and f is the fundamental eigenfrequency [Belyaev et al., 1990]. That means the curve of a spectrum slice can be treated as a quasi-periodic function. That is based on the assumption that the Alfvén velocity within the cavity could be treated as a constant. This assumption is not always true. An example is showed in Fig 3.16, and the relevant factors will be investigated in Chapter 7. However, in most of the studies of the IAR eigenfrequencies, the eigenfrequency separations were considered to be constant [e.g. Odzimek, 2006; Hebden, 2005], thus the assumption of the constant

eigenfrequency separation will be utilized in the study in this chapter. The sinusoidal function is a typical periodic function. Also, cosine function is also periodic and it is almost same as the sinusoidal function. Thus both of the functions can be utilized to do the curve fitting. In this chapter, the sinusoidal function is utilized. There were many methods to determine the eigenfrequencies of IARs [Odzimek, 2006; Hebden, 2005]. Comparing with those methods, the frequency resolution of the method utilized in this chapter is higher.

The sinusoidal curve fitting method is a least square curve fitting process. Considering there are 700 data points, which are $D_1, D_2, D_3, ..., D_{700}$ in the frequency range of 0.01-7Hz, the resolution of the frequency is 0.01Hz. Because the magnitudes of components are different, an interval would be picked out for curve fitting. Assuming that the interval represented by subscripts range from M to N was selected, the frequency range for curve fitting would be m/100 to n/100. The sinusoidal function is:

$$D = a * \sin(b * f + c) + (\sum_{i=M}^{N} H_n) / (m - n + 1) \tag{3.1}$$

where a, b, c are coefficients. According to the expression, the period of the function depends on b, and a denotes the average magnitude of components in the selected interval. These two coefficients are worth being investigated. Using that method on the interval of 17:50:00UT to 17:51:40UT, the result is showed in Fig 3.7. In this figure the blue lines are spectrum slices and the red lines are fitted curves. The left panel shows the curve fitting on the frequency band of 1.00Hz to 3.20Hz comparing with the double-smoothed data. And the curve was moved towards the x-axis to make it centred at the x-axis approximately. The distance of the movement is the last term in equation 3.1. The right panel shows the comparison between the extension of the fitted curve from 0.01-4.00Hz and the single-smoothed data. In this panel the troughs and the peaks of the fitted curve and the observed curve correspond to each other quite well. Thus the sinusoidal curve fitting is proper to study the separation and the eigenfrequency variations of IAR harmonic structures. The goodness of the curve fittings is represented by the value of R^2, which shows that in what extent the fitted curve matches the data [Steel and Torrie, 1960]. This method is quite sensitive to small variations of IAR eigenfrequency shifts because any small change of the eigenfrequency separation would

lead to the change of the value of coefficient b of equation 3.1. Thus all the measurements of the methods are based on the coefficient b in equation 3.1.

3.4. The IAR observed by single station

The four IAR events that occurred in October 1998 at SOD were studied in order to investigate the time scale of IAR eigenfrequency shifts at high latitudes. The dates of the 4 events are 04/10/98, 05/10/98, 14/10/98 and 30/10/98, respectively. The dynamic spectra of the 4 events were showed in Fig 3.2.

In order to calculate the eigenfrequency separations of those events, some intervals were selected from the dynamic spectrum of each event. Basically there are four criteria to select the intervals based on the curve of the spectrum slices. First, the peaks and troughs of the selected spectrum slice should be quite clear and easy to be identified. Second, the separation between the peaks should be almost equivalent. Otherwise the assumption of the uniformly distributed eigenfrequencies (see Section 3.3) would not be satisfied, and the sinusoidal curve fitting would not work approximately. Actually most of the peak separations are not equivalent. An example can be seen at the end of section 3.6. Further details of the non-uniformity of eigenfrequencies will be discussed in Chapter 7. Third, the most concerned frequency band is 0 to 4Hz. A certain band would be selected from 0 to 4Hz. The mean signal strength on the certain band should be almost same. For example, in Fig 3.7, the selected band is 1Hz to 3.2Hz, in which the signal strengths of the harmonic structures are almost same. The fourth is that the value of the R-square of the curve fitting should be between 0.5 and 1, which represents a relatively high quality of the curve fitting.

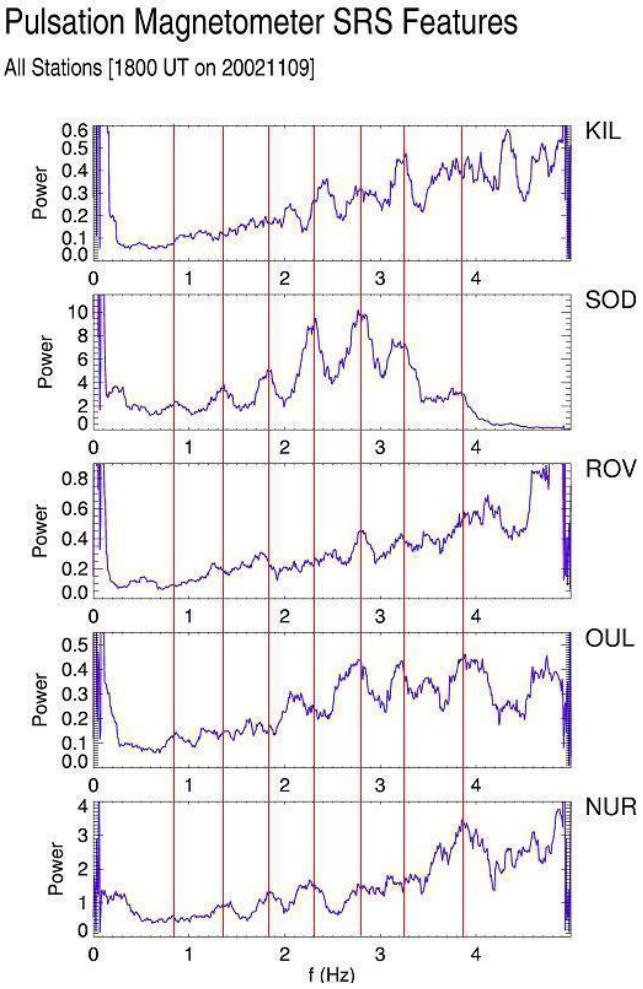

Fig 3.5 The dynamic spectrum slices of the five stations of the period around 18UT. The red lines highlighted harmonic structures.

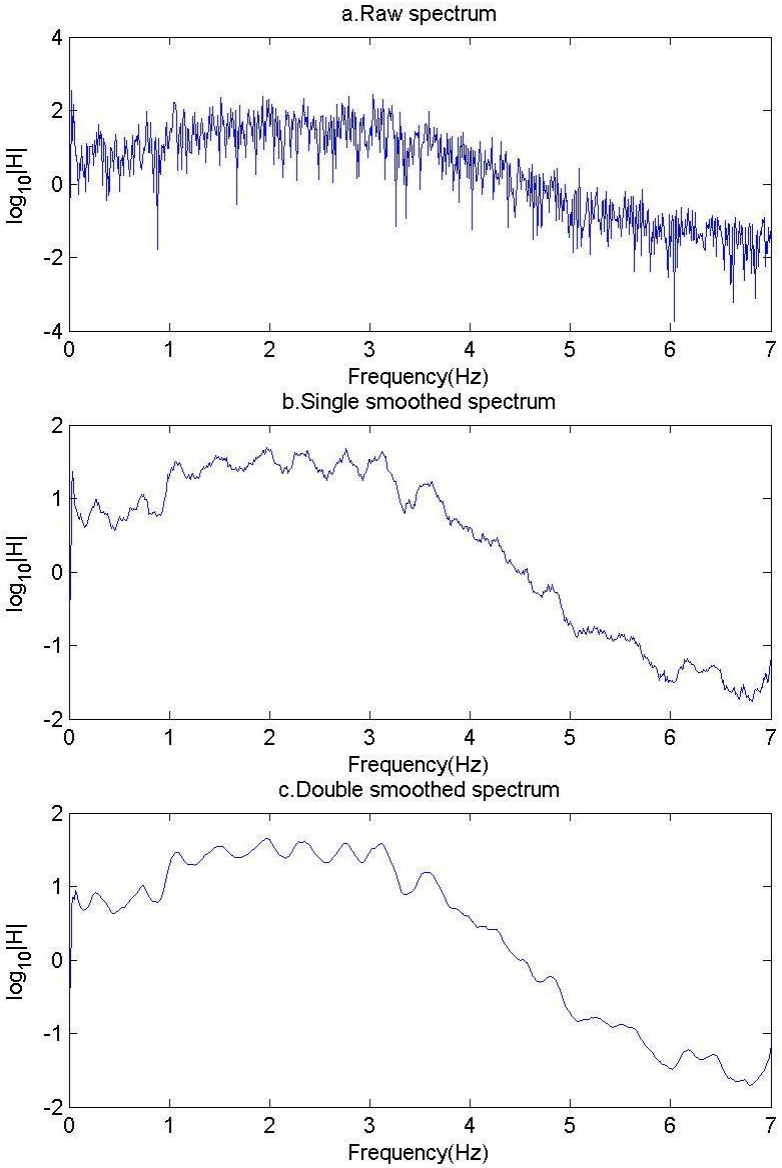

Fig 3.6 The schematic illustrates the double running average method. Panel a. shows the raw spectrum data. Panel b. shows the data has been smoothed once. Panel c. shows the data smoothed twice.

Fig 3.8 illustrates the eigenfrequency variations of the four events based on the sinusoidal curve fitting method. The error bars denote the confidence boundaries of 95% of the curve fittings. It can be seen that the general trend of the eigenfrequency separation variations is increasing. That is caused by the variations of ionospheric conditions which were led by daily solar radiation variations, which is caused by the variation of the zenith angle. The zenith angle strongly affects the ionospheric plasma density profile as well as the Alfvén velocity profile [Kelley and Heelis, 1989]. Also, it can be seen that there are fluctuations of the eigenfrequency separations of all the events. The eigenfrequency variations were not increasing monotonically. Furthermore, the fluctuations could occur in less than 10 minutes. In addition, the eigenfrequency separations could change significantly in a short period. For example, in the second panel, the eigenfrequency separations almost decreased then increased for 50% in 18:30 to 18:40 and 18:40 to 18:50, respectively. In the third panel, the eigenfrequency separations increased for more than 60% in 17:50 to 18:00. The factors that lead the fluctuations and the quick change of the eigenfrequency separations will be discussed in more details in Chapter 7.

In addition, the single moving average method carried out on the five selected time intervals across the whole lifetime of the IAR event observed on 04/10/98. The result is showed in Fig 3.9, where the blue line, the green line, the red line, the yellow line and the black line represent time intervals of 17:50:00UT - 17:51:40UT, 19:13:20UT - 19:15:00UT, 20:36:40UT - 20:38:20UT, 22:00:00UT - 22:01:40UT and 23:23:20UT - 23:25:00UT, respectively. Obviously, the wave-like structures appear on the logarithm dynamic spectrum slices correspond to oscillations of resonance. The power under the wave-like structures corresponds to the noise of the ionosphere detected by the magnetometer. The ‘noise’ means the non-harmonic signals detected by the pulsation magnetometer. The intensity variations with frequency were partly caused by the response curve of the magnetometer. According to the figure, magnetic components from 1.00-3.30Hz are getting weaker with time. Particularly the noise was getting weaker. It might be caused by the variation of the ionospheric condition, which might contain the signal of source current of the IAR. In Chapter 4 and Chapter 7 more details will be discussed, and further study will carry on.

3.5. The IAR observed by multiple stations

Again the double running average method and the sinusoidal curve fitting method were used to find the eigenfrequencies of the IAR event observed by multiple stations. Fig 3.10 illustrates the curve fitting results at the interval of 16:47:00UT – 16:49:00UT. It can be seen that the eigenfrequencies are different at different stations in the interval. From high latitude to low latitude, the eigenfrequencies were 0.3845Hz, 0.4192Hz, 0.4640Hz, 0.3143Hz and 0.4007Hz, respectively. The confidence boundaries for the curve fitting processes of the five stations were fixed to be 95%. The confidence boundaries of each station are showed in the brackets below the corresponding panel. The selected bands on spectrum slices of different stations were also different. It can be seen on the horizontal axis of each panel. Also, in some of the stations the eigenfrequencies show some non-uniformity, e.g., on the band of 1.5Hz to 2.3Hz in ROV. The criteria to select the interval are same with those mentioned in the last section. The quality of the curve fitting is not quite good for ROV. Unfortunately this is the only interval that is good enough to do the curve fitting for all of the five stations. The eigenfrequency separation variations of IARs are mainly dominated by ionospheric plasma density variations [Ermakova et al, 2000]. Thus it might be caused by plasma density perturbation. Further details of the factors that could lead to IAR eigenfrequency separation change would be discussed later in this chapter and in Chapter 7.

Obviously the eigenfrequencies of a resonator are dominated by the size of the resonator and the group velocity of wave propagation within the resonance cavity. It should be noticed that the Alfvén wave is reflected by the gradient of the Alfvén velocity profile on the top of the ionosphere. Thus it is necessary to investigate the factors that dominate the Alfvén velocity.

Equation 3.2 is the relation of the Alfvén velocity.

$$V_A = \frac{B}{\sqrt{\mu_0 m_i n_i}} \tag{3.2}$$

where V_A is the Alfvén velocity, B is the magnetic field, m_i is the average mass of the ions, n_i is the plasma number density, and μ_0 is the vacuum permeability, respectively. In the study in this chapter it is assumed that the difference of the eigenfrequencies of different stations could be dominated by the difference of the geomagnetic field or the V_A profile among those stations. Due to the limited data support it is very difficult to estimate the impacts caused by the average mass of ions. This assumption will be further tested later in this chapter. In order to find out the main factor, it is necessary to further analyse the eigenfrequency distribution during the whole lifetime of the IAR event.

Fig 3.11 illustrates the eigenfrequency separation variations observed at the 5 stations during the lifetime of the IAR. Spots are observed values. Each spot represents a sinusoidal curve fitting result on a selected spectrum slice. The lines are the mean variations during the period. The mean variation rate of each station is displayed under the corresponding panel. According to those average changing rates of the IAR eigenfrequency separations, there were great differences on the IAR eigenfrequency separation variation rates. The maximum eigenfrequency separation variation rate was observed at KIL, which was 1.358 mHz/min, while the minimum was observed at ROV, which was 0.3353mHz/min. The minimum eigenfrequency separation variation rate was approximately 1/4 of the maximum. One of the factors that led to the difference is the differences of the latitudes and longitudes of those stations. The differences of the latitudes and longitudes led to different variations of zenith angles at those stations, which dominated the diurnal plasma density variation of the ionosphere. However, by referring Fig 3.4 and Table 3.1, the differences of the latitudes and longitudes are not great enough to lead such great differences. Thus there should be some other factors made contribution to the IAR eigenfrequency separation variations. According to previous discussions, those factors should be able to influence the local geomagnetic field or local plasma density of the ionosphere.

The local IAR eigenfrequencies fluctuate frequently. This has been discussed in section 3.4. However, more details were revealed by analysing the event observed by multiple stations. The eigenfrequency variations of every two neighbouring stations were compared in the four panels of Fig 3.12, respectively. Blue lines always denote the eigenfrequency separations obtained at the station at relatively higher magnetic latitude, and red lines illustrate the eigenfrequency separations obtained at the station at relatively lower magnetic latitude. It can be seen that in all of the four panels, the eigenfrequency separations obtained at all the stations show a general trend of increasing. The fluctuations are similar in every two neighbouring stations. However, red lines and blue lines cross each other frequently in all of the four panels. That means the geomagnetic latitude is not the only dominant factor for the IAR eigenfrequency separation, in others words, by ignoring the change of the ion mass, the plasma density profile is probably the more significant factor.

Fig 3.13 illustrates the geomagnetic field and the eigenfrequency variation in Sodankylä from 16UT to 19UT on 9 November 2002. The data of the geomagnetic field was from the official website of Sodankylä Geophysical Observatory of University of Oulu, Norway (http://www.sgo.fi/Data/Magnetometer/magnData.php). The time resolution of the geomagnetic data is 1 minute. The left panel illustrates the geomagnetic field variation and its average variation during the period of 16UT to 19UT, 09/11/02. The average changing rate was 0.0077nT/min during the 3 hours. The total changing percentage during the period was just about 0.15%, which is small compared to the IAR eigenfrequency separation variation rate (changed by more than 20%). The right panel illustrates the eigenfrequency separations of the IAR observed at Sodankylä versus the local geomagnetic field. There was not any clear or systematic relationship between the two. Referring to both Fig 3.12 and Fig 3.13, the eigenfrequency separation variations and fluctuations appear to be quite local. Thus the eigenfrequency separation variations and fluctuations were dominated by local ionospheric plasma density variations and perturbations. Further evidences to support the point will be available in the next section.

Another important question that needs to be answered is why the SRS signals on the dynamic spectrum of KIL and OUL were invisible on the dynamic range of the plot. In most of the previous studies, an IAR event was defined by the existence of SRS signal on the dynamic spectrum. However, in this event, there were no SRS signals in KIL or OUL though the IAR event was still observed by the two stations. That implies that in previous statistic works some IAR events might be neglected because of the invisible SRS signals. Since the SRS signal is invisible, the corresponding IAR would not be counted in a study which utilized the traditional way to identify IAR events.

In Fig 3.3 it can be seen that the SRS signals in SOD and NUR were clearest. The SRS in the panel of ROV was less clear than SOD and NUR. However, it was still visible. There were no visible SRS in the panels of KIL and OUL. As mentioned earlier in this section, the variations of eigenfrequency separation of the IAR were found to differ at different stations. There were fluctuations of eigenfrequency separation observed in all the stations. Fig 3.14 illustrates such fluctuations of all the stations. The left panel illustrates the dynamic spectra of LHC of the five stations. The right panel illustrates the mean variations of the IAR eigenfrequency separations of the five stations in the period of 16UT to 19UT. The error bars denotes the differences between mean and real eigenfrequency separations of the selected intervals of curve fitting. The *err* showed in each sub-panel was calculated by equation 3.3.

Suppose the total number of the selected dynamic spectrum slices was N, a variable *err* for estimating the intensity of fluctuations of eigenfrequency separations can be defined as:

$$err = \frac{\sum_{n=1}^{N} | F(n) - f(n) |}{N} \tag{3.3}$$

where $F(n)$ is the eigenfrequency separation of the nth slice. By doing a linear curve fitting the mean eigenfrequency separations in a certain period can be obtained. Based on the linear fitting, for each F(n), there is a corresponding mean eigenfrequency separation $f(n)$. Thus the *err* is the mean difference between the real and the mean

eigenfrequency separations for an individual station. The differences between the real and the mean eigenfrequency separations are the fluctuations, thus *err* denotes the mean magnitude of the fluctuations of the eigenfrequency separations. The absolute value of *err* for each station can be seen on the right of each sub-panel in Fig 3.14. The unit of *err* is Hz. Greater *err* denotes more intensive fluctuations of eigenfrequency separations.

It can be seen that the maximum of the mean eigenfrequency fluctuation occurred in KIL, and the second greatest *err* value was obtained in OUL. The minimum was obtained in SOD, which is just 0.0151, less than 1/4 of the maximum. The value obtained in NUR is 0.0273, which is also quite small. The medium *err* value was obtained in ROV. Referring to the left panel of Fig 3.14, it can be seen that the SRS signals were invisible when the *err* values were quite big; the SRS signals were quite clear when the *err* values were quite small. Considering that the SRS signal in ROV was visible but not quite clear, and the SRS signal in OUL was invisible, the threshold for the visibility of SRS should be between 0.04 and 0.05. Considering each sliding window covered two minutes in the observation, the threshold should be between 0.020Hz/min and 0.025Hz/min, i.e., if the eigenfrequency separation varies quicker than 0.025Hz/min, the SRS signal of the IAR would be invisible.

However, when there are intensive fluctuations of IAR eigenfrequency separations, the SRS could be invisible but exist, like the IAR event observed by KIL. Thus the previous statistic works of IAR based on SRS just studied the events without strong fluctuations of eigenfrequencies.

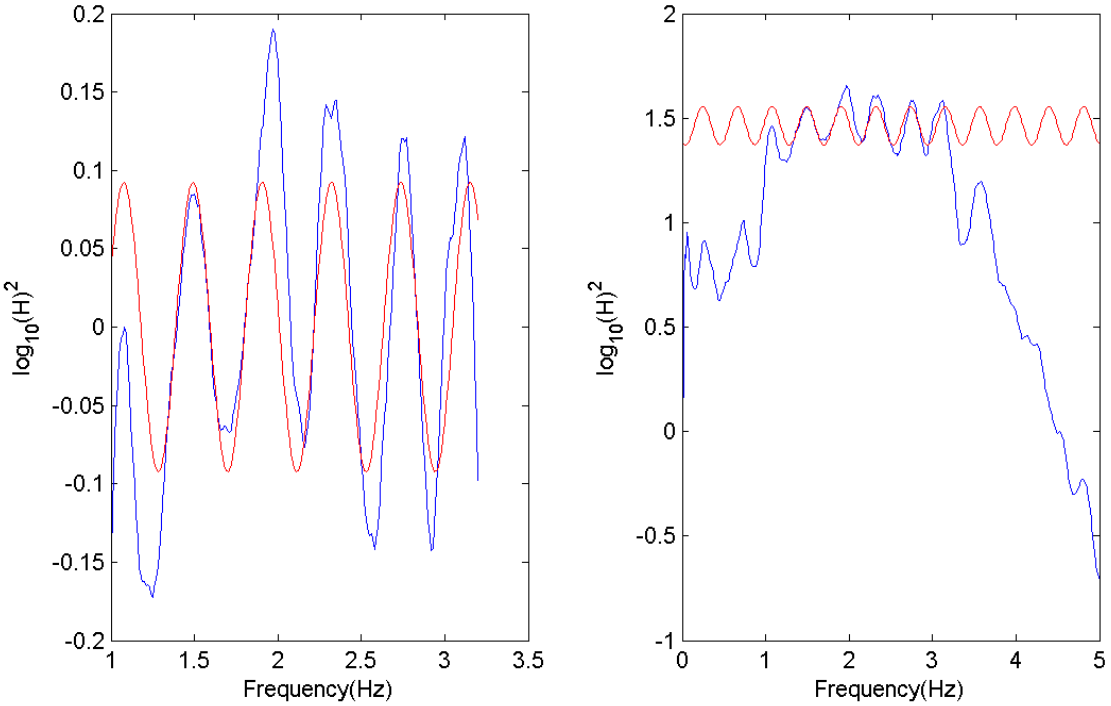

Fig 3.7 The left panel shows the curve fitting result on the interval from 1-3.2Hz on double-smoothed data. In the right panel the fitted curve are extended in order to compare with the single-smoothed data.

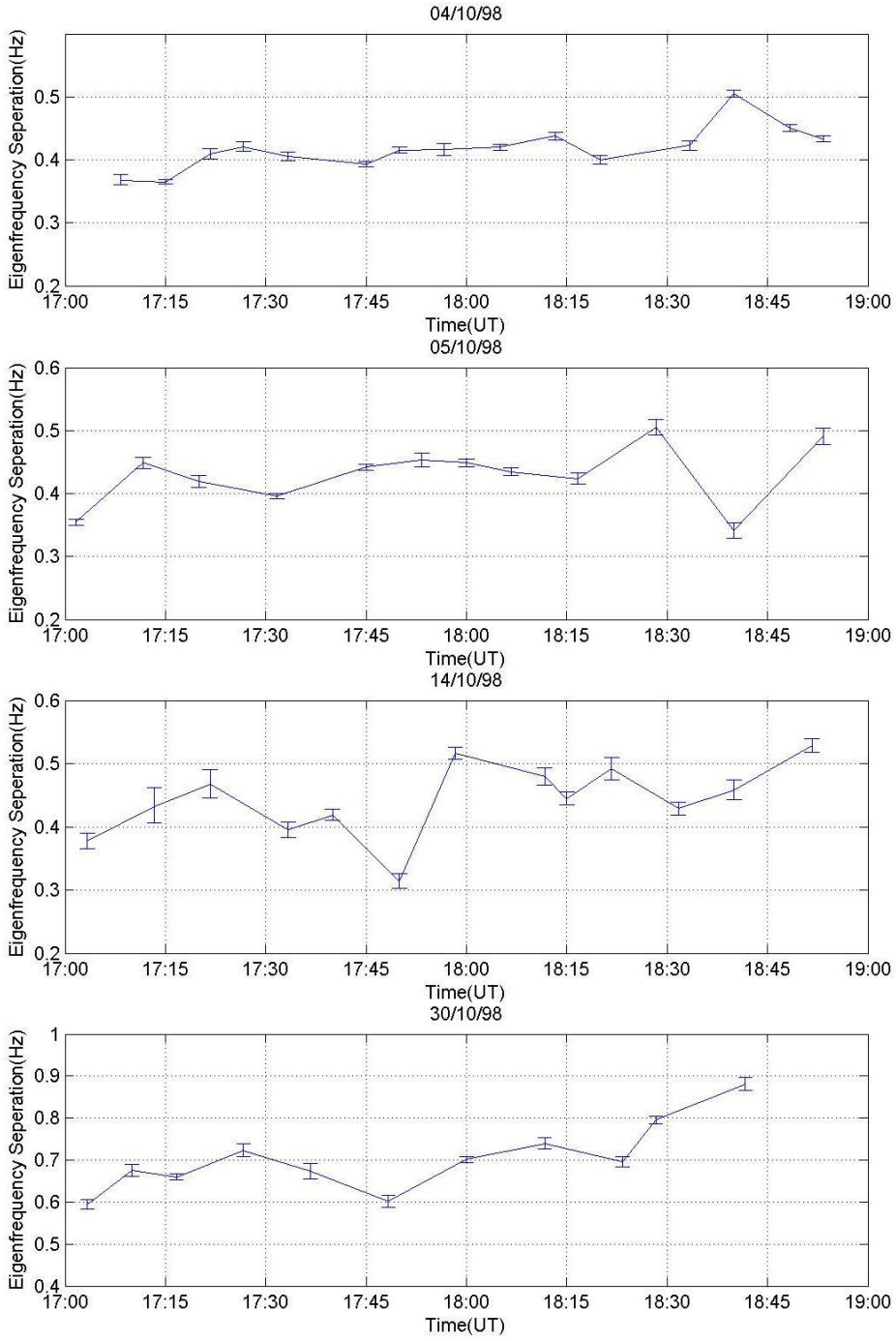

Fig 3.8 The eigenfrequency variations of the four IAR events observed on 04/10/98, 05/10/98, 14/10/98 and 30/10/98, respectively. The common time intervals selected to study the four events are from 17:00UT to 19:00UT, which covers two hours. The error bars denote the confidence boundaries of 95% of the curve fittings.

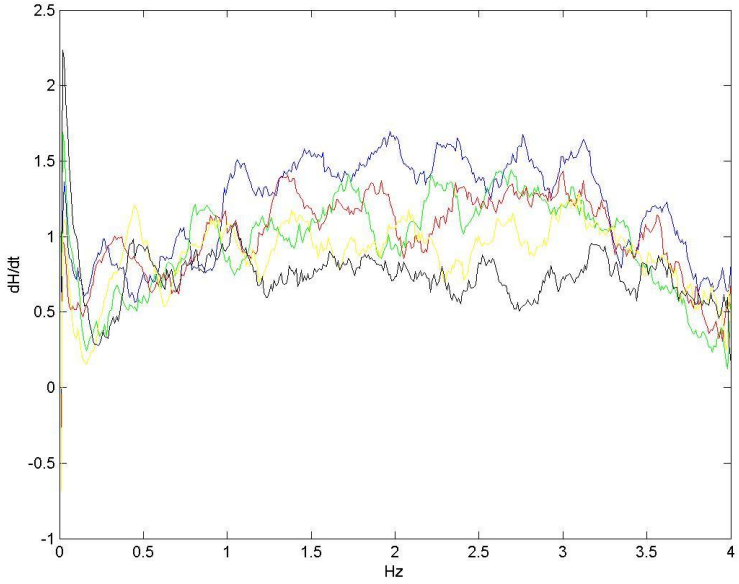

Fig 3.9 The plot shows the single running average of logarithm spectrum slices on the band of 1-3.2Hz. The blue line, the green line, the red line, the yellow line and the black line represent time intervals of 17:50:00UT-17:51:40UT, 19:13:20UT-19:15:00UT, 20:36:40UT-20:38:20UT, 22:00:00UT-22:01:40UT and 23:23:20UT-23:25:00UT, respectively.

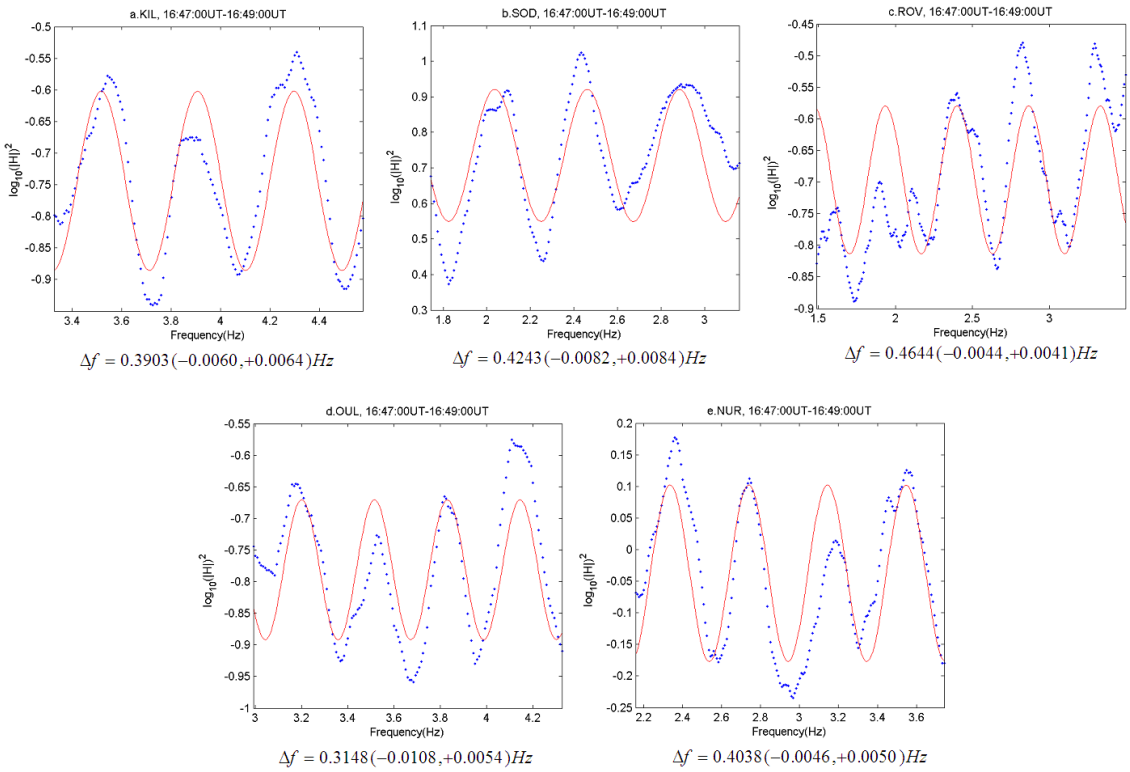

Fig 3.10 The plot shows the sinusoidal curve fitting of the five stations at the same time interval. The latitudes of the stations are getting lower from panel a to panel e. The eigenfrequencies and the confidence boundaries of each station are displayed below each corresponding panel.

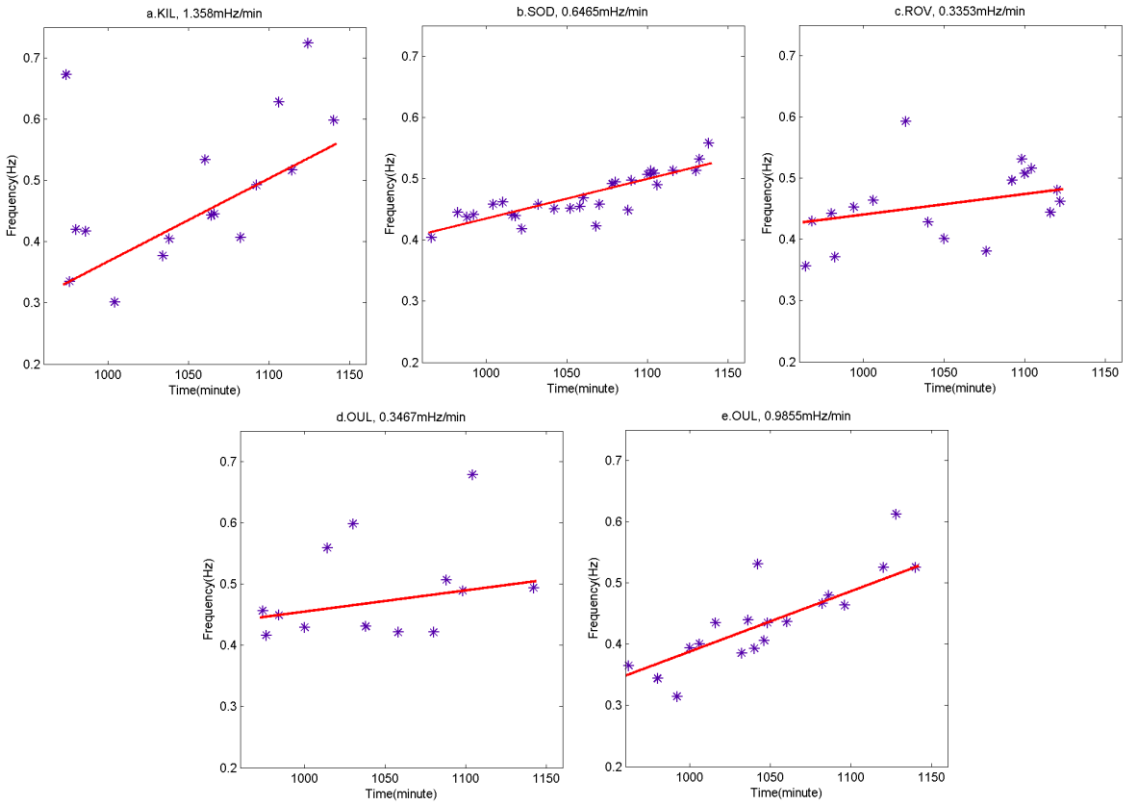

Fig 3.11 The eigenfrequency variations observed at the five stations. Asterisks are observed values. The lines are the mean variations during the period. The mean eigenfrequency variation rate of each station is displayed under the corresponding panel.

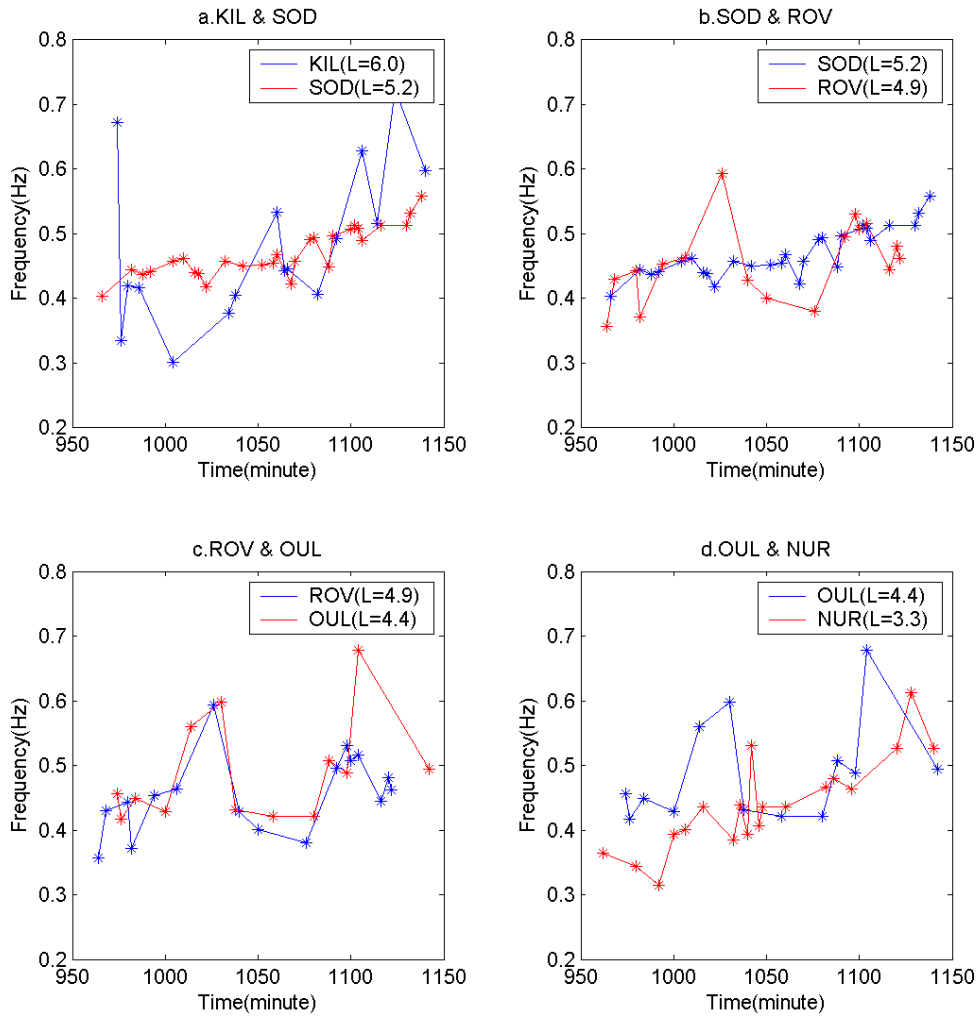

Fig 3.12 The comparison of eigenfrequency fluctuations between every two neighbouring stations. Blue lines always illustrate the eigenfrequencies observed at the station at relatively higher magnetic latitude, and red lines illustrate the eigenfrequencies observed at the station at relatively lower magnetic latitude.

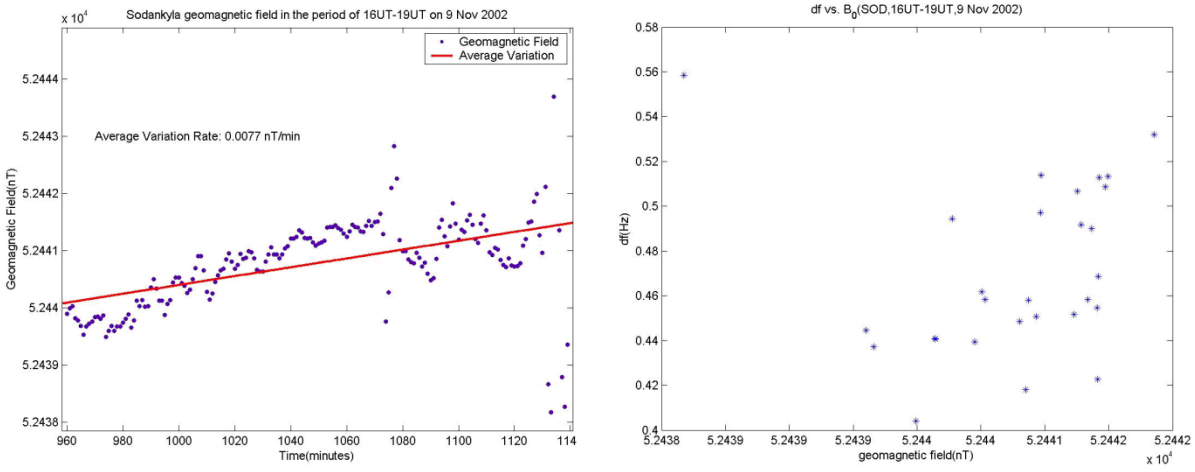

Fig 3.13 The left panel illustrates the geomagnetic field variation and its average change. The right panel illustrates the eigenfrequency of the IAR observed at Sodankyl äversus the local geomagnetic field.

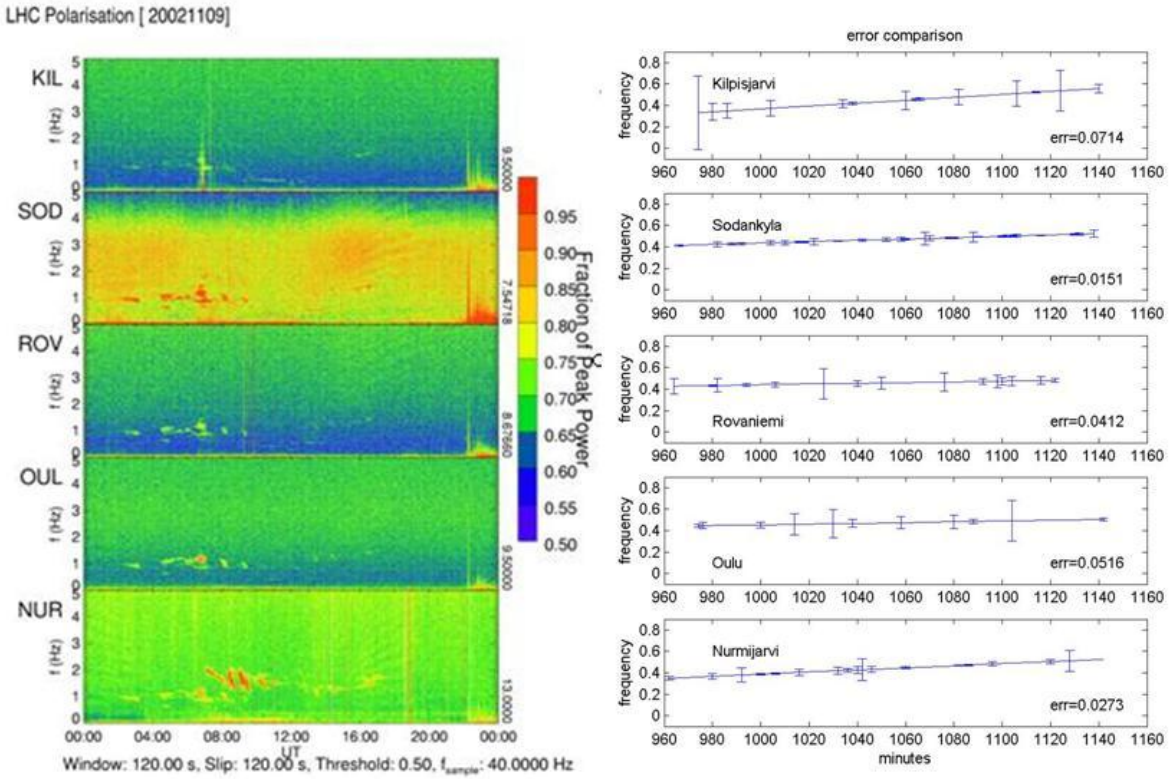

Fig 3.14 The left panel illustrates the dynamic spectra of LHC of the five stations. The right panel illustrates the mean variations of the IAR eigenfrequency separations of the five stations in the period of 16UT to 19UT. The error bars denotes the differences between mean and real eigenfrequency separations of the selected intervals of curve fitting.

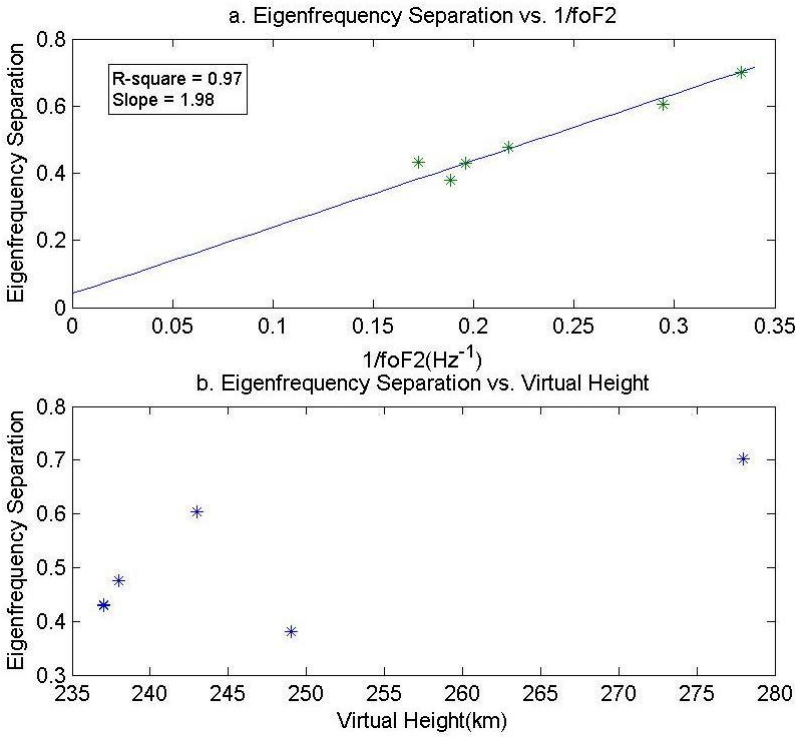

Fig 3.15 The events showed in the plot was observed in October 1998 at SOD. Each asterisk represents a time interval of curve fitting. Detailed information and parameters of the selected time intervals can be seen in Table 3.2. The upper panel shows the eigenfrequency separations against the reciprocals of foF2. The lower panel shows the eigenfrequency separations against the virtual heights.

Event No.	1	2	3	4	5	6
Date	04/10/98	04/10/98	05/10/98	14/10/98	30/10/98	30/10/98
Time(UT)	18	19	18	18	17	18
Time(LT)	20	21	20	20	20	21
foF2(MHz)	5.8	5.3	5.1	4.6	3.4	3.0
Virtual Height(km)	237	249	237	238	243	278
ES*(Hz)	0.4318	0.3803	04398	0.4760	0.6042	0.7016

Table 3.2 The detailed information and parameters for Fig 3.15.

ES is short for Eigenfrequency Separation.

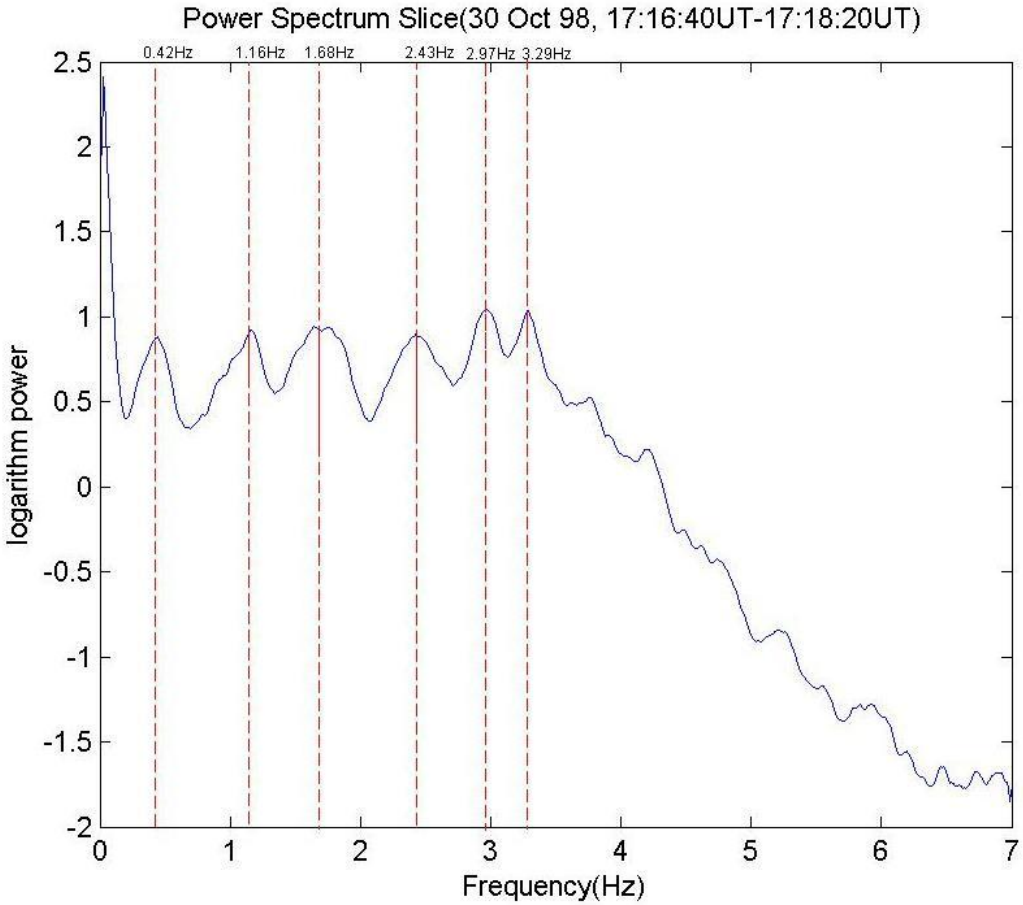

Fig 3.16 The plot shows an example of IAR of non-uniform eigenfrequencies. In other words, the eigenfrequency separations are not equivalent. The time interval is showed at the top of the figure. The dashed lines denote the peaks of the power spectrum. The exact frequencies of the peaks are showed above the dashed lines.

All the previous statistical studies of IARs were based on the signals of SRS. However, in this section it indicates that the SRS could be invisible due to the intensive eigenfrequency fluctuation while the periodic structure could be seen in single dynamic spectrum slices. Thus, considering the eigenfrequency fluctuations of IARs are dominated by local plasma density variations and perturbations, the previous statistical studies of IAR events just investigated the events occurred in 'quiet' or 'quasi-quiet' ionospheric plasma density profiles, which means the plasma density profile did not change intensively nor frequently during the period of the IAR life time.

3.6 Further Discussion and Analysis

The Alfvén velocity is a function of the background geomagnetic field, and the plasma mass density. Based on the discussion and the analysis showed in section 3.4 and 3.5, the eigenfrequency separations are more likely to be dominated by local ionospheric plasma density. However, all the evidence showed in section 3.4 and 3.5 are indirect. Fig 3.15 shows direct evidence.

The events showed in Fig 3.15 were observed in October 1998 at SOD. Each asterisk represents a time interval of curve fitting. Detailed information and parameters of the selected time intervals can be seen in Table 3.2. The foF2 data is available on the website of Sodankylä Geophysical Observatory (http://www.sgo.fi/Data/Ionosonde/ionData.php). The theoretical relation between the foF2 and the eigenfrequency separation is explained in more detail later in this section (the eigenfrequency separation should be proportional to the reciprocal of foF2, see Equation 3.4 to 3.10). Panel a shows the eigenfrequency separations against the reciprocals of foF2. Panel b shows the eigenfrequency separations against the virtual heights. In panel a it can be seen that the eigenfrequency separations are proportional to the reciprocals of foF2. The blue line is the linearly fitted line for the asterisks. The line crosses the y-axis at the value of about 0.04, which is quite close to the origin compared with the scale of the y-axis. The intersection of the line and the y axis is at y=0.04,

which is relatively small. There are two possible reasons that why the line does not cross the origin. The first reason is that it is purely caused by errors. The other reason is that it is caused by the difference of the bottom boundary conditions of IARs. The ratio of the Pedersen conductivity and the wave conductivity at the E peak could be a very significant parameter to control the eigenfrequencies detected on the ground. It will be discussed in more details in Chapter 6. However, for Fig 3.15, it can be seen that all the intervals were selected from the period of 20LT to 21LT, and all the events were observed in a single month at the same location. It implies that the ratio between the Pedersen conductivity and the Alfvén wave conductivity at the E peak should be close for all of the six time intervals plotted in Fig 3.15. Thus the difference between the intersection on the y axis and the origin seems more likely to be errors. In panel b there is no systematic relation can be seen between the eigenfrequency separations and the virtual heights.

The eigenfrequencies of an IAR event correspond to zeros of a Bessel function if the Alfvén velocity profile was considered to be exponential above the F2 peak and a constant below the F2 peak [Lysak, 1991]. However, as it mentioned in section 3.3, normally the eigenfrequency separations could be considered to be a constant. That means the resonance cavity was considered to be an idealized resonator. The Alfvén velocity within the cavity is assumed to be uniform. Both the upper and the lower reflective boundaries are supposed to be thin layers. The thickness of the boundaries is ignored. According to Lysak [1991], typically the effective length of the idealized resonance cavity is about 1000km.

For an idealized resonator,

$$f(N) = \frac{NV_A}{2L} \tag{3.4}$$

$$\Delta f = f(1) = \frac{V_A}{2L} \tag{3.5}$$

where f is the eigenfrequency, Δf is the eigenfrequency separation, $N \in \{1,2,3,...\}$, V_A is the Alfvén velocity within the cavity and L is the length of the cavity.

Considering the foF2 is electron plasma frequency, thus for foF2, the expression is,

$$foF2 = \sqrt{\frac{e^2 n_e|_{F2\,peak}}{m_e \varepsilon_0}} \tag{3.6}$$

where n_e is the electron number density, e is the electron charge, m_e is the electron mass and ε_0 is the vacuum permittivity.

The ion number density and electron number density is equivalent.

$$n_e = n_i \tag{3.7}$$

For the idealized resonance cavity the uniform plasma density within the cavity is proportional to the density at the F2 peak, thus for the uniform density,

$$\omega_{pe} = \alpha foF2 \tag{3.8}$$

where α is the coefficient.

According to equation 3.2, 3.5, 3.6, 3.7 and 3.8

$$\Delta f = \frac{Bec}{2L\alpha foF2}\sqrt{\frac{1}{m_i m_e}} \tag{3.8}$$

where c is the speed of light. Thus,

$$\Delta f \propto B \tag{3.9}$$

and,

$$\Delta f \propto \frac{1}{foF2} \tag{3.10}$$

when m_i almost keeps a constant in the idealized cavity, i.e., the mean mass density of ions in 1000km above the E peak is almost a constant, and the percentage of the each species of ions does not change. According to equation 3.9 and 3.10, the eigenfrequency separations are proportional to local geomagnetic field intensity and the reciprocal of foF2. In Fig 3.13 and Fig 3.15, it can be seen that the IAR eigenfrequency separations are dominated by foF2, i.e., by local plasma density of the ionosphere.

All the IAR eigenfrequency separations studied in this chapter can be treated as equivalent for an individual spectrum slice; however, it is not always true. As it mentioned earlier in this section, theoretically the eigenfrequency separation is more likely to be a Bessel function. Fig 3.16 shows that the realistic case could be more complicated.

Fig 3.16 illustrates the power spectrum slice of the time interval of 17:16:40UT to 17:18:20UT on 30/10/98 at SOD. The dashed lines highlight the peaks on the curve, which correspond to eigenfrequencies of the IAR in the interval. The corresponding frequency of each peak is showed on the top of the dashed line. Thus the eigenfrequencies below 4Hz are 0.42Hz, 1.16Hz, 1.68Hz, 2.43Hz, 2.97Hz and 3.29Hz, respectively. Due to the response curve of the pulsation magnetometer the detected signal intensity declines from about 3.5Hz, thus the small peak from 3.5Hz to 4Hz is not considered as the sign of an eigenfrequency. The fundamental eigenfrequency is 0.42Hz. The eigenfrequency separations are 0.74Hz, 0.52Hz, 0.75Hz, 0.54Hz and 0.32Hz, respectively. The minimum is less than half of the maximum. Those eigenfrequency separations cannot be explained if the resonance cavity is considered as an idealized resonator. More realistic conditions of the cavity need to be taken into account. It will be studied numerically in more details in Chapter 7.

3.7. Summary and Conclusion

There are 13 IAR events observed in October 1998 at Sodankylä. Four of those were selected to be analysed. The dates of the four events are 04/10/98, 05/10/98, 14/10/98 and 30/10/98, respectively, which cover the beginning, the middle and the end of the October. For all of those events, the period of 16UT to 19UT was the common interval that IARs existed.

The IAR eigenfrequency separations for a certain time interval (100s for the 13 events detected by a single station in 10/98 and 120s for a single events detected by multiple stations on 09/11/02) could be considered as a constant. In such a case the double running average methods was used to smooth the dynamic spectra data. Also, a sinusoidal curve fitting method was utilized to find the constant eigenfrequency separations for each dynamic spectrum slice. By investigating the eigenfrequency separations of the five IAR events, it is found that the IAR eigenfrequencies increase in the afternoon generally. However, there are fluctuations on the eigenfrequencies. On 14/10/98, the eigenfrequency separations increased for around 60% in 17:45:00UT to 18:00:00UT. For all of those events, the eigenfrequency separations could fluctuate in less than 10 minutes.

In addition, on 09/11/02, a single IAR event was observed by 5 Finnish pulsation magnetometers simultaneously. The magnetometers are at different locations. Also based on utilizing the double running average and sinusoidal methods for finding the eigenfrequency separations, it was found that the eigenfrequency separations are different at different locations. Also, the eigenfrequency separations fluctuated. The fluctuation could lead to the invisibility of SRS structures on dynamic spectra. According to the dynamic spectra of the five events, the threshold of the rate of eigenfrequency separation fluctuation is between 0.020Hz/min and 0.025Hz/min, i.e., the SRS would be invisible when the fluctuation of eigenfrequency separations is higher than 0.025Hz/min though there is IAR detected. Weaker fluctuations make the SRS more visible.

By supposing the IAR is an idealized resonance cavity, the IAR eigenfrequencies are dominated by local plasma density profiles, not local geomagnetic field intensity in the ionosphere. For the events observed in October 1998 studied in this chapter, it implied that the ionospheric plasma density at high latitudes could change for 30% in 10 minutes according to equation 3.2. Considering that although a pulsation magnetometer just measures the magnetic field intensity at its position, however, the field intensity is dominated by a huge area around the position of the magnetometer, the measurements by a pulsation magnetometer reflect the information of the certain area around the location of it. Thus, considering the distance between every two neighbouring pulsation magnetometers utilized in this chapter, the scale of the horizontal ionospheric plasma density structure is smaller than 200km at high latitudes. On the other hand, considering that the upper reflective layer of the resonance cavity is the gradient of the plasma density profile above the F2 peak, and the effective length of the resonance cavity is 1000km, it can be concluded that the scale of the nonuniformity of ionospheric plasma density structure in 1000km above the E peak at high latitudes is less than 200km.

Chapter 4. IARs Observed in Antarctica

4.1. Introduction

Since Polyakov [1976] first predicted the existence of the IAR, all the IAR events studied so far at high latitudes were observed at Northern hemisphere. Some of them were observed by pulsation magnetometers in Arctic regions. For example, the IAR events studied in Chapter 3 were detected by 5 stations. One of the stations is in the Arctic, i.e., the Kilpisjärvi station, and other 4 stations are equatorwards of Arctic Circle. Based on the observations and data interpretations of IAR events observed at high latitudes, a lot of details of Magnetosphere-Ionosphere coupling (MI coupling) have been revealed [e.g., Parent et al., 2010; Yeoman et al., 2008]. However, the IARs in southern hemisphere are also quite significant in coupling the magnetosphere and the ionosphere. In this chapter the study will aimed at characterizing the IAR features in Antarctica. The annual and seasonal IAR occurrence in Antarctica will be investigated. Also, the relation between the IAR occurrence and sunspots number will be briefly discussed and compared with the study by Trakhtengerts et al [2000b]. The source of oscillation of IARs will be discussed based on the statistical study.

The data were obtained at Halley Bay Station. Fig 4.1 is the exterior view of the station. Halley Bay Station was built for scientific activities in Antarctica in 1956. The station which is now referred to as the Halley Research Station is operated by British Antarctic Survey (BAS). It is located at 75°35'S, 26°34'W. The L shell value of the station is 4.3. Considering its high geographic latitude, the L shell value of the station is relatively small. According to the geographic longitude of the station, the time difference between Halley Research Station and universal time can be worked out. Universal time is two hours prior the local time of Halley Research Station. The sampling frequency of the pulsation magnetometer at the station is 10Hz, which is lower than the sampling frequency of the magnetometers utilized in chapter 3. That means the time resolution of

the signals is 0.1s. The frequency band of interest in this study of IARs is about 0.1Hz to 5Hz. Thus the 10Hz sampling frequency is good enough to do the study in this chapter.

4.2. A Brief Introduction to the Events

In order to identify the IAR events, all the SRSs were analysed by quick dynamic spectra and tested to confirm that whether a SRS denotes an IAR event. Quick views of dynamic spectra were available on the website of the Space Physics Department of Augsburg College (http://space.augsburg.edu/). Fig 4.2 illustrates an example of SRS on the quick dynamic spectrum. Quick view means that there was no threshold for plotting or particular window for FFT processes. The date of the example is 28 Sep 2008, which was the 272nd day of the Year. It should be noticed that the time in the quick plot is universal time. The colour bar on the right illustrates the fractional power level of the dynamic spectrum. From the top to the bottom, the panels illustrate the dynamic spectra of X, Y and Z components, respectively. X component is the N-S component, which was called H component sometimes. Y component is the E-W component, which was called D component sometimes. The maximum of the concerned band shown in the plot is 5Hz. Normally the Z components were not concerned in studies of IARs. It can be seen that the SRS is clear on the Y components. It is also visible on the X components. But the SRS on the X components is not as clear as on the Y components. Actually this is a common feature of the IAR events observed at Halley Research Station. The feature will be discussed later in this chapter. The SRS occurred at about 20UT, and became clearer later. The eigenfrequency increase with time can be seen on the quick spectrum. The SRS lasted till 24UT on the spectrum plot. Thus it can be supposed that the SRS also exists in the early morning on the next day in universal time. Considering the time difference between the local time and the universal time, it is necessary to re-plot the data in local time. Also, it is necessary to notice that there could be continuous IAR events that cross two days or even last several days. Thus it could be expected that there could be continuous SRS, which crosses 24LT and last till the next day or several days later.

Fig 4.3 illustrates the dynamic spectrum of the same day in local time. The Z components were not illustrated in Fig 4.3. The levels of renormalized fractional powers were illustrated by the colour bar on the right of each panel. In order to make the SRS signals clearer in dynamic spectra, it is necessary to set a threshold for each spectrum plot. The threshold is the percentage of the peak power. The power above the threshold will not be displayed on the spectrum plot. The peak power was artificially set to be at 3Hz in all the spectrum plots in this chapter. The threshold was set to be 85% for both of two panels. This is a quite high threshold, thus a lot of blank space and points can be seen on the dynamic spectra. Those blanks represent the powers below the threshold. The oscillation of the first eigenfrequency started at about 18LT, which is earlier than the starts of other eigenfrequencies. The width of the sliding window was set to be 100s, which covers 1000 sampling data points. The distance of the sliding was 100s, thus there was no overlap between every two neighbouring windows. The geomagnetic field had been removed from the raw data of the dynamic spectrum. Thus the spectrum just illustrates the power of magnetic pulsations. The power illustrated in both of the two panels had been renormalized. The referred peak power, which was the maximum power at 3Hz, was illustrated to the right bottom of each panel. All the data points displayed in the two panels were the logarithm values of the spectrum data. It can be seen that the intensities of the referred peak powers of the two components are quite close. The SRS of the X components were not as clear as in the Y components. The separations between the eigenfrequencies were not quite clear. It implied that the resonance of the X components were not as strong as in the Y components. It can be seen that the SRS became weaker with time till it reached 24LT. However, it did not disappear around 24LT. That implied that the SRS could be continuous till the next day. For example, according to Table A2 in the APPENDIX, there were IAR events every day during the period of 19/09/09 to 25/09/09, which covers 7 days. In some of the 7 events, there were SRS signals at 24LT and lasted till the next day or more than one day later.

However, the dynamic spectrum is not sufficient to identify an IAR event. Some of the structures that look like SRS are not real SRS. Thus it is necessary to check the

polarization features of the IAR. For example, in 2005 there was a quite clear harmonic structure on a daily dynamic spectrum, however, the analysis shows there was only linear polarization in the harmonic structure. Thus, that harmonic structure was believed to be the instrument systematic error. Fig 4.4 illustrates the Left Hand Circular (LHC) polarization spectrum and the Right Hand Circular (RHC) polarization spectrum of the same day. The SRS are also visible on the two panels. The powers illustrated were renormalized referred to the peak power of the components at 3Hz. The referred power is illustrated to the right bottom of each panel. The colour bars on the right show the levels of the fractional powers. All the IAR events studied in this chapter were confirmed by checking the SRS signals of LHC and RHC.

4.3. IAR Occurrence at Halley Research Station

All the data obtained in the period from 1 Jan 2005 to 31 Dec 2009 at Halley Research Station has been surveyed. The period covers 5 years. The study was carried on in 2010, and the seasonal and annual variations of IAR occurrences were investigated, thus the events of 2010 were not taken into account in this study. There were also some data gaps in the period of 2005 to 2009. The dates of the data gaps can be seen in Table 4.1.

It can be seen that all of 1826 days of the five years, there were 1758 days in which the pulsation magnetometer data was available. Thus the percentage of the data coverage of the five years is 96.28%. Particularly the data coverage of 2008 and 2009 is 100%. The relatively low data coverage rate is in 2005, which is 87.67%. The exact dates of the data gaps are also listed in the table.

Fig 4.1 The exterior view of Halley Research Station. The picture was from the website of British Antarctic Survey.

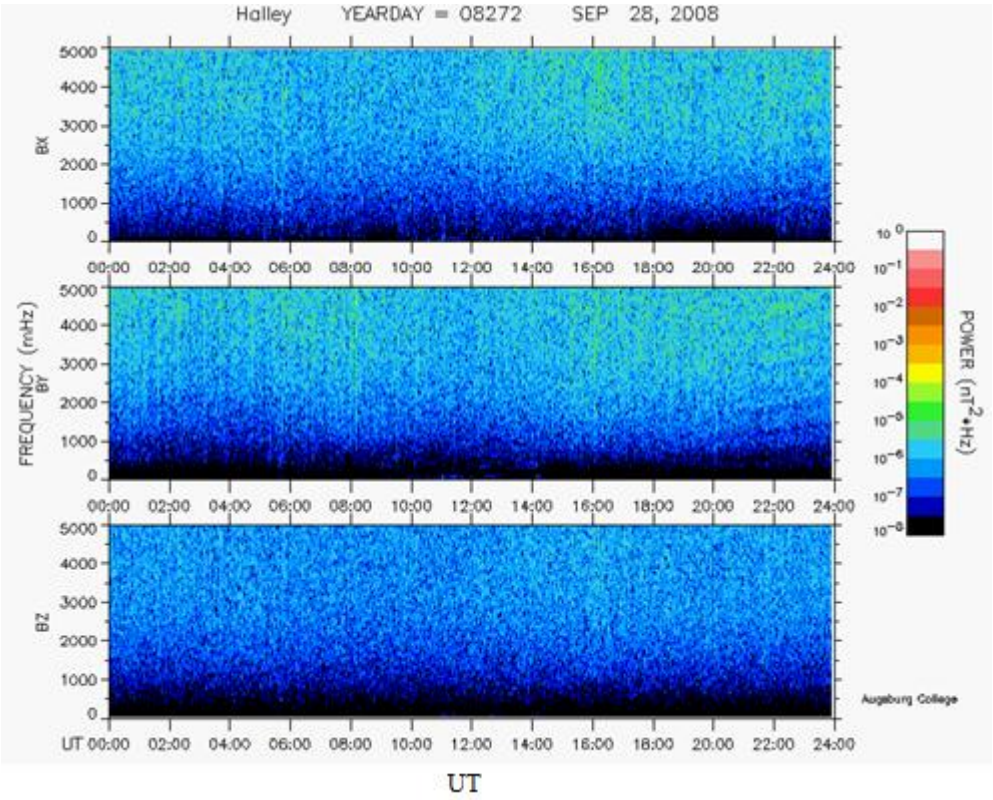

Fig 4.2 An example of SRS on quick plots of dynamic spectrums. The date of the spectrum is 28 Sep 2008. The levels of the renormalized fractional powers are illustrated by the colour bar on the right.

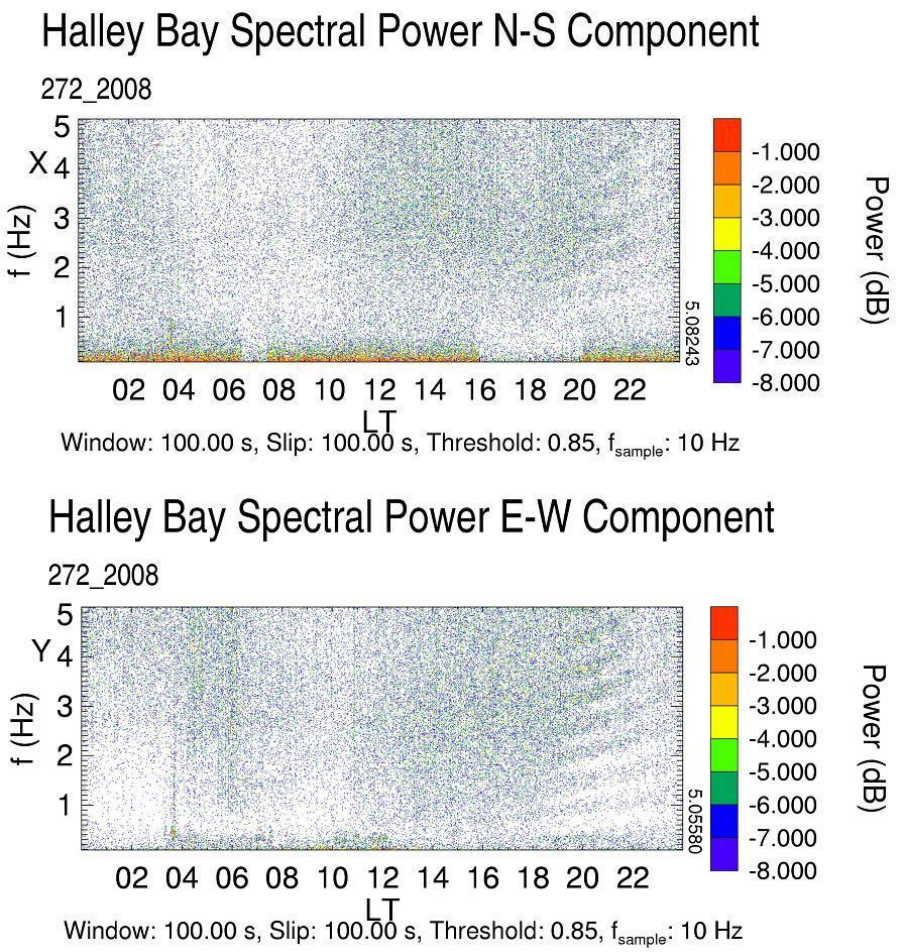

Fig 4.3 The dynamic spectrum of 28 Sep 2008 of Halley Research Station. The upper panel and the lower panel illustrate the X and Y components, respectively.

Totally there were 37 IAR events confirmed during the period. The dates of the events are listed in A2 of the Appendix. It can be seen that the number of the events increases with Year. There was only one event observed in 2005, and 23 events in 2009. The number of the events reached the maximum in 2009. However, 37 in 5 Years is a small value for the occurrence comparing with the IAR occurrence at Northern hemisphere [Semenova and Yahnin, 2008]. According to the study in Chapter 3, it can be supposed that there should be more than 37 events. The 37 events found during the five Years were just observed when the ionospheric conditions were quasi-stable, thus the eigenfrequencies did not fluctuate too frequently or intensively. The sampling frequency of the magnetometer is 10Hz, which is relatively low comparing with the magnetometers utilized in Chapter 3, which are 20Hz and 40Hz. Thus the time resolution of the data obtained at Halley is not as good as the resolution of the Finnish magnetometers, i.e., the time resolution is 1/2 of the events observed in 1998 and 1/4 of the event observed in 2002. Unfortunately the detailed upgrade information of the magnetometer in Halley Research Station is not available, thus the systematic effects on the occurrence caused by the magnetometer were not taken into account in this chapter.

There has been study on IAR diurnal behaviour at high latitudes [Semenova and Yahnin, 2008]. However, there was no presented work of IAR annual and seasonal behaviour in high latitude region at southern hemisphere. Fig 4.5 illustrates the annual distribution and the monthly distribution of the IAR events. The left panel illustrates the annual distribution of the events while the right panel illustrates the monthly distribution. From the left panel it can be seen that the number of the events increase Year-by-year in 2005 to 2009. From the right panel, it can be seen that the IAR events just occurred in five months, which are February, March, April, September and October, respectively. The maximum of the IAR occurrence is in October. The maximum of the first half of a Year is in February. Considering that the data gaps in 2005 and 2007 cover 14 days and 1 day in February, the events in February of the two years could be more than those have been observed. However, according to the dates of events observed in 2008 and 2009 which are listed in table A2, the IAR occurrence in February is lower than in September. Thus the IAR occurrence in September is greater than in February, March or April. The right

panel shows two gaps of IAR occurrence, which are May to August and November to January respectively, during a whole Year. Considering the equinoxes are close to the two occurrence periods of a whole Year, it is worth seeing the IAR occurrence relevant to the equinoxes during the five Years. Dates of the equinoxes are listed in Table 4.2.

It should be noticed that the Halley Research Station is in southern hemisphere. Thus the equinoxes in March are autumn equinoxes (AE); the equinoxes in September are spring equinoxes (SE). Fig 4.6 illustrates the number of IAR events against time. The time in the plot was defined by equinoxes, which are shown on the horizontal axis. For example, 05AE means the autumn equinox in 2005, which is 20 March according to Table 4.2. Each grid on the horizontal axis denotes 6 months. Thus each half-grid represents 3 months, which is a season. The events numbers in Fig 4.6 are located in half-grids of the horizontal axis. Hence the plot shows the IAR occurrence in every three months.

According to Fig 4.6 it can be seen that there were 32 IAR events, which is 86.5% of all the events, occurred after the spring equinoxes, which are in September, and before the autumn equinoxes, which are in March. According to table A2 in the APPENDIX and Table 4.2 in this chapter, it can be seen that the IAR events occurred in one month prior or after the equinoxes were about 95% of all the events (35/37). The earliest IAR event of a single year around the autumn equinoxes occurred on 18 Feb 2006; the latest events of a single year around the autumn equinoxes occurred on 7 Apr 2005, which is the unique event around the autumn equinoxes occurred after the equinox; the earliest event of a single year around the spring equinoxes occurred on 19 Sep 2009; the latest event of a single year around the spring equinoxes occurred on 21 Oct 2009. According to the study by Molchanov et al [2004], the IAR occurred almost every month from July 2000 to December 2002 at middle latitudes of northern hemisphere. Also, Semennova and Yahmin [2008] found that IARs were observed in December 2005 and June 2006 at Barentsburg station which is located at $78.05°N$,$14.12°E$ (L=15), which is at high latitude region of northern hemisphere. Obviously June and December are two months prior or after the nearest equinoxes. There was no IAR observed at Halley Bay in the periods. The pulsation magnetometer data obtained at Kilpisjärvi station from 2006 to

2008 was surveyed. Unfortunately, there was no clear SRS signal in the dynamic spectra. Thus the occurrence of IARs in Antarctica is quite different from both middle and high latitude regions of northern hemisphere. The global factors in northern and southern hemispheres are almost same. Thus the differences could be led by some local factors in southern hemisphere.

According to the work by Trakhtengerts [2000b], the occurrence of IAR and the solar activities are anti-correlated. However, all the previous studies were based on the observations in northern hemisphere. It is necessary to test the relation between the Antarctic IAR occurrence and the solar activities. The sunspots number was selected to be the parameter to illustrate the intensity of the solar activities. The data was from the Solar Influences Data Analysis Centre in Belgium (http://sidc.oma.be/index.php). Fig 4.7 illustrates the sunspots number from 2005 to 2009.

The left panel of Fig 4.7 illustrates the annual sunspots number. The right panel illustrates the monthly sunspots number in 2005 to 2009. The red bars are observed sunspots numbers. The blue line is the smoothed sunspots number which could illustrate the trend of the monthly variation of solar activities during the period. It can be seen that the sunspots number reached the minimum in early 2009, and then it turned to increase. From 2005 to 2008, the solar activity was getting weaker. 2008 is a solar minimum year. The sunspots number increases quickly in late 2009, particularly in November and December. Also, there was not any sunspot in August of 2009, which means the solar activity was completely ‘quiet’ during the month and then it got back to active. Due to the quick increase of the sunspots number in late 2009, the total sunspots number in 2009 was slightly greater than 2008. Thus the anti-correlation between the solar activity and the IAR occurrence was satisfied in Antarctica, which can be seen clearly in Fig 4.8.

YEAR	D1/D2	PERCENTAGE	PERIOD
2005	320/365	87.67%	01/01/05 – 14/02/05
2006	359/365	98.36%	14/01/06 – 17/01/06
2007	348/365	95.34%	16/01/07 – 01/02/07
2008	366/366	100%	
2009	365/365	100%	
Total(2005-2009)	1758/1826	96.28%	

Table 4.1 The table shows all the dates of the gaps of data. D1 is the number of dates that the data is available of each year. D2 is the total number of days of each year. Percentage is the rates of the dates that the data is available in each year. Period is the dates of each data gap.

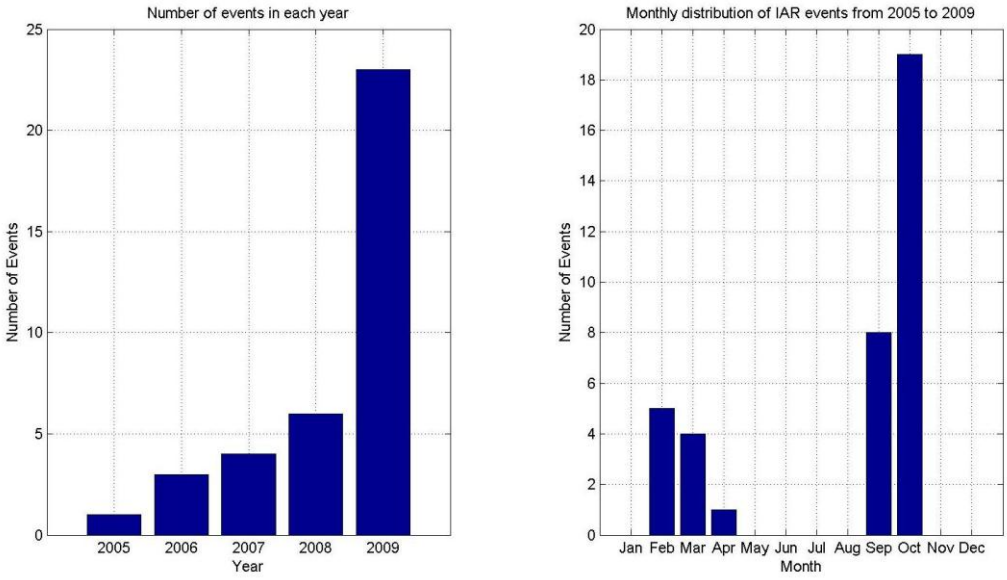

Fig 4.5 Annual and monthly distribution of the IAR events. The left panel shows the annual distribution; the right panel shows the monthly distribution.

2005		**2006**		**2007**		**2008**		**2009**	
20/03	22/09	20/03	23/09	21/03	23/09	20/03	22/09	20/03	22/09

Table 4.2 The dates of the equinoxes in the period of 2005 to 2009.

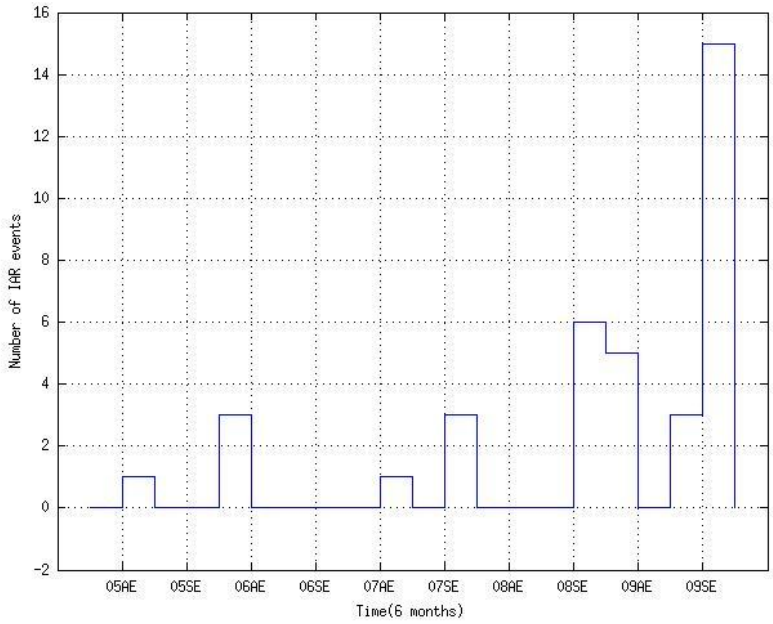

Fig 4.6 The figure shows the number of IAR events against time. The time was defined by equinoxes. AE is short for autumn equinox, and SE is short for spring equinox.

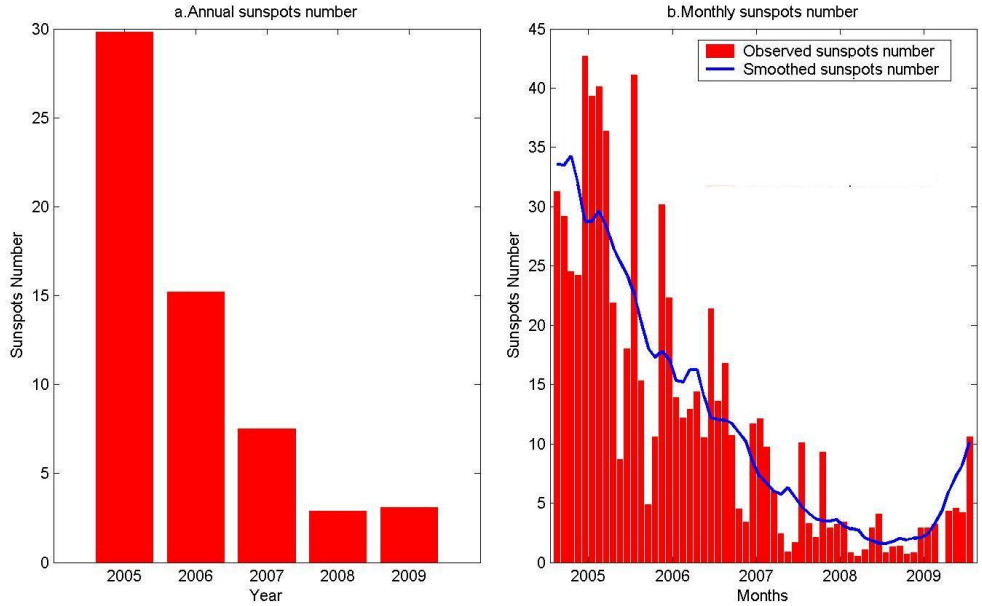

Fig 4.7 The figure illustrates the annual and monthly sunspots number. The left panel illustrates the annual sunspots number. The right panel illustrates the monthly sunspots number in 2005 to 2009. The red bars are observed sunspots numbers. The blue line is the smoothed sunspots number.

The left panel of Fig 4.8 illustrates the relation between the sunspots number of each year and the number of IAR events of the year. Each asterisk represents a year. The right panel illustrates the number of IAR events against the sunspots number of every half a year. Each asterisk denotes 6 months. From the left panel it can be seen that the anti-correlation between the solar activity and the IAR occurrence was satisfied.

4.4. The Source of Oscillation of IARs

In chapter 3 it is mentioned that the resonance power decreases with the decrease of the electromagnetic noise. In this section, more evidences are shown to support that the noise could be the source of the resonance oscillation in the IAR. The 'noise' means the non-harmonic pulsation signals. For example, the pulsation caused by lightening, or comes from the magnetosphere, or even human activities.

For the most events observed in Antarctica, the harmonic structures of Y component are clearer than X component. The feature can be seen in both Fig 4.9 and Fig 4.10. The two events were randomly selected from the 37 events. The upper panels of the figures illustrate the X component, which is the N-S component. The lower panels of the figures illustrate the Y component, which is the E-W component. High thresholds were set for the two plots. In Fig 4.9 it can be seen that the harmonic structure of the Y component is quite clear, which started at about 19UT. However, the harmonic structure of the X component is much less clear than the Y component. The harmonic structure of the Y component started at about 18LT in Fig 4.10. However, the harmonic structure of the X component in Fig 4.10 is almost invisible. The date of the event shown in Fig 4.9 is 28 Sep 2008, which is close to the spring equinox. The date of the event shown in Fig 4.10 is 2 Mar 2009, which is close to the autumn equinox.

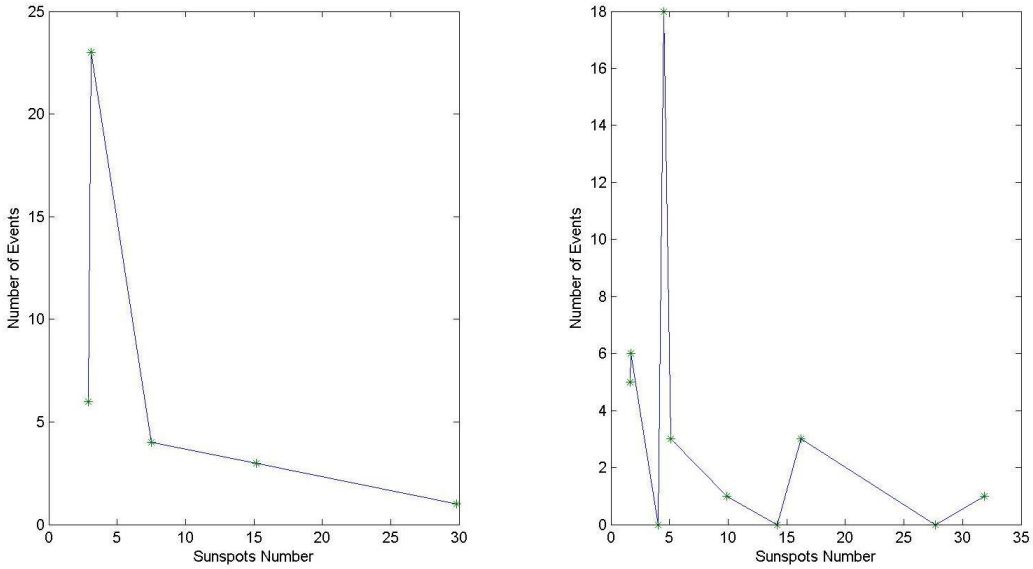

Fig 4.8 The plot illustrates the number of IAR events vs. sunspots number. The left panel illustrates the relation between the sunspots number of each Year and the IAR occurrence of the Year. Each asterisk denotes a Year. The right panel illustrates the number of IAR events against the sunspots number of every half a year. Each asterisk denotes 6 months.

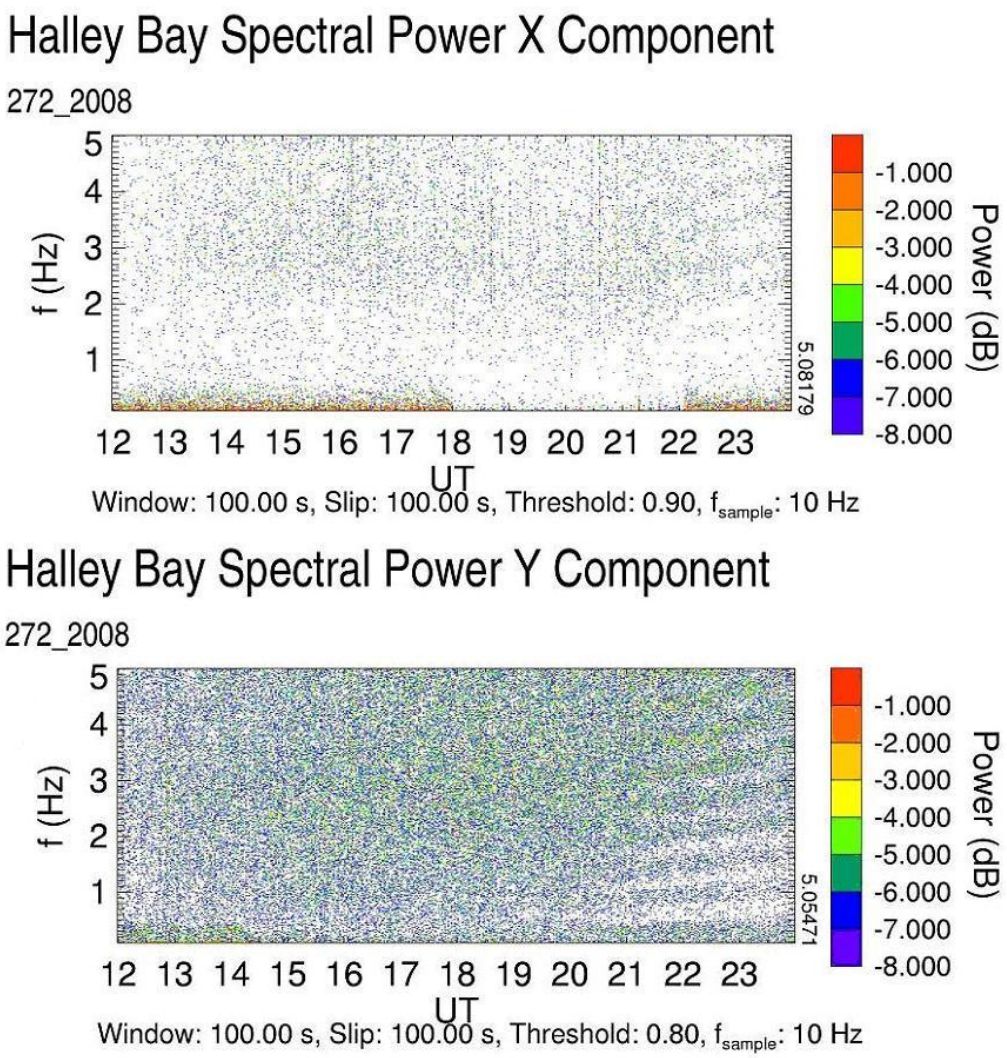

Fig 4.9 The spectrum of 28 Sep 2008. The upper panel illustrates the X component which is N-S component. The lower panel illustrates the Y component which is E-W component.

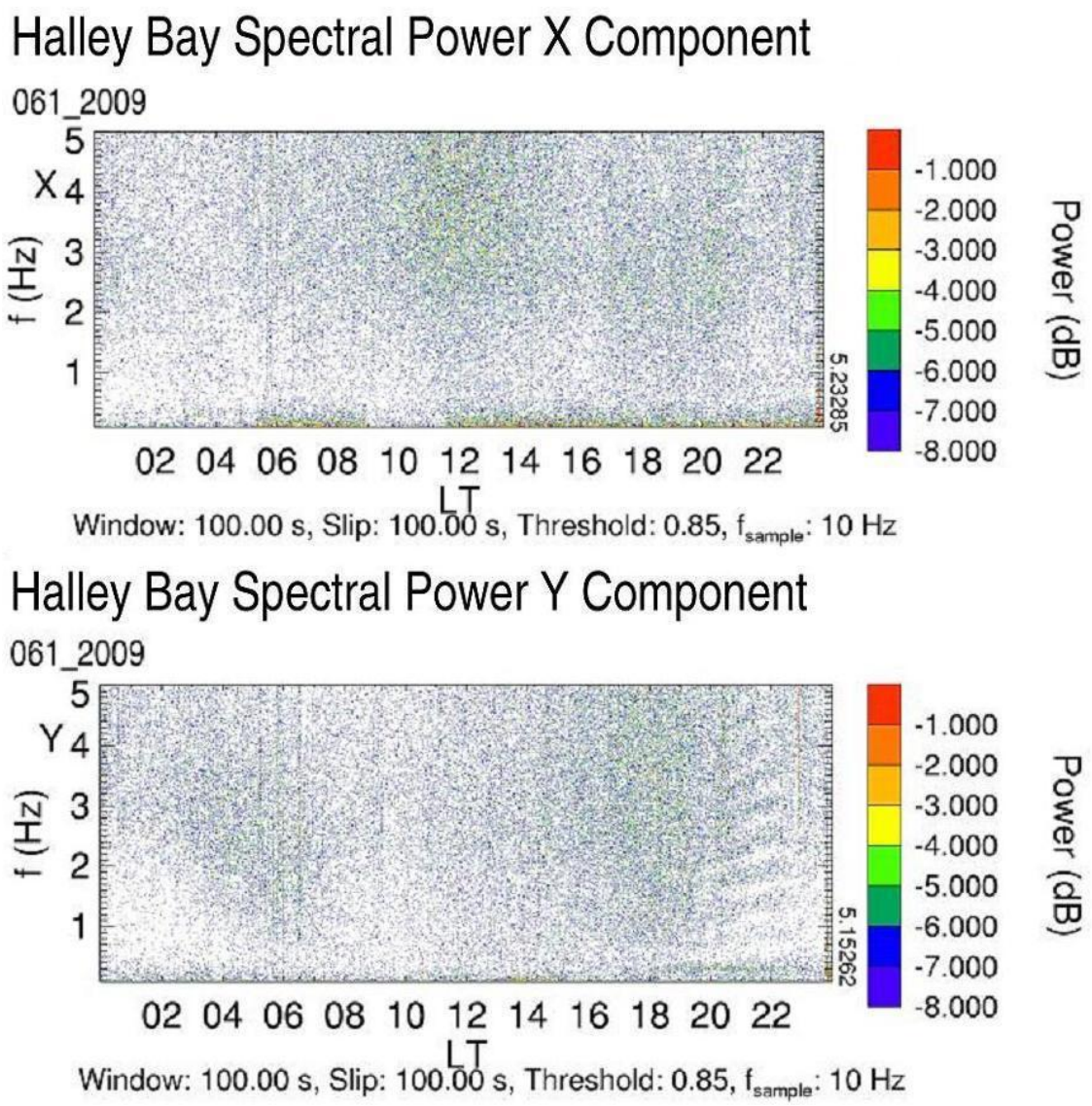

Fig 4.10 The spectrum of 2 Mar 2009. The upper panel illustrates the X component which is N-S component. The lower panel illustrates the Y component which is E-W component.

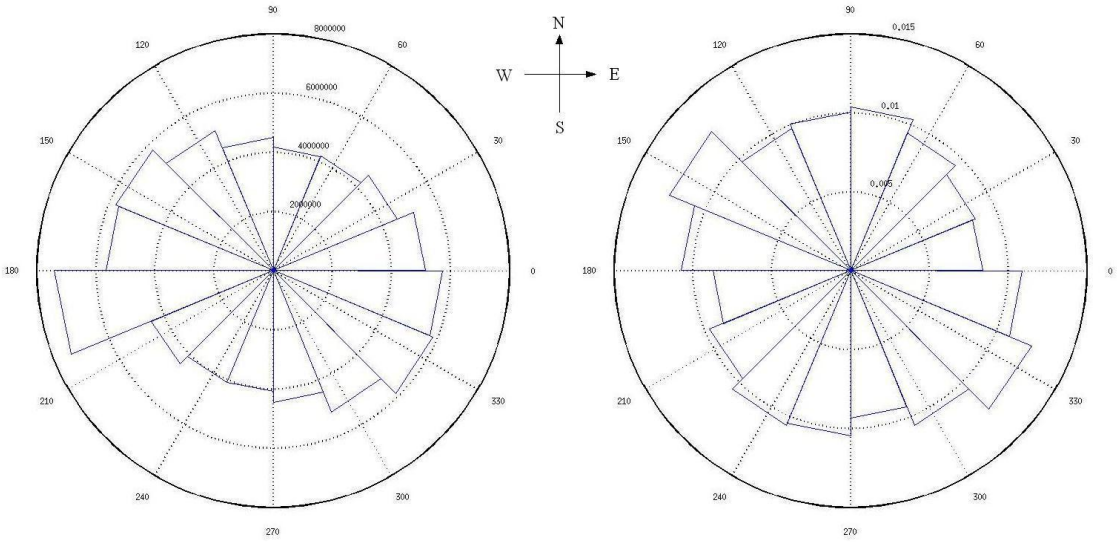

Fig 4.11 The figure illustrates the polar coordinate histogram of the directions of the magnetic field directions detected by the pulsation magnetometer in Halley Bay Station from 2006 to 2009, including both IAR days and days without IARs. The left panel illustrates the total number in each direction. The right panel illustrates the total power of the signals in each direction.

According to some previous studies on IARs, the oscillation source of IARs could be lightening or magnetospheric signals [Shalimov and Bosinger, 2008; Surkov et al, 2006; Mursula et al, 2000, Demekhov, 2007]. However, there could be other oscillation sources. Fig 4.11 illustrates the polar coordinate histogram of the directions of the magnetic field vector detected by the pulsation magnetometer in Halley Bay Station from 2006 to 2009, including both IAR days and days without IARs. The data were worked out by subtracting the mean field intensity from the raw time series pulsation data of each component. Fig 4.11 just shows the horizontal components. The left panel illustrates the total number in each direction. The right panel illustrates the total power of the signals in each direction. It can be seen that during the 4 years, there were more pulsation directions toward west by south and east by south, and less toward north or south. Also, the total power of the pulsations towards east by north and west by north are stronger than the total power of the pulsations towards north or south. Referring to Fig 4.9 and Fig 4.10, it can be seen that the whether the harmonic structures of IARs are clear or not might be dominated by the periodic signals in the ionosphere. In addition, it implies that the source of the IAR oscillations could be the Pedersen current driven by the horizontal electric field in the ionosphere, and the electric field could be the noise signals in the ionosphere. Thus it may not be necessary for IARs to have particular events such as lightening or pearl structure for oscillation sources.

Typically a resonance cavity is formed by two reflective layers at both of the ends, and a main body between the two reflective boundaries. For an IAR, the lower reflective boundary is the Pedersen conductive layer at the altitudes around 100km. The upper reflective layer is the exponential plasma density profile above the F2 peak. The maximum effective altitude of the IAR is about 1400km [Prikner et al., 2007]. Considering that both the Pedersen conductive layer and the exponential plasma density profile above the F2 peak always exist, the structure of the resonance cavity always exists. In other words, there is always a Q factor for the IAR everywhere at high latitudes of both northern and southern hemispheres. The Q factor varies with time. According to previous studies [Belyaev et al., 1990; Polyakov and Rapoport, 1991], the Q factor is mainly controlled by the ratio between the height integrated Pedersen conductivity and the Alfvénic wave conductivity in the E layer. In such a case, the intensity of the resonance signals would be clear if the energy feed into the IAR is

greater than the energy loss. The energy feed into the IAR could be provided by the noise of the electromagnetic field in the ionosphere or the magnetosphere. It could explain why the IAR could be easily excited by lightening or pearl structures. Lightening could lead to the burst of source energy that feed into the IAR. A pearl structure represents the enhancement of the intensity of pulsations in a certain frequency band. Both of the two could feed more energy into the IAR to lead to stronger resonance.

4.5. Summaries

The first statistical study of IARs in Antarctica has been performed. The data was from Halley Bay Station which is operated by the British Antarctic Survey of UK. The data from 2005 to 2009 was surveyed. The period covers five years including a solar minimum which is in 2008. There were 37 IAR events observed based in SRS signals in dynamic spectra in total.

According to the study, more than 95% (35/37) of all the IAR events occurred in one month prior or after equinoxes. There are two gaps for the IAR occurrence in a whole year in 2005 to 2009, which are November to January and May to August, respectively. However, considering the data gaps shown in Table 4.1, there could be IAR occurred in January. Also, the occurrence in February could be a little higher than the rate shown in this chapter, however, it would not change the result of the statistical study of IAR seasonal and monthly occurrence in this chapter significantly. The instrument upgrade was not taken into account in this study. The date coverage rate of the surveyed data of the whole period is 96.28%, which is relatively high. The IAR occurrence after spring equinoxes and prior autumn equinoxes is higher than the other two periods. According to the study by Trakhtengerts et al [2000b], the IAR occurrence is anti-correlated to the solar activity. However, all the previous studies about the IAR occurrences just investigated the IARs in northern hemisphere. In the study of this chapter, it can be seen that the anti-correlation between the solar activity and the IAR occurrence is also satisfied in Antarctica.

Also, based on the statistical study of the directions of magnetic field vector measured by the pulsation magnetometer in Halley Bay Station in this chapter and the field intensity variations of the IAR in chapter 3, it can be seen that the oscillation source of the IAR could be the noise of the electromagnetic field pulsations in the ionosphere. There are always the resonance cavity structures of IARs in the ionosphere, thus there should be a threshold for the noise to excite IARs.

Chapter 5. Numerical Modelling: Model Description and Tests

5.1. Introduction

In Chapter 3 it has been pointed out that the IAR eigenfrequency separations were mainly dependent on the local plasma density profile of the ionosphere. Also, at the end of section 3.6, an example of non-uniform distributed eigenfrequencies was shown in Fig 3.16. In order to investigate the relationship between the eigenfrequency separations and the structure of the resonance cavity in more details, it is necessary to develop a computational model. There have been many models developed based on traditional theories of Alfvén waves and IARs (see Chapter 2). Some of them are based on the first model of IAR which was developed by Trakhtengerts and Feldstein [1981]. The model was further developed by Lysak [1988, 1991] and Belyaev et al [1990].

Basically those models were using exponential plasma density profiles. The density below the F2 peak was set to be uniform and the plasma density above the F2 peak decreases with altitude exponentially. More details can be seen in Chapter 2.

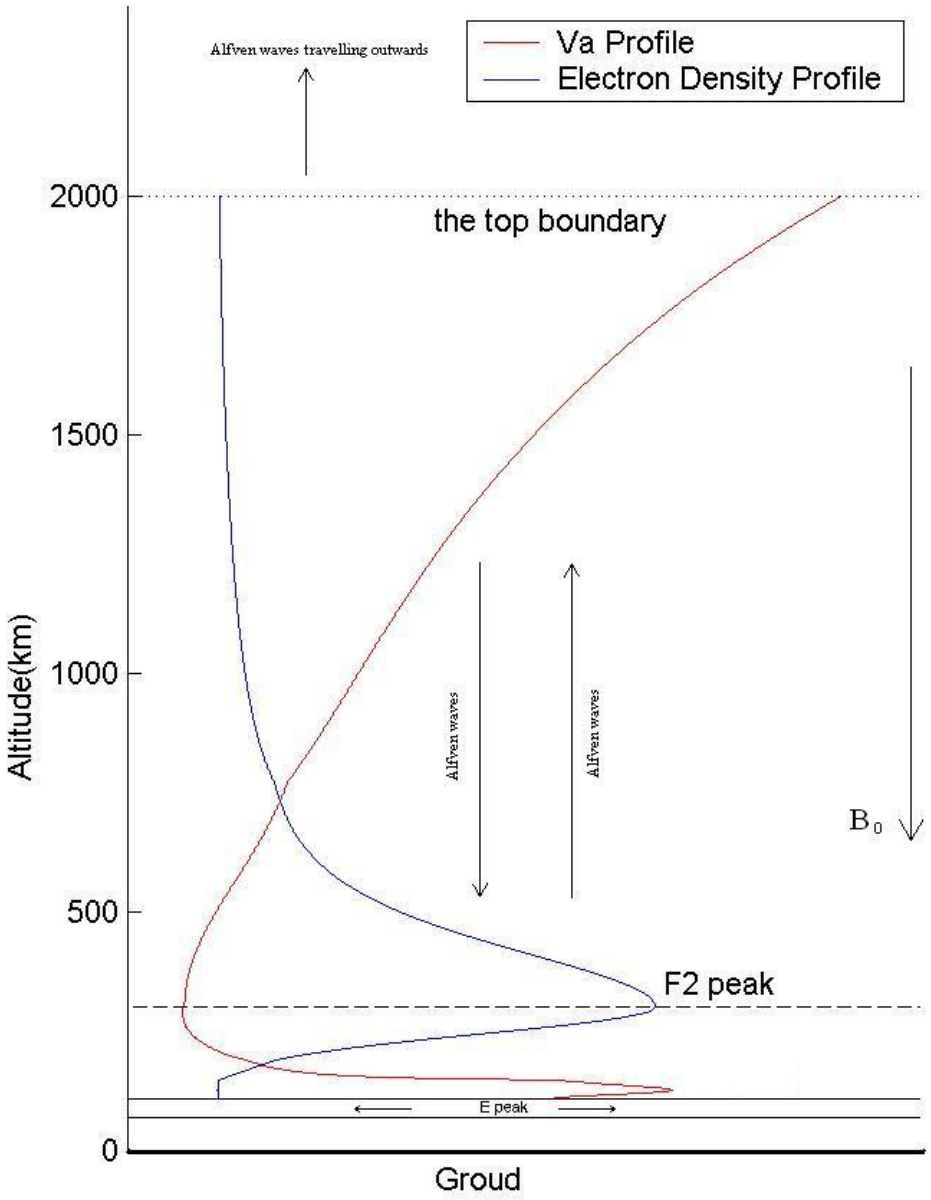

Fig 5.1 The figure illustrates the structure of the IAR model. The blue line is the plasma density profile. The red line is the Alfvén velocity profile.

The model that is going to be introduced in this chapter was also developed based on the Trakhtengerts' first model. But it will be treated numerically. The model will be carefully tested in this chapter, and the results of the model would be compared with some observations.

The programme of the numerical computation of the model was developed in Matlab6.5. Version 6.5 of Matlab was published by The MathWorks in 2002.

5.2. The Structure of the Model

The structure of the model is illustrated in Fig 5.1. The model is quite similar to Trahktengerts' [1981]. The model introduced in this chapter is simpler than Lysak's model [Lysak, 1991] and Belyaev's models [Belyaev et al., 1990] because the Hall term in the E region of the ionosphere was ignored. On the other hand it is able to deal with any type of plasma density profile. That means a real plasma density profile could be utilized for the input of the model. In Belyaev's model and Lysak's model the plasma density profile below the F2 peak was set to be uniform.

The main features of the IAR can be seen in the model shown in Fig 5.1. Those features would be taken into account in the numerical model. The bottom boundary of this model is the E peak of the ionosphere, which is about 100km above the ground. The thickness of the bottom boundary was assumed to be negligible. Also, the bottom boundary is the Pedersen conductive layer of the ionosphere. Practically the thickness of the Pedersen conductive layer is 30km-50km, thus in order to make the model be more realistic, the height integrated Pedersen conductivity was used at the bottom boundary. This makes sense because the wavelengths of Alfvén waves are much greater than the thickness of the effective Pedersen conductive layer in the E region and the lower F region. So, the Hall conductivity was ignored. In this model, the region above the bottom boundary is the main body of the resonance cavity. The plasma density

increases with altitude till it reaches the F2 peak. The blue curve in Fig 5.1 indicates the plasma density profile. The maximum value occurs at the F2 peak. The red line indicates the Alfvén velocity profile in the same range of altitudes. In the region where the plasma density increases monotonically with altitude below the F2 peak. The Alfvén velocity profile increases for a short distance and then decreases. The minimum value of the Alfvén velocity profile is not exactly at the altitude of the F2 peak. These features are caused by the variation of average mass density of ions with altitude in addition to the change in plasma density. The percentage of each species of ions is changing with altitude according to the model of International Reference Ionosphere. Generally the percentages of light ions increase with height while percentages of heavy ions such as O^+ decrease with height. The dashed line indicates the altitude of the F2 peak. The space above the F2 peak is the top of the ionosphere and the bottom of the magnetosphere. The plasma number density decreases exponentially with height in this region while the Alfvén velocity increase exponentially with height. According to the study of Prikner et al [2007], the effective size of an IAR that affect the wave signal received on the ground could be up to 1500km. In order to ensure that the results of this model are more realistic, the altitude of the top boundary was set to be 2000km. In the model introduced in this chapter, it is assumed that the plasma density becomes a constant above this altitude. Thus the field strength of the Alfvén waves penetrate into the magnetosphere from the resonance cavity does not change, just the phase of the field changes. Also, it is assumed that the Alfvén waves travelling above the top boundary will not be able to penetrate the main body of the resonance cavity. That means all the reflective processes take place below the top boundary of the model. When waves travelling upwards in the cavity reach the top boundary, part of them could penetrate the region above the top boundary and never comes back. In such a case the transmitting boundary condition will be utilized at the top. However, the top boundary is just an artificial boundary. There is nothing special at that altitude. The reflective processes occurred at the boundary were physical. That means the reflection of Alfvén waves at the top boundary is still caused by the gradient of the exponential Alfvén velocity profile. This could lead to errors, which will be discussed later in this chapter.

Kinetic effects will not be taken into account in this model. Thus, for this model there is a unique main axis in the model. Waves propagate along the main axis. The main axis is

assumed to be Z axis in the model. The electric field is in X direction and the magnetic field is in Y direction. In other words, the plasma is taken as uniform in the other two directions. Events going to be studied with this model were observed at high latitudes, and considering that the effective altitude of the IAR is less than 2000km, thus the background geomagnetic field was set to be vertical (Z axis). Since those events were observed in northern hemisphere, thus the geomagnetic field was towards the ground. Alfvén waves propagate upwards and downwards along the geomagnetic field. When the Alfvén waves in the resonance cavity reach the lower boundary, which is the maximum E region of the ionosphere, the electric field of the waves drives Pedersen currents horizontally at the lower boundary. The Pedersen currents could be the source to stimulate new Alfvén waves propagating upwards. The new Alfvén waves propagating upwards can be reflected due to the gradient of the Alfvén velocity profile near the upper boundary. A source current is needed to stimulate the Alfvén waves propagating towards the top of the cavity. In this study the source current is a stable horizontal current at the lower boundary. That means for the numerical study the source of the resonance is in the ionosphere. The source current is an independent and oscillating Pedersen current, which is different from the currents driven by the Alfvén waves. Also, the intensity and the phase of the source current cannot be affected by the Alfvén waves. Obviously there could be magnetospheric sources of Alfvénic resonances [Prikner et al, 2004]; however, this situation is not taken into account in this chapter. The model introduced in this chapter just deals with the sources in the E region.

5.3. The mechanisms of the Model

The equations of the model are listed below:

Equations of the main body of the model:

$$\nabla \times \vec{E} = -\frac{\partial \vec{B}}{\partial t} \tag{5.1}$$

$$\nabla \times \vec{B} = \mu_0 \vec{J}_1 \tag{5.2}$$

$$\vec{J} = \vec{J}_S + \vec{J}_W \tag{5.3}$$

$$\vec{E} = -\vec{v}_1 \times \vec{B}_0 \tag{5.4}$$

$$\rho \frac{\partial \vec{v}_1}{\partial t} = \vec{J} \times \vec{B}_0 \tag{5.5}$$

$$\vec{J}_W = \frac{1}{\mu_0} \nabla \times \vec{B}_1 \tag{5.6}$$

Equations for the boundary conditions:

$$Top: \vec{E}(z) = \vec{E}(z) e^{ik_\infty z}, \vec{B}(z) = \vec{B}(z) e^{ik_\infty z} \qquad z > z_{upper} \tag{5.7}$$

$$Bottom: \nabla \times \vec{B} = \mu_0 (\sigma_P \vec{E}_x + \vec{J}_S) \tag{5.8}$$

$$\vec{J}_S = \vec{I}_{ext} \delta(z - z_0) \tag{5.9}$$

where $\vec{E}, \vec{B}, \mu_0, \vec{J}_S, J_W, \vec{v}_1, \rho, V_A$ are electric field, magnetic field, vacuum permeability, source current, wave current, vertical drift velocity of plasma, mass density and Alfvén velocity, respectively. z_{upper} is the altitude of the upper boundary. k^∞ is the wave vector above the top boundary. Subscript 0 denotes the stable part or the background of the variable, 1 denotes the perturbation part of the variable, S denotes variables of the source and subscript W denotes variables of the wave. Equation 5.1 is the Faraday's Law; Equation 5.2 is the Ampere's Law; Equation 5.3 means the total current is consisted of the wave current and the source current; Equation 5.4 is the equation of E cross B drift; Equation 5.5 is the Ampere's Force Law and Equation 5.6 is the Ampere's Law. The above equations are basic MHD equations of the Alfvén wave. The mass of electrons was ignored. The boundary conditions of the model were represented by the three boundary equations. Equation 5.7 is the upper boundary condition. This equation shows that both the electric field strength and the magnetic field strength do not change above the top boundary, just the phase of the field changes. It is a transmission boundary condition. This is the assumption mentioned in the last section. Equation 5.8 and 5.9 are the boundary conditions for the bottom boundary. Equation 5.8 implies that the electric field of the Alfvén wave at the lower boundary drives the Pedersen current. Equation 5.9 implies that the only source current is at the lower boundary, which is an independent Pedersen current.

This is a purely one-dimensional linear model. All the nonlinearities were ignored in this model. The Hall term was also ignored because the aim of the model is calculating the eigenfrequencies of the IAR. The eigenfrequencies mainly depend on the structure of the resonator according to the theories of resonance cavities. That means the compressional modes were not taken into account in this model because the Hall term just allows the coupling to compressional modes. In such a case it makes sense to ignore the Hall term. Also, since the mass of electrons was ignored there will be no dispersion process for Alfvén waves in the model, e.g. the inertial Alfvén waves and the kinetic Alfvén waves are not taken into account, and thus the parallel electric field will not exist in this model. Finally the vertical plasma transportation and all the thermal processes of the plasma were ignored.

Basically the plasma number density and the Alfvén velocity profile for the model input were generated by International Reference Ionospheric Model 2007 (IRI2007). The IRI is an empirical model developed since late 1960s. The model kept being improved since then. The plasma number density data and the percentage of each species of ions could be downloaded from http://ccmc.gsfc.nasa.gov/modelweb/models/iri_vitmo.php. The data of geomagnetic field at Sodankylä is available on the website of Sodankylä Geophysical Observatory. The time resolution of the geomagnetic field data is 1 minute. According to equation 5.10, the Alfvén velocity profile could be worked out based on the plasma density, percentages of ion species, which were given by IRI2007 model, and the geomagnetic field. Thus the numerical study will be based on the Alfvén velocity profile at Sodankylä.

$$V_A = \frac{B}{\sqrt{\mu_0 m_i n_i}} \tag{5.10}$$

where μ_0 is the vacuum permeability, B is the intensity of the geomagnetic field, m_i is the mean mass of ions and n_i is the ion number density.

There are several reasons to choose the IRI2007 model for the input data of Alfvén velocity profile. Firstly the IRI2007 model monitors the general trend of the plasma density profile variation quite well. Plasma density profile at any location over the whole world can be worked out by IRI2007 model. Secondly the vertical scale of IRI2007 model is quite large. It is able to work out the ionospheric parameters at the altitude up to 2000km. According to Prikner et al [2007], the effective vertical scale of the IAR could be up to 1400km. In practice of the study, an even bigger resonance cavity is required in order to reduce numerical errors. However, there are only two normal ways to detect the plasma density above the F2 peak precisely, one is using incoherent scatter radar like EISCAT, and the other one is using a low orbit satellite. There are just a few incoherent scatter radars over the whole world, and seldom of them are close enough to a pulsation magnetometer (less than 200km). Those incoherent scatter radars rarely run in the mode that is able to detect the plasma density profile up to 1500km. On the other hand, the satellite cannot detect a continuous vertical density profile at certain location. Thus using the IRI2007 model is the best way for this model. However, the Alfvén velocity profile generated by IRI2007 model is not precise enough, e.g., the foF2 generated by IRI2007 is different from the detected foF2, which could lead to significant errors of the Alfvén velocity at the F2 peak. In order to solve this problem a correction process was used. Basically the density profile data generated by IRI2007 model was scaled according to the foF2 detected by ionosondes. For example, when the density profile of Sodankylä was generated by IRI2007, the observed foF2 by Sodankylä ionosonde was used as an input parameter, and then the output plasma density profile would be much more precise. The detected values of foF2 in Sodankylä are available at its website (http://www.sgo.fi).

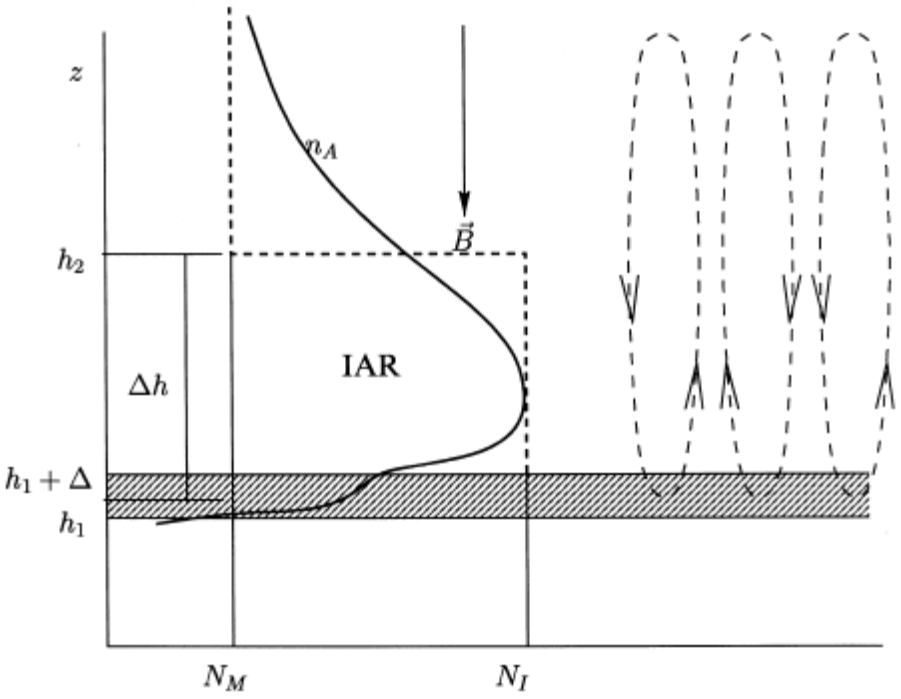

Fig 5.2 The structure of Trakhtengerts' 3-step model [Trakhtengerts & Belyaev, 2000a]. The solid thick line is the real plasma density profile. The dashed line is the density profile utilized in the model. The shadow area is the E region of the ionosphere. The dashed circles with arrows on the right show the Alfvén vortices.

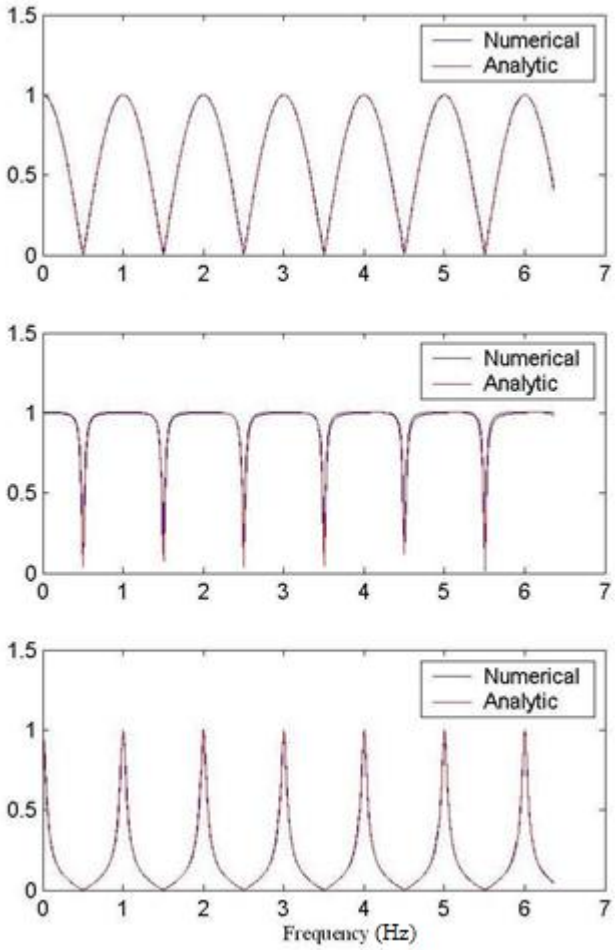

Fig 5.3 The comparison between this numerical model and the 3-step model. From the top to the bottom the panels corresponds to the conditions of Σ_W / Σ_P equals to 1, 0.1 and 10, respectively. 'Analytic' illustrates the results of the 3-step model; numerical illustrates the results of the present numerical model. The two lines in each panel are almost superposed, which means this numerical model agreed with the 3-step model quite well.

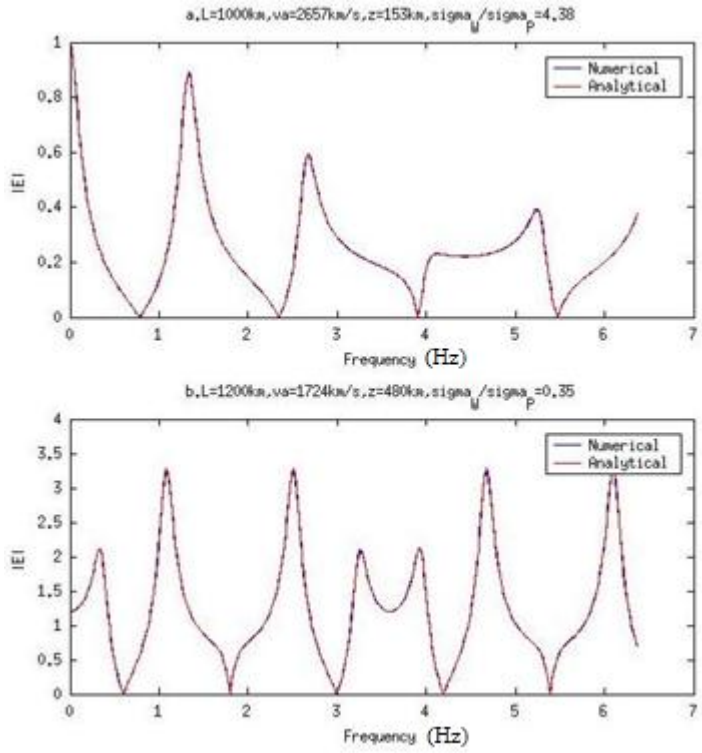

Fig 5.4 The comparison on the electric field of random altitudes. The two lines are superposed in each panel. The altitudes are selected randomly.

5.4. Algorithms and Error Estimation

In order to solve the model numerically, equation 5.1 to 5.6 need to be Fourier transformed into frequency domain. Considering it is a one-dimensional model, equations 5.11 to 5.14 correspond to equation 5.1 to 5.6 respectively.

$$\frac{\partial E_x}{\partial z} = i\omega B_{1y} \tag{5.11}$$

$$\mu_0 J_1 = \frac{\partial B_{0z}}{\partial z} \tag{5.12}$$

$$\mu_0 J_{1x} = -i\omega\rho v_{1y} / B_{0z} \tag{5.13}$$

$$E_x = -v_{1y} B_{0z} \tag{5.14}$$

where ω is the angular frequency, i is the imaginary unit, B_{0z} is the background geomagnetic field, which was set to be a constant in the study. The subscript x denotes the component in x direction while subscript y denotes the component in y direction. Both of the two directions are in the horizontal plane.

Direction of each variable is denoted by the subscript. Here, x and y are horizontal directions and z is the vertical direction, which is also the direction of the wave propagation. Equations 5.11 to 5.14 can be simplified into two equations, which are shown as equation 5.15 and 5.16.

$$\frac{\partial B_y}{\partial z} = \frac{i\omega}{V_A^2(z)} E_x \tag{5.15}$$

$$\frac{\partial E_x}{\partial z} = i\omega B_y \tag{5.16}$$

where $V_A(z)$ is the Alfvén velocity, z is the altitude.

There are only two variables left in equations 5.15 and 5.16, which are the electric field and the horizontal magnetic field, respectively. The electric field and the horizontal magnetic field are perpendicular to each other. They are the two components of Alfvén waves. The two equations can be further simplified to a single equation. By inserting equation 5.16 into equation 5.15, equation 5.17 was obtained.

$$\frac{\partial^2 E_x}{\partial z^2} + k_A^2(z) E_x = 0 \qquad (5.17)$$

where $k_A(z) = \omega / V_A(z)$, which is the Alfvén wave vector. ω is angular frequency. Equation 5.17 is a typical wave equation in frequency domain. This equation will be used for numerical computation to solve the model.

In order to solve the model numerically, the differential equation 5.17 has to be transformed into difference form. The difference algorithm [Mathews, 1987] is shown below:

$$\left.\frac{\partial f}{\partial z}\right|_{z_0} \approx \frac{f|_{z_1} - f|_{z_{-1}}}{2\Delta z} + O(\Delta z^2) \qquad (5.18)$$

$$\left.\frac{\partial^2 f}{\partial z^2}\right|_{z_0} \approx \frac{f|_{z_1} - 2f|_{z_0} + f|_{z_{-1}}}{\Delta z^2} + O(\Delta z^2) \qquad (5.19)$$

where the Δz is the grid size, and $O(\Delta z^2)$ denotes the second order of local truncation error. The difference equation 5.20, which corresponds to the partial differential equation 5.17, was obtained.

$$E_x(n-1) + (\Delta z^2 k_A^2 - 2) E_x(n) + E_x(n+1) = 0 \qquad (5.20)$$

where $E_x(n)$ is the electric field at n-th grid point. In order to solve equation 5.20, Gaussian elimination or other similar methods are needed. However, in order to solve the system of linear equations, the top and the bottom boundary equations in difference form are required. It should be noticed that $E_x(1)$ is not the total electric field at the bottom boundary. It is just the wave field. The total electric field at bottom boundary

includes the wave field and the field which drives the source current. The signal detected on the ground depends on the total field of the bottom boundary.

For the upper boundary, the difference equation is the difference approximation of equation 5.7. Thus,

$$E_x(n+1) = E_x(n)e^{ik_z z} \tag{5.21}$$

where $E_x(n+1)$ is the electric field at the ghost grid point above the top boundary, $E_x(n)$ is the electric field at the top boundary, k_z is the wave vector at the top boundary, z is the relative altitude referred to the altitude of the bottom boundary, e.g., if the bottom boundary was supposed to be at 0km, for the grid point that is 1km above the bottom boundary, the altitude z is 1km. Equation 5.21 means the intensity of the electric field above the top boundary equals to the intensity at the top boundary. That is caused by the assumption that the Alfvén velocity is a constant at and above the top boundary.

For the lower boundary, equations 5.22 and 5.23 are the difference approximation of the differential form of the boundary condition. The equations were derived from equation 5.3, 5.8, 5.9, 5.10 and the transmission boundary condition for the ghost grid.

$$\frac{V_{A2} - V_{A1}}{2\Delta z} = R_{bot} \tag{5.22}$$

$$E_x(-1) = E_x(0)e^{-ik_0\Delta z} \tag{5.23}$$

where $E_x(0)$ is the electric field at the ghost grid point below the bottom boundary and $E_x(-1)$ is the electric field below the ghost grid. The ghost grid is an unreal grid below the bottom boundary [Matsumoto & Omura, 1993]. By utilizing the ghost grid, the gradient at the bottom boundary could be worked out.

It should be noticed that in order to solve equation 5.20, the wave vector below the bottom boundary is needed. However, the bottom boundary is a discontinuous boundary

layer. The wave vector below the bottom boundary is 0. In order to solve the problem, an artificial Alfvén velocity was set below the bottom boundary to generate the Alfvén velocity gradient at the bottom boundary. In the computation, the gradient of the Alfvén velocity at the bottom boundary reflects the Alfvén wave instead of the Pedersen conductivity. Referring to Trakhtengerts' 3-step model [2000a] and Hirose's book [Hirose & Lonngren, 1985], the Alfvénic wave conductivity equals to the height integrated Pedersen conductivity at the bottom boundary. The 3-step model will be introduced in more details and compared with this numerical model in section 5.5. According to equation 5.24 and 5.25, the artificial Alfvén velocity below the bottom boundary was obtained.

$$R_i = \frac{1-\Sigma_P/\Sigma_W}{1+\Sigma_P/\Sigma_W} \tag{5.24}$$

$$\Sigma_W = \frac{1}{\mu_0 V_A} \tag{5.25}$$

where R_i is the reflective coefficient at the bottom boundary, Σ_P is the height integrated Pedersen conductivity and Σ_W is the Alfvénic wave conductivity at the bottom boundary.

In order to estimate the error of the numerical solution of the model, the errors would be sorted by their sources and discussed separately. Basically there are two types of errors.

The first type is the numerical error. Generally the numerical errors are truncation errors. Local truncation errors are generated by difference approximations. In this numerical algorithm the local truncation error is the second order. The local truncation error of the numerical computation could propagate and accumulate due to the Gaussian elimination process. The error caused by the Gaussian elimination in this numerical model was estimated. The details can be seen in section A3 of APPENDIX.

In addition, numerical errors can be produced at the two boundaries. Sometimes the vertical gradients of parameters of ionospheric plasma are quite big, particularly near the bottom boundary. The spatial scales of the ionospheric layers are much smaller than structures at higher altitudes. For example, if the length of a single grid is chosen to be 20km, the plasma density might not change too much from a grid point to its neighbour point above 1000km, however, the plasma density might be totally different at the altitude of 20km below the bottom boundary. In this numerical study, the grid size was normally selected to be 1km. In other words, there could be strong discontinuity at or near the bottom boundary. That could lead to significant errors at the bottom boundary because the difference forms of equations need to assume that the discontinuities are not quite strong. Similarly, the plasma density near the top boundary of the resonance cavity was assumed to be a constant, thus the field strength does not change when the wave propagates across the top boundary. However, that is not always true. The results of different grid sizes will be tested in section 5.5, which will show that the errors exist, but they are negligible in this study. By viewing the Alfvén velocity profile generated by IRI2007 model (e.g. the profile shown in Fig 5.1), it is possible to see that the Alfvén velocity still keeps increasing at the altitude of 2000km. That does not completely satisfy the top boundary condition of the model, thus it might lead to significant errors. To reduce the numerical errors generated at the boundaries, the grid length of the simulation box was chosen to be 1km, which is really small compare to vertical structures of the ionosphere. The top boundary was fixed to be much higher than the effective size of the resonance cavity. However, it led to a low efficiency of the code.

On the other hand, there are some simplifications and assumptions in this model, and some physical mechanisms were ignored. Some of those assumptions and ignorance could lead to errors. First, all the nonlinear processes were ignored in the model. Some nonlinear processes could significantly change the plasma density profile of the ionosphere. This model cannot deal with those nonlinear cases. An example will be introduced in Chapter 6. The model was solved in the frequency domain. That implies that the ionospheric condition should be stable or quasi-stable during a certain period, then the model just works in the period. For example, in the IAR event observed at

Kilpisjärvi station in Chapter 3, the ionospheric condition changed significantly, which led to intensively changing eigenfrequencies of the IAR. This numerical model cannot simulate cases like that. Secondly, the errors generated by IRI2007 model might be significant. IRI2007 is an empirical model developed based on observations. It just shows the general trend of density profiles according to modern theories and observations of the ionosphere. However, theories and models are still not good enough to predict or interpret all the processes in the ionosphere. There are only a few incoherent scatter radar systems over the whole world. Thus the ionospheric data above the maximum F2 layer is not sufficient to support the development of IRI models. In such a situation, sometimes the errors of IRI models are not ignorable. In addition, it leads to the error of the reflective boundaries, particularly the bottom boundary. For example, the altitude of the E peak was fixed to be 110km at Sodankylä in the plasma density profile generated by IRI2007, but that is not always true. In order to obtain more accurate density profiles, the ionosonde observation data was used to correct the density profiles generated by IRI2007 model. Another significant error is caused by the ignorance of the Hall term. The ignorance of the Hall term might lead to errors on eigenfrequencies [Pokhotelov, O., D. Pokhotelov, et al, 2000], and sometimes it could lead to significant errors on the ratio of intensity of eigenfrequencies.

5.5. Model Tests

It is very important to test a new numerical model carefully; otherwise the results of the model are not believable. In order to find the most efficient initial parameters and estimate the numerical errors and the physics of the results, it is necessary to test the errors of the model.

There are four steps to test the model. The first step is to compare the results of the model with other models and theories; then of the random source current will be initialized to prove that the results are physical; after that the results of different sizes of spatial grids and different frequency steps would be compared; finally the results will be compared with some observations.

For the first step, the results of the numerical model were compared with Trakhtengerts' 3-step simple analytic model [Trakhtengerts, 2001a]. In the 3-step model the plasma density was supposed to be uniform in the ionosphere and magnetosphere, respectively. The interface between the ionosphere and the magnetosphere was assumed to be discontinuous for the density profile. The structure of the 3-step model can be seen in Fig 5.2. In the figure, h_1 is the height of the bottom of the E region; Δ is the thickness of the E region; Δh is the effective size of the resonance cavity; h_2 is the effective height of the resonance cavity; N_I and N_M are the effective plasma density of the ionosphere and the magnetosphere, respectively. By assuming that the Hall conductivity equals to 0, and the plasma density profile in the numerical model is uniform, the numerical model becomes definitely same to the 3-step model. The wave equation and the solution of the 3-step model can be seen in equation 5.26 and 5.27, respectively.

$$\frac{d^2\vec{E}}{dz^2} + k_{A0}^2\vec{E} = \frac{4\pi i\Omega}{c^2}\vec{j}_{ext}(k_\perp, \Omega, z) \tag{5.26}$$

$$E(\Omega, \vec{k}_\perp, z) = \frac{\vec{k}_\perp 2\pi I_{ext}}{k_\perp n_{A0} c}\{\frac{1+R_e\exp[2ik_{A0}\Delta h]}{1-R_iR_e\exp[2ik_{A0}\Delta h]} \times (R_i[ik_{A0}(z+z_i)] \tag{5.27}$$

$$+\exp[ik_{A0}(z_i - z) - 2ik_{A0}h_1])\} + \begin{vmatrix} 0, & z \le z_i \\ 2i\sin k_{A0}(z-z_i), & z \ge z_i \end{vmatrix}$$

where $\vec{E}$ is the vector of the electric field, k_{A0} is the Alfvénic wave vector in the ionosphere, $\vec{k}_\perp$ is the perpendicular wave vector, z is the altitude, I_{ext} is the source current density, n_{A0} is the Alfvénic wave refractive index in the ionosphere, c is the speed of light, R_e is the reflection coefficient of the magnetosphere, which is quite close to 1, R_i is the reflective coefficient at the bottom boundary, Ω is the angular frequency, z_i is the altitude of the E region and $\vec{j}_{ext} = \vec{I}_{ext}\delta(z - z_i)$ means the source current located just located at the E region. It should be noticed that the equations of 3-step models are in c.g.s. unit system and the present numerical model is in SI unit system. However, the ratio between the two models is a constant.

Fig 5.3 shows that the results of this numerical model agree with the 3-step model quite well. 'Analytic' denotes the results of the 3-step model, and the 'numerical' denotes the results of this numerical model. It can be seen that the two lines in each panel superposed, which means that the two models agrees quite well.

Additionally, Fig 5.4 illustrates the agreement of the two models. The altitudes of the two panels of the two models are randomly selected. The results are agreed. The results were measured at the altitude of 153km and 480km above the E peak in panel a and b, respectively. In each panel there are two lines. The two lines in each panel are superposed quite well, thus it seems there is only one line. Also, the size of the cavities and the Alfvén velocities are randomly selected. It should be noticed that the ratio between the Alfvénic wave conductivity and the Pedersen conductivity are different in the two panels. The two values are also selected randomly. However, this ratio is a very significant parameter for the boundary condition which could lead to different eigenfrequencies for the resonance cavities of the same sizes when their wave velocities are same [Belyaev et al, 1990; Hirose & Lonngren, 1985]. It will be investigated in more details in Chapter 6. However, in this chapter, all the tests for the numerical model will take place in different boundary conditions, i.e., the ratio is less than or equal or greater than 1.

In order to test that whether the numerical results of the model were physical, a source current of pure noise was utilized. If the results are numerical, not physical, the total respond at the bottom boundary would not show any harmonic features due to the random noise of the source current. The results were shown in Fig 5.5. The Alfvén velocity profile, which is the profile at Sodankylä on 4 Oct 1998, utilized for this figure is the profile calculated from the density profile generated by IRI2007. In panels a1 to a3, $\Sigma_W / \Sigma_P = 0.1$; in panels b1 to b3, $\Sigma_W / \Sigma_P = 1$; in panels c1 to c3, $\Sigma_W / \Sigma_P = 10$. Panels a1, b1 and c1 illustrate the source current; panels a2, b2 and c2 illustrate the total current at the bottom boundaries; panels a3, b3 and c3 illustrate the ratio between the total current and the source current. In the figure it can be seen that the total responds at

the bottom boundaries are noise when the source currents are random noises, regardless of the value of Σ_W / Σ_P. However, the harmonic structures are quite clear in the panels a3, b3 and c3. Those harmonic structures indicate that the resonance occurred in the cavities. The cavities worked as filters. Components of certain frequencies, which are eigenfrequencies, were more intensive than other components. Also, those imply that there are harmonic structures in panel a2, b2 and c2; however, they hide in the noise. Referring to the test shown in Fig 5.3 and Fig 5.4, the numerical results are physical. The electric field intensities shown in panel a3, b3 and c3 are different at higher band. Those differences were caused by the different wave phases at the bottom boundary. Both the field that drives the source current and the wave field at the bottom make contribution to the phase of the total field at the bottom boundary. Different bottom boundary conditions lead to the differences of the phase of the total field. The wave phase at the bottom boundary strongly affects the waves travelling and trapped in the cavity. As the results, the wave intensity is the function of the phase at bottom boundary.

As a standard and typical step to test a numerical model, the size of the spatial grids should be changed and compared with each other. The length of timesteps should also be changed and compared. In this model there is no time advance process because the model was solved in frequency domain. Thus the model was tested with different frequency steps. The code calculates the intensity of electric field as well as the oscillating current at the bottom boundary from low frequency to high frequency in a certain band. Thus there is a resolution of the frequency. This resolution is the frequency step. The resolution should be predetermined. The value of the resolution impacts the precision of the results. The results of the test can be seen in Fig 5.6 and Fig 5.7. The Alfvén velocity profile of 18UT 4 Oct 1998 at Sodankylä generated by IRI2007 was utilized to do the two tests.

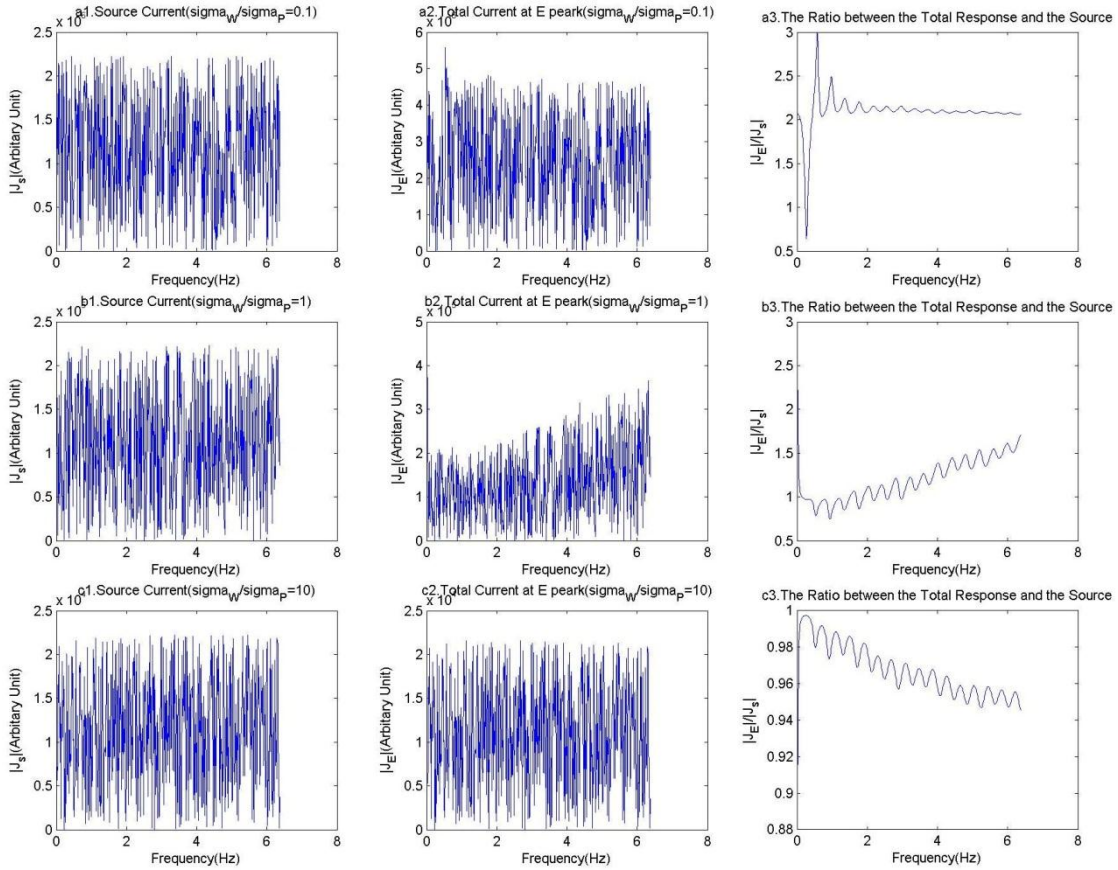

Fig 5.5 The plot illustrates the results of random source current. In panels a1 to a3, $\Sigma_W / \Sigma_P = 0.1$; in panels b1 to b3, $\Sigma_W / \Sigma_P = 1$; in panels c1 to c3, $\Sigma_W / \Sigma_P = 10$. Panels a1, b1 and c1 illustrate the source current; panels a2, b2 and c2 illustrate the total current at the bottom boundaries; panels a3, b3 and c3 illustrate the ratio between the total current and the source current.

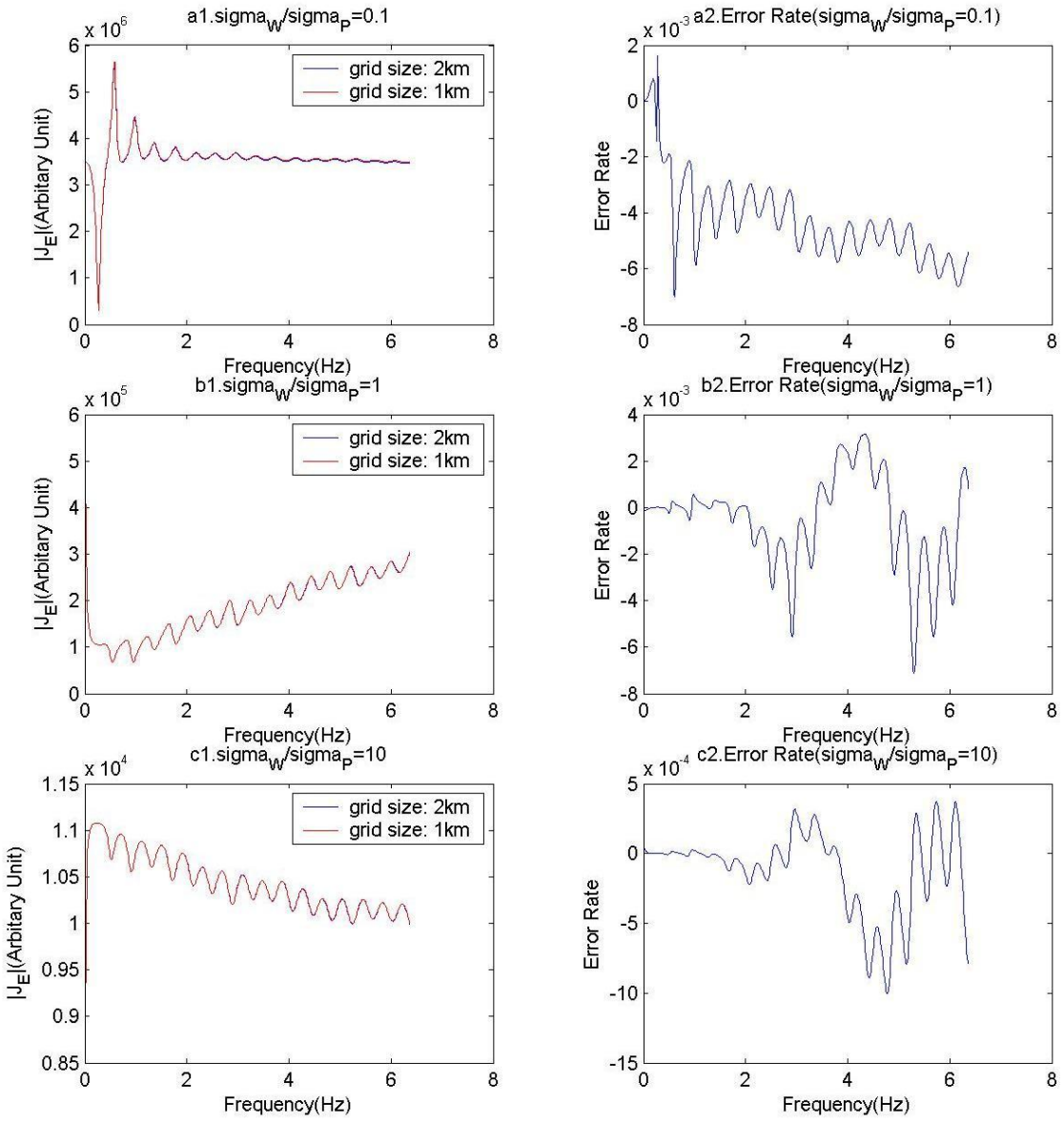

Fig 5.6 The figure illustrates the numerical results of different grid sizes. In panel a1 and a2 $\Sigma_W / \Sigma_P = 0.1$. In panel b1 and b2 $\Sigma_W / \Sigma_P = 1$. In panel c1 and c2 $\Sigma_W / \Sigma_P = 10$. The left panels illustrate the total current at the bottom boundary when the grid sizes are 1km and 2km, respectively. The two lines in each panel are almost superposed. The right panels illustrate the relative error rates. It can be seen that the maximum relative error rate is less than 0.4%.

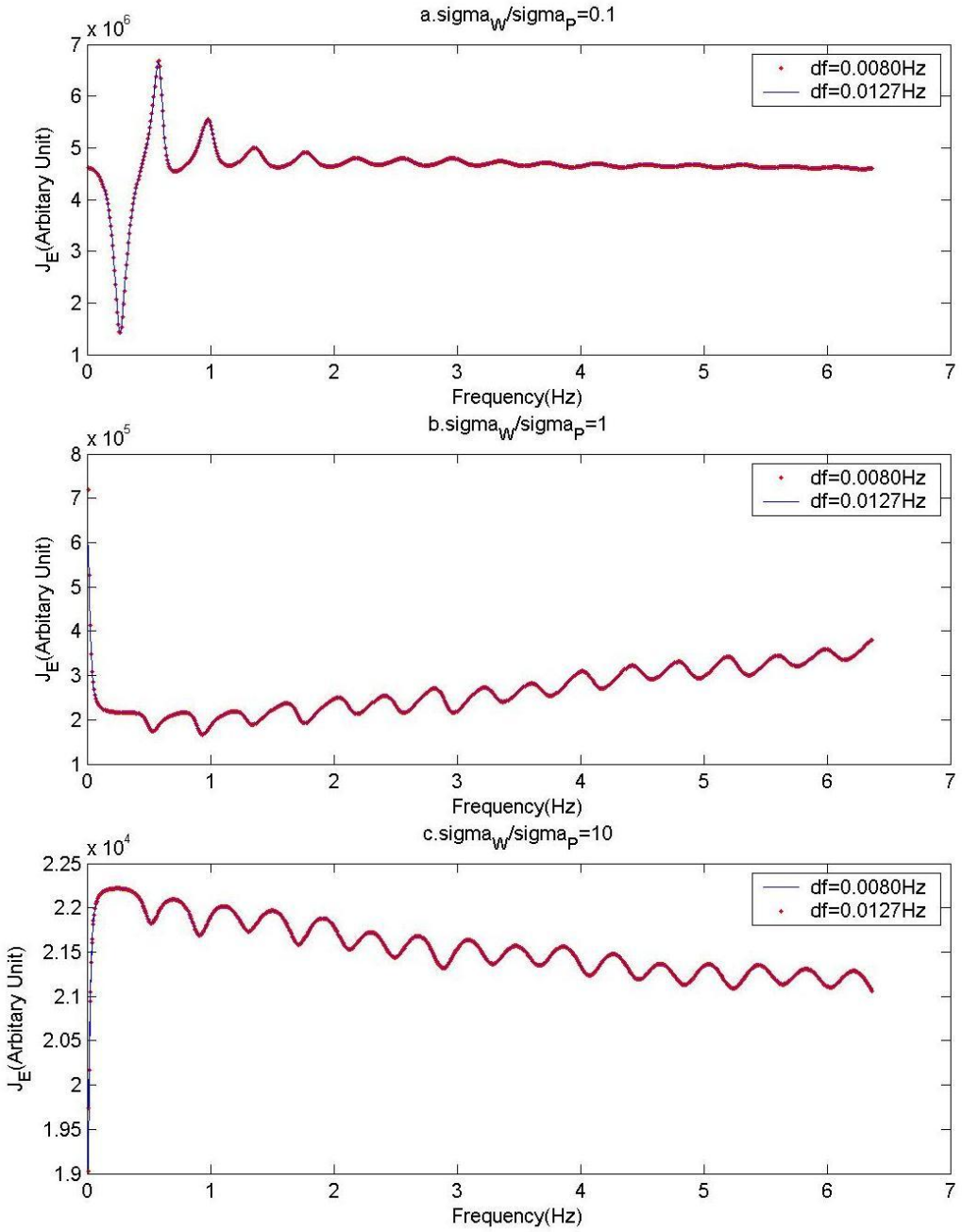

Fig 5.7 The figure illustrates the numerical results of different frequency steps. In panel a $\Sigma_W / \Sigma_P = 0.1$. In panel b $\Sigma_W / \Sigma_P = 1$. In panel c $\Sigma_W / \Sigma_P = 10$. The 'df' is the frequency step. In each panel the two lines superposed. That indicates that the numerical results are completely same when the frequency steps are different (other conditions are same).

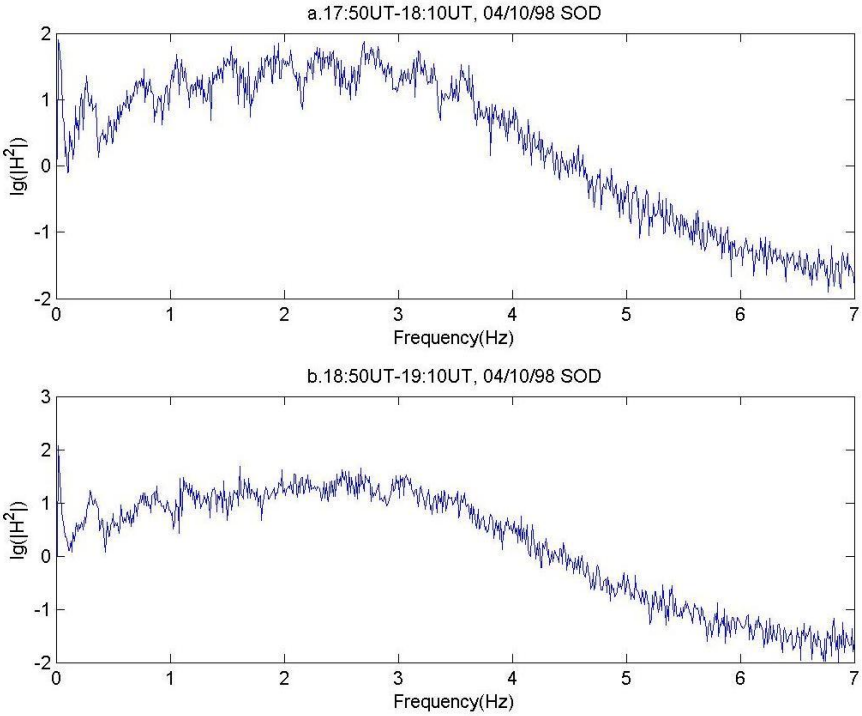

Fig 5.8 The upper panel shows the period in which the harmonic features are clear. The lower panel illustrates the period in which the harmonic features are less clear. Those imply that the eigenfrequencies during the first interval are much more stable than in the second interval.

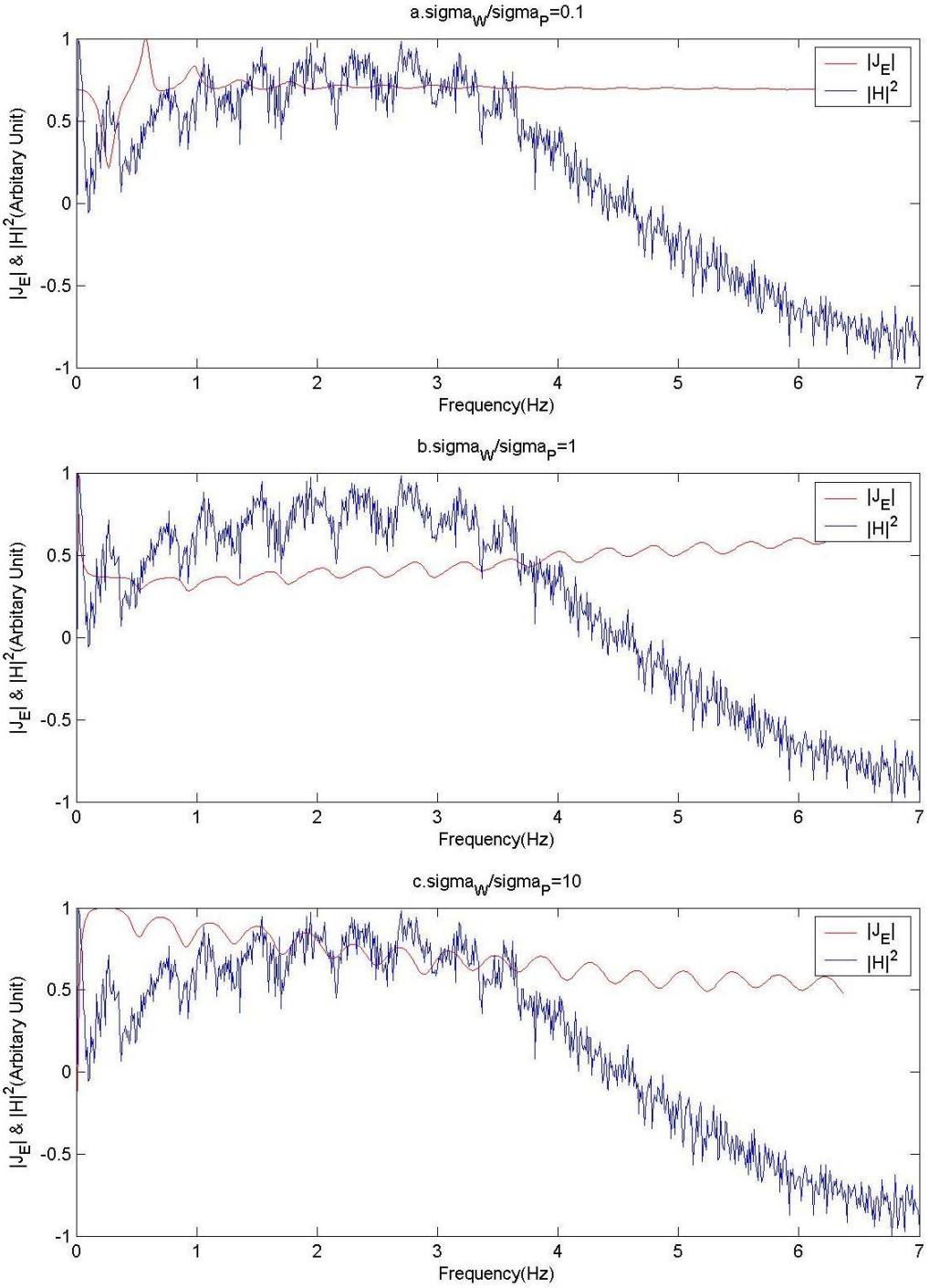

Fig 5.9 The figure illustrates the comparison between the numerical model and the observed dynamic spectrum. The Alfvén velocity profile utilized for the comparison was generated by IRI2007. It is the profile of 4 Oct 1998 at Sodankylä.

Fig 5.6 illustrates the comparisons of the current at the bottom of the resonance cavity as well as the relative error rates which were shown on the right panels. The grid sizes were set to be 1km and 2km, respectively. In panel a1 and a2 $\Sigma_W / \Sigma_P = 0.1$. In panel b1 and b2 $\Sigma_W / \Sigma_P = 1$. In panel c1 and c2 $\Sigma_W / \Sigma_P = 10$. The left panels illustrate the total current at the bottom boundary when the grid sizes are 1km and 2km, respectively. The two lines in each panel are almost superposed. The right panels illustrate the relative error rates. It can be seen that the maximum relative error rate is less than 0.4%. Thus the relative error rates of different grid sizes are quite small. However, in order to obtain high accuracy of the numerical results, the gird size was set to be 1km, which is the highest spatial resolution that can be given by IRI2007. In practice, it takes no more than 15 minutes to complete a single running when the total grid number is 1800 and the total frequency bandwidth is 7Hz.

Fig 5.7 illustrates the comparison between different frequency steps. The two frequency steps were 0.0127Hz and 0.0080Hz, respectively. Σ_W / Σ_P in pane a, b and c are 0.1, 1 and 10, respectively. It can be seen that the dotted line and the solid line in each panel are almost superposed. That indicates the frequency step will not affect the accuracy of the numerical results significantly. In practice the frequency steps was selected to be 0.0127Hz in order to enhance the efficiency of the programme.

Finally, the computation results were compared with observations. Normally IARs appear to be Spectrum Resonance Structure (SRS) on the spectrum of pulsation magnetic field data obtained by pulsation magnetometers. Also, the strength of the magnetic field pulsation observed on the ground is proportional to the Pedersen current in the E region of the ionosphere [Trakhtengerts, 2001a]. Thus the troughs and peaks of the Pedersen current in the computation results will be compared with the spectrum data obtained by pulsation magnetometers. There was an IAR event observed in Sodankylä on 4 Oct 1998 (see Chapter 3). The computation results will be compared with the observed spectrum data of the event. According to the study in Chapter 3, the eigenfrequency of the IAR could fluctuate in a very short period. The eigenfrequency

fluctuations were caused by plasma density variations in the ionosphere. However, the Alfvén velocity profiles used in this model were generated by IRI2007, which is an empirical model. Thus the model cannot deal with the events under strong and frequent plasma density perturbations. In order to ensure that the eigenfrequencies of the IAR were quasi-stable during a certain period, the 20 minutes average spectra of the periods were utilized to roughly measure the variation of the eigenfrequencies of the IARs. Fig 5.8 shows an example of how to measure the eigenfrequencies' variation based on the average spectrum. Panel a illustrates the average spectrum of 17:50UT to 18:10UT on 4 Oct 1998 and panel b illustrates the average spectrum of 18:50UT to 19:10UT of the same day. Clear harmonic features can be seen in panel a; however, it is difficult to see clear peaks and troughs in panel b. That indicates the eigenfrequencies were quasi-stable during the interval shown in panel a. The eigenfrequencies were fluctuating frequently or intensively during the interval shown in panel b. In other words, the Alfvén velocity profile of the period of panel b was changing frequently or intensively, which cannot be well simulated by IRI2007. Thus the spectrum shown in panel a is utilized to compare with computation results.

Based on the spectrum slice shown in panel a of Fig 5.8, the comparison between the numerical results and observed data carried on. Fig 5.9 illustrates the comparison between computations and observations. The values of Σ_W / Σ_P of panel a, b and c are 0.1, 1 and 10, respectively. Both the numerical results and dynamic spectrum slices were normalized according to equation 5.28 and 5.29 in order to compare with each other. However, the peaks and troughs of $\Sigma_W / \Sigma_P = 10$ are not quite clear, thus the numerical results in panels was processed according to equation 5.30.

$$J_E = J_{E0} / \max(J_{E0}) \tag{5.28}$$

$$|H|^2 = |H_0|^2 / \max(|H_0|^2) \tag{5.29}$$

$$J_{E1} = J_E * 10 - 9 \tag{5.30}$$

where J_{E0} is the total current at the bottom boundary of the numerical results, J_E is the normalized total current at the bottom boundary, $|H_0|^2$ is the power of the observed

signals, $|H|^2$ is the normalized power, J_{E1} is the current of the numerical results shown in panel c. Equation 5.30 means that the differences between the peaks and troughs are amplified by ten times. It makes the harmonic structure clearer.

The initial purpose of this model is to investigate the relationship between the plasma density profile and the eigenfrequency shifts observed on the ground (see Chapter 7), thus the positions of the troughs and the peaks of the two lines in each panel should be compared. It is clear that the peaks and troughs match quite well in panel b and panel c. The difference is led by the different boundary conditions, which will be investigated in more detail in Chapter 6. However, they do not match in panel a. Considering that the time of the profile utilized in this test is 18UT, and the time difference between the local time of Sodankylä and universal time is 2 hours, the local time of the profile is 20LT. The value of Σ_W / Σ_P varies from 0.1 to 10 in a single day. In such a case Σ_W / Σ_P is between 1 and 10 [Belyaev et al, 1990]. Thus the comparison shown in panel b or c is more realistic, and the troughs and peaks match quite well. So this numerical model could simulate the eigenfrequencies of IARs quite well based on known plasma density profiles. The further aim of this model is to roughly estimate the plasma density perturbations above the F2 peak based on the IAR eigenfrequencies detected by pulsation magnetometers on the ground. This is parts of the future work of this model.

5.6. Evaluation of the Model and Potential Development

Generally the model was developed to simulate the eigenfrequencies of the IAR. However, it is necessary to further consider the advantages and limitations of the model.

The most important advantages of this numerical model are that it is easy to solve the model in a high efficiency and it could be solved with any Alfvén velocity profile. Basically the model works well in calculating the eigenfrequencies of the IAR.

Trakhtengerts' 3-step analytic model cannot deal with non-uniform profiles. Trakhtengerts', Lysak's and Belyaev's models [Trakhtengerts and Feldstein, 1981; Lysak et al, 1988, 1991; Belyaev et al, 1990] considered the Hall term, which is not necessary in the study of this thesis because the Hall term does not make significant contribution to the IAR eigenfrequencies. The efficiency of the programme could be reduced by the additional Hall term.

For the limitation, the errors of the model have been discussed in section 5.4. The Alfvén velocity profile is a very significant limit of the model. The profiles utilized in the computations were generated by IRI2007. However, it is an empirical model. That means the ionospheric condition should be 'normal', otherwise the Alfvén velocity profiles generated by IRI2007 could be inappropriate.

Considering the model could be solved efficiently, it is possible to further develop the model into a time-advance model. For each timestep, the model is solved in frequency domain. And then the variables should be transformed back to the time domain for the process of time advance. A similar method has been used by Shukla & Eliasson [2003] and Eliasson [2003] to solve Vlasov equations. This is a one-dimensional model. Thus it cannot deal with horizontal coupling processes. And the Hall term was ignored in the model, thus the results of the model would not agree with observations well when compressional modes are significant. Finally, the ignorance of the electron mass might lead to some significant errors in calculating the electric field and the magnetic field [Stasiewicz, 1999; Lysak, 1996]. And it also leads to the ignorance of the vertical plasma motion driven by Alfvén waves.

In such a case, there are several potentials to further develop the model. For example, the Hall term can be added into the model to investigate the horizontal coupling processes. The spatial grids of the model could be non-uniform, and then the model could be used to simulate the Alfvén wave propagation in the whole closed flux tube, e.g. Field Line Resonance (FLR) events.

Chapter 6. Boundary Condition Dependence of IARs

6.1. Introduction

In Chapter 5 a numerical model was introduced and tested in detail. Both in Fig 5.7 and Fig 5.9, it is quite clear that the eigenfrequencies of IARs are affected by not only the structure of the resonance cavity but also the boundary conditions. At the beginning of Chapter 5 it was mentioned that the numerical model would be utilized to investigate the relationship between the IAR eigenfrequency shifts and the plasma density perturbation in the ionosphere. Thus it is necessary to investigate the boundary condition dependence of IARs in more detail first.

Also, there have been observations of IARs by spacecraft [Robinson et al, 2000; Grzesiak, 2000]. It is quite interesting to see whether the boundary condition of the E region could influence the data detected by satellites or not. The spatial structures of the electric field will be investigated in this chapter based on different boundary conditions. Artificial heating experiments to stimulate Alfvénic resonances in the ionospheric resonance cavity have become a very important method to study the Magnetosphere-Ionosphere coupling processes [Robinson et al, 2000; Scoffield et al, 2006]. For example, artificial experiments could accelerate the particle precipitation from the magnetosphere to the ionosphere. As the result the plasma density profile in the ionosphere could be significantly changed. However, the data collected by ground based systems could be affected by boundary conditions of the IAR [Hirose & Lonngren, 1985; Trakhtengerts, 2000a; Belyaev et al, 1990]. In this chapter, the boundary condition dependence of artificial heating experiments will be investigated based on the numerical model introduced in Chapter 5. The heating experiment which carried out on 8 October 1998 [Robinson et al, 2000] will be modeled, and the best time interval for artificial heating experiments on that day will be theoretically estimated.

Obviously there are many factors for the boundary conditions of IARs such as Pedersen conductivity, wave impedance etc. This chapter will just focus on the ratio between the height integrated Pedersen conductivity and the wave conductivity at the E-peak, which was supposed to be the bottom boundary of the IAR.

6.2. Boundary Conditions and the Eigenfrequencies

For an idealized resonance cavity, there are two types of idealized reflective boundary conditions, which are fixed boundaries and free boundaries [Hirose & Lonngren, 1985]. The restoring force at a fixed boundary is always infinite, thus the wave amplitude at this boundary is always 0; the restoring force at a free boundary is always 0, thus the wave amplitude at this boundary is always two times of the amplitude of the wave crests. Both of the two types of boundaries could perfectly reflect waves trapped in the resonance cavity. However, in a more realistic case, if the wavelength is much greater than the thickness of the reflective boundary, the thickness of the bottom boundary could be ignored. A resonance cavity form by such reflective boundaries could have wave nodes or wave antinodes on the boundaries. More details can be seen in Fig 6.1.

The resonance cavities shown in Fig 6.1 are IARs (Ionospheric Alfvén Resonators). The Alfvén velocity within the cavities was fixed to be 2000km/s. That means the Alfvén velocity profile is uniform within the resonance cavity; the cavity sizes are fixed to be 1000km. In realistic cases the top reflective boundaries of IARs are the exponential Alfvén velocity profiles above the F2 peak. The Alfvén velocities increase with altitudes. Fig 5.1 in Chapter 5 illustrated an example of realistic situation. Thus in these idealized resonance cavities the top reflective boundaries were formed by Alfvén velocity gradients. The Alfvén velocity above the top boundary was 10 times of the Alfvén velocity below. For the lower reflective boundaries, Pedersen conductivities were set to reflect Alfvén waves traveling downwards and reach the bottom boundary. All the model equations are same as the model introduced in Chapter 5.

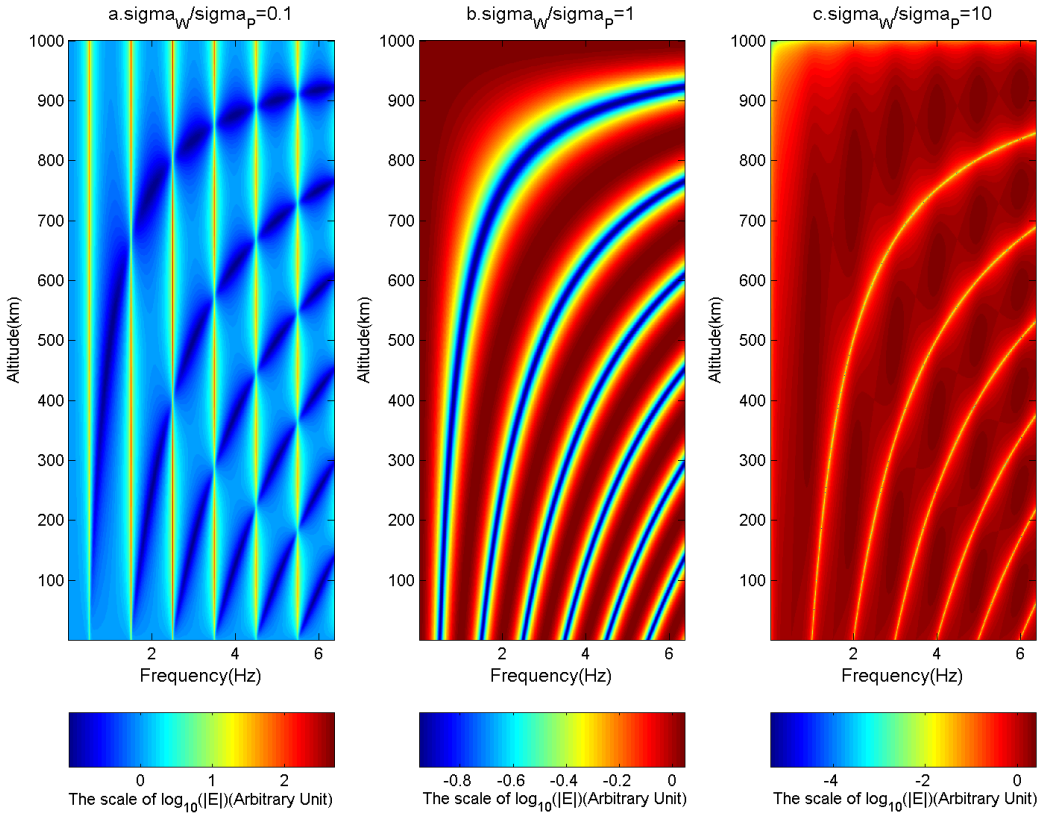

Fig 6.1 The spatial structure of the electric field intensity. The top boundaries in all the panels are same. The Σ_W / Σ_P in panel a, b and c are 0.1, 1 and 10, respectively. The color bar is shown at the bottom of each panel. The sizes of the cavities are same, which are 1000km, while the Alfvén velocities are uniform and same, which is 2000km/s.

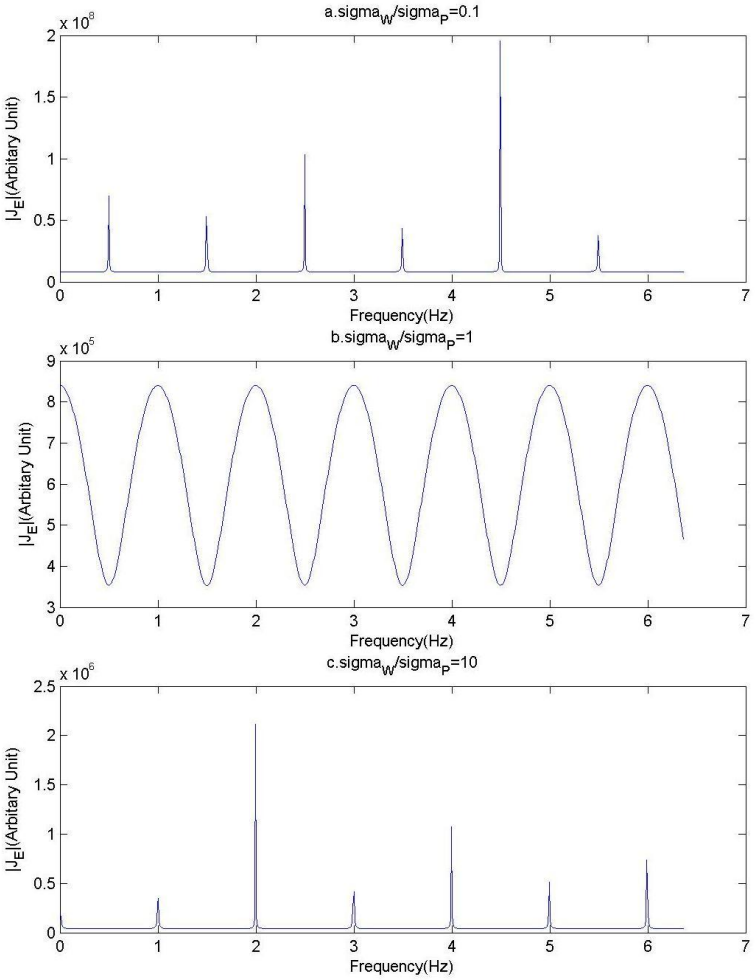

Fig 6.2 The total current at the bottom boundaries of the cavities shown in Fig 6.1. Panel a, b and c illustrate the total current at the bottom boundaries of $\Sigma_W / \Sigma_P = 0.1$, 1 and 10, respectively.

The ratio between the Alfvén wave conductivities and the Pedersen conductivities are different in those panels. In panel a, b and c, the ratios are 0.1, 1 and 10, respectively. According to equation 6.1 [Trakhtengerts, 2000a],

$$R_i = \frac{1-\Sigma_P/\Sigma_W}{1+\Sigma_P/\Sigma_W} \tag{6.1}$$

where R_i , Σ_P and Σ_W are the reflective coefficient, height integrated Pedersen conductivity and the Alfvén wave conductivity at the bottom boundary of IAR, respectively, the reflective coefficients of the bottom boundaries of panel a, b and c are negative, zero and positive, respectively. Negative and positive reflection coefficients mean the phase of the reflected waves is opposite to and same as the incident waves, respectively. When it equals to zero, there is no reflection at the bottom boundary, which leads to a much lower Q-factor of the resonance cavity. The definition of the Alfvénic wave conductivity is completely same with the definition in Chapter 5 and 6. The corresponding color bar is shown to the right of each panel. It should be noticed that the scale of the color bars are different. That was caused by the different Q-factors. The ratio between the Alfvén wave conductivities and the Pedersen conductivities could strongly influence the Q factor of IARs. The source oscillating electric field was fixed to be 1. The Pedersen conductivity was determined by the wave conductivity at the bottom boundary and the ratio between the wave conductivity and the Pedersen conductivity. Thus the intensities of source current of the three panels are different.

Clear wave structures can be seen in all the panels of Fig 6.1. However, it is quite clear that the resonance frequencies in the three cavities are different. In panel a the resonance frequencies are half integer frequencies. In panel b and c the resonance frequencies are integer frequencies. In panel b the wave structures are much broader in the frequency domain. That was caused by the reflective coefficient of the bottom boundary. According to equation 6.1, the reflective coefficient is zero at the bottom boundary, i.e., there was no reflection in panel b. Thus all the reflective processes occurred at the top boundary. Due to the existence of both the top reflective boundary and the source current, the Alfvén waves were trapped within the cavity. However, the Q factor was too low due to the zero reflection at the bottom. That is why the wave

structures are quite different from the structures in panel a and panel c. The total current intensity at the bottom boundaries of the three panels can be seen in Fig 6.2.

Panel a, b and c in Fig 6.2 illustrate the total Pedersen current at the bottom boundaries of the resonance cavities which were shown in Fig 6.1, respectively. The total current intensity includes the Pedersen current driven by the wave field and the source current. It can be seen that the eigenfrequencies in panel a are half integer frequencies. However, in panel b and c the eigenfrequencies are integer frequencies. Those agree with Fig 6.1. It should be noticed that the scales of y-axis are different in the three panels. That was caused by the differences of the Q-factor of the resonance cavities.

For a more realistic IAR, the total respond at the bottom boundary could be different and more complicated. Fig 6.3 illustrates the spatial structures of the electric field intensity of different boundary conditions. The profile utilized in this plot was generated by IRI2007 model. The time interval of the profile is 18UT, 04/10/98. The location is Sodankylä. This profile has been utilized in Chapter 5 to test the numerical model, which was shown in Fig 5.1. The numerical results agreed with observed data. Thus the profile was also utilized in some numerical studies in this chapter. The Σ_W / Σ_P in panel a, b and c are 0.1, 1 and 10, respectively.

The wave structures are quite clear in all of the three panels of Fig 6.3. However, the spatial structure of the field intensity shown in panel a is quite different from the structures in panel b and c. In order to see more details, the total electric field intensity and the Alfvén wave electric field intensity are illustrated in Fig 6.4. In panel a, b and c the values of Σ_W / Σ_P are 0.1, 1 and 10, respectively. In each panel the scale of the wave field intensity is the left y-axis and the total field intensity scale is the right y-axis. In each panel the blue line and the black line illustrate the wave field and the total field, respectively. It can be seen that the peaks and troughs of the intensities of the total and wave electric fields are different in panel b and c. That is caused by the difference of the phases of the source electric field and the wave electric field at the E-peak.

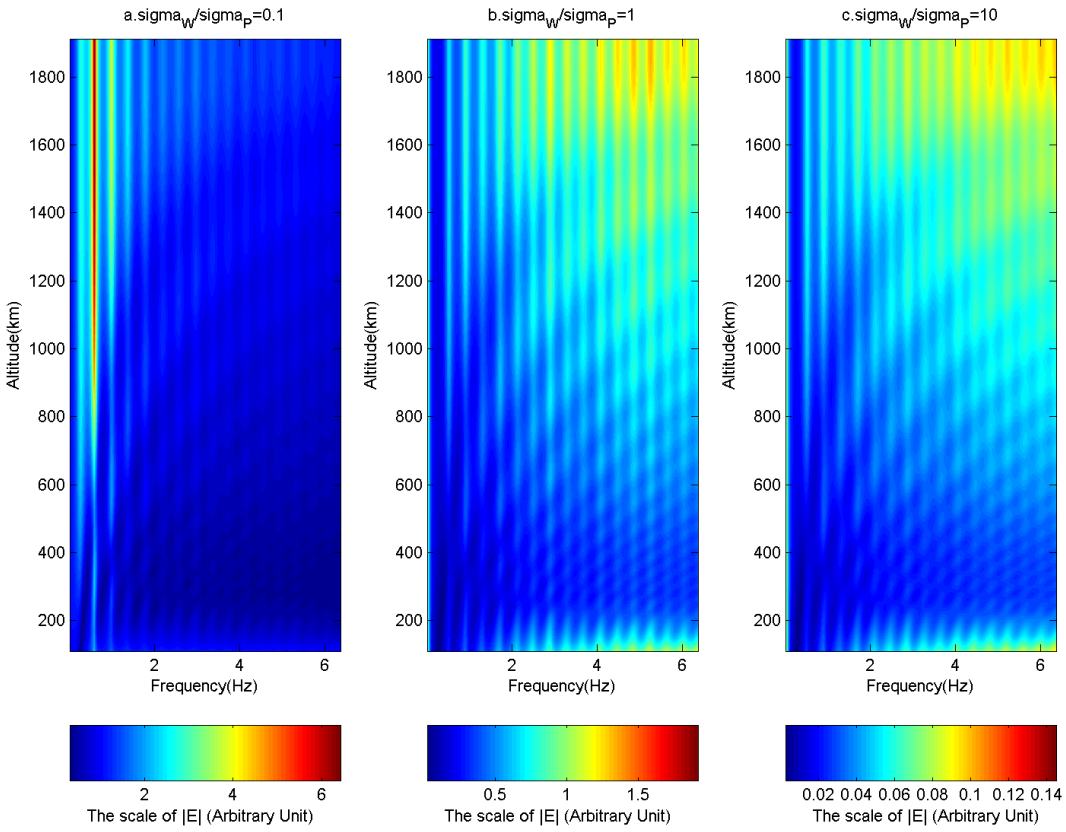

Fig 6.3 The plot illustrates the spatial structure of the absolute values of the electric field for the interval of 18UT, 04/10/98, SOD. The color bar at the bottom of each panel shows the scales of the electric field intensities in the resonance cavity.

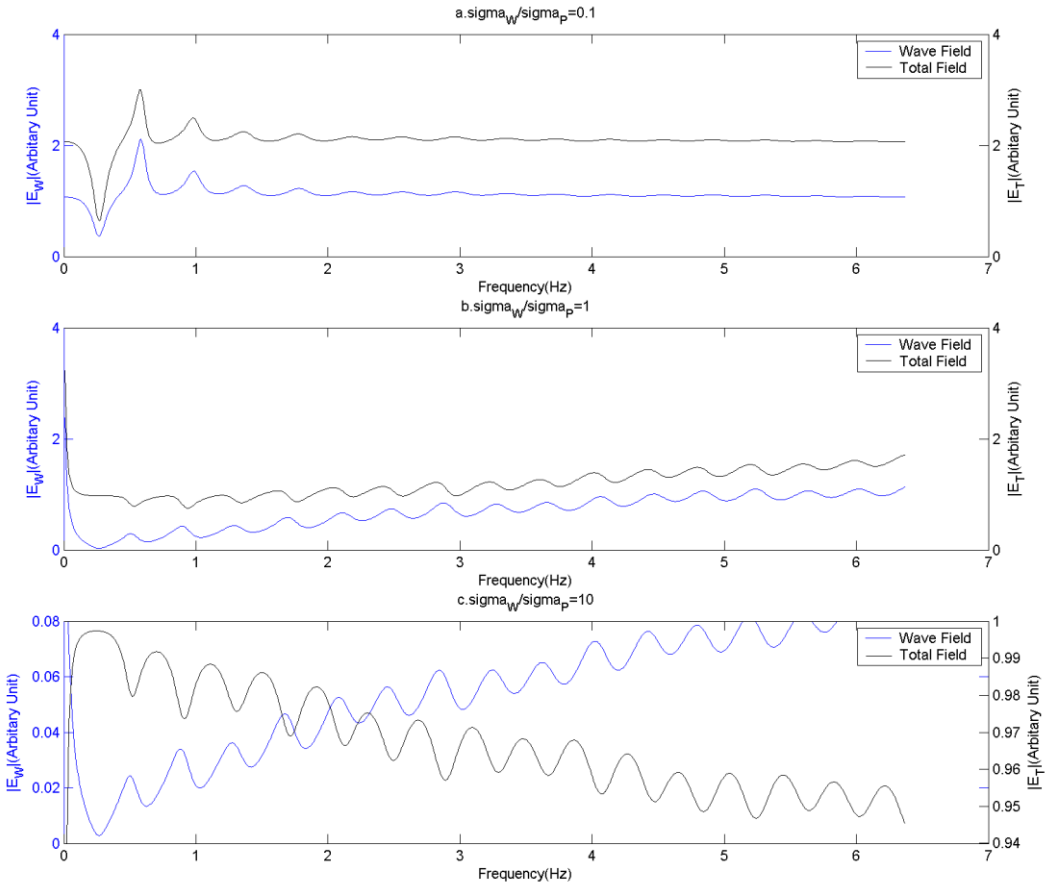

Fig 6.4 The figure illustrates the wave electric field intensity and the total electric field intensity at the bottom boundary of the IARs which were shown in Fig 6.3. In panel a, b and c the values of Σ_W / Σ_P are 0.1, 1 and 10, respectively. In each panel the scale of the wave field intensity is the left y-axis and the total field intensity scale is the right y-axis. In each panel the blue line and the black line illustrate the wave field and the total field, respectively.

Both the trapped waves and traveling waves are oscillating in the cavities. However, ground based observations just detect the signals stimulated by the total current at the bottom of the IAR. The total is proportional to the total electric field intensity. On the other hand, the in-situ observations detect the field within the cavities [Robinson et al, 2000]. That means for an individual IAR event, the eigenfrequencies detected on the ground could be different from the eigenfrequencies detected by satellites when the ratio between the wave conductivity and the Pedersen conductivity is greater than or equal to 1. Also, it can be seen that the troughs and peaks in panel b and c are different from those in panel a. Those troughs and peaks in panel b and c are on same frequencies. The frequencies of troughs and peaks in panel a are reversed. That agrees with the differences of the wave structures illustrated in Fig 6.3. In panel a, the troughs and peaks of the wave field and the total field match each other. In such a case the eigenfrequencies observed on the ground and by satellites would be same. In other words, for a give Alfvén velocity profile, the eigenfrequencies of the IAR strongly depend on the ratio between the wave conductivity and the height integrated Pedersen conductivity. Also, this ratio makes great contribution to determine whether the eigenfrequencies observed on the ground and by satellites are same or not. Panel b and panel c shown the situations that the eigenfrequencies observed on the ground could be different from the resonance frequencies.

In addition, in panel c of Fig 6.4 it should be noticed that the scales of the wave field intensity and the total field intensity are different. The intensity of the wave fields is only about 10% of the intensity of the total field. That implied the source current would make the main contribution to the signals detected on the ground, and the wave field is relatively much weaker compared with the situations shown in panel a and panel b. This feature will be investigated in more details in section 6.4, and the best time interval for heating experiments to stimulate artificial IARs will be estimated based on this feature.

6.3. The Spatial Structure of the Electric Field

The different spatial structures of the electric field intensities were illustrated in Fig 6.3 when the ratios between the Alfvén wave conductivity and the height integrated Pedersen conductivity are different. According to the discussion in section 6.2 the

differences of the spatial structures of the electric field intensities were caused by the bottom boundary condition. In this section, the spatial structures of the electric field intensity will be investigated in more detail based on the same Alfvén velocity profile and the numerical model. Particularly the study in this section will focus on the relationship between the electric field intensity above the E peak and the values of Σ_W / Σ_P at the E peak.

The electron density profile and the Alfvén velocity profile are shown in Fig 6.5. Panel a illustrates the electron density profile in the range of 110km to 2000km. The profile was generated by IRI2007. Panel b illustrates the Alfvén velocity profile, which was worked out based on the electron density profile and the percentage profile of ion species. The percentage profile was also generated by IRI2007. The altitude of the E peak was 110km, which was at the bottom of the profiles. Thus the total available length of the resonance cavity is 1890km. In the numerical computation the length was selected to be 1800km. That means the maximum altitude that taken into account in the study was 1910km. Basically this height is lower than some of the satellites orbits altitudes. In other words, this maximum altitude may not high enough to simulate the satellite observations for a specified event. Thus the study is aimed at qualitatively investigate the features of the data collected by satellites. The F2 peak was at 292km.

According to Fig 6.4 the resonance frequencies can be affected by Σ_W / Σ_P at the E peak. Also, the exact resonance frequencies could be found according to the peaks of the curves in Fig 6.4.

Fig 6.6 illustrates the comparisons of different ratios between Σ_W and Σ_P. Wave intensities are illustrated in the panels. The left y-axis represents the scale of the wave intensity of the smaller Σ_W / Σ_P and the right y-axis represents the scale of the wave intensity of the greater Σ_W / Σ_P in each panel. The blue and the red dashed lines highlight the peak frequencies of the same colour of the solid lines in each panel; the dotted lines highlight the trough frequencies of the same colour of the solid lines in each panel. In panel a and b it is quite obvious that the peaks and troughs of different Σ_W / Σ_P do not match each other. However, in panel c it can be seen that the peaks and troughs

are on same frequencies when Σ_W / Σ_P equals to 1 and 10. The comparison of the spatial wave intensity structures for peak, trough and arbitrary frequencies can be seen in Fig 6.7.

In panel a of Fig 6.7, 0.99Hz and 1.17Hz are peak and trough frequencies for Σ_W / Σ_P =0.1; 1.07Hz is an arbitrary frequency in between. In panel b and c, 0.90Hz and 1.03Hz are peak and trough frequencies for Σ_W / Σ_P =1 and 10; 1.03Hz is an arbitrary frequency in between. Clear wave structures, which are the quasi-harmonic structures, can be seen in those panels. However, those are not real harmonic structures because the wavelengths change with Alfvén velocity variation and the Alfvén velocity changes with altitude. It should be noticed that all the field intensities illustrated in this figure are the absolute values, thus there are only positive intensities, i.e., every two quasi-harmonic structures represent a single wavelength. The selected frequencies are around 1Hz, which is relatively low, thus there are not many wavelengths in those panels.

The horizontal axes in Fig 6.7 are electric field intensities in arbitrary unit. The vertical axes are altitudes covering the range from 110km to 2000km. The scales of those horizontal axes are different. That is caused by the different source current. The source current in Fig 6.7 is set based on a constant electric field which drives the source current and the value of Σ_W / Σ_P. Thus the intensities of the source current in those panels are different, which lead to the difference of the total current at the bottom boundary. The resonance components are illustrated by the blue lines in Fig 6.7. It can be seen that the field intensities of the resonance components are greater than other components except at the altitudes close to wave nodes. However, the resonance component is always stronger than other components in panel a and the resonance components is always stronger than the component at the trough frequency in panel b. In panel c the resonance component could be even weaker than the component that at the trough frequency at certain altitudes. Thus, for in-situ measurements, it would be easier to distinguish the resonance components from others when value of Σ_W / Σ_P is small. In other words, Σ_W / Σ_P could significantly affect the signal intensities observed by spacecraft when measuring IARs. Also, it could significantly affect the difference of the signal intensities between resonance components and non-resonance components. More details can be seen in Fig 6.8.

Fig 6.8 illustrates the wave field intensity against Σ_W / Σ_P for specified frequencies and altitudes. The electric field and the Alfvén velocity profile are fixed. The x axes are logarithmic. The blue, red and black lines illustrate the wave intensities at 600km, 1100km and 1600km, respectively. 0.99Hz and 0.90Hz are resonance frequencies for Σ_W / Σ_P =0.1 and 1, respectively. 3.0Hz is frequently used for artificial heating experiments. It can be seen that for those frequencies and altitudes, the signal intensities increase with Σ_W / Σ_P till the intensities reach certain maximums, then decrease. The values of Σ_W / Σ_P corresponding to the maximums are different for different frequencies. The maximums for a certain frequency correspond to the same value of Σ_W / Σ_P at different altitudes. The wave field intensities increase with altitudes for a specified frequency. It should be noticed that the minimum altitude illustrated in this figure is 600km; however, the altitude of the F2 peak is 292km, which is much lower than 600km. That implied that the situation might be different below the F2 peak. In such a case, according to the scales of the vertical axes, the resonance signal intensities are stronger at lower Σ_W / Σ_P. That implies the IAR is easier to detect by satellites when Σ_W / Σ_P is close to 0.1 for a specified horizontal scalar potential and an Alfvén velocity profile.

6.4. Artificial Heating Experiments

According to the study in section 6.3, the value of Σ_W / Σ_P could affect the electric field intensities of Alfvén waves. The electric field intensities of Alfvén waves in the E region have impacts on the total Pedersen current. For ground observations, the signals of magnetic field collected by pulsation magnetometers are stimulated by the Pedersen current in the E region. Thus it could expect that the values of Σ_W / Σ_P have impacts on ground observations, which can be seen in Fig 6.9. In heating experiments to stimulate artificial IARs, ground observations are quite important for collecting the data of the results [Scoffield et al, 2006; Yeoman et al, 2008]. The pulsation magnetometer observation could be the only way to collect the data of the results of heating experiments when there is no satellite in appropriate orbits. Thus the value of Σ_W / Σ_P

should be taken into account in artificial heating experiments.

Fig 6.9 illustrates the total Pedersen current and source current intensities. In panel a, b and c, Σ_W / Σ_P=0.1, 1 and 10, respectively. The solid lines illustrate the total current intensities. The dashed lines illustrate the intensities of source current. The horizontal scalar potential is fixed. Due to the difference of the values of Σ_W / Σ_P, the source current intensities are different. As the result, the electric field which drives the source current is fixed. The Alfvén velocity profile utilized in this figure is shown in Fig 6.5. Clearly the current intensities are quite different. On the other hand, the total current is not always stronger than the source current. In panel c, it can be seen that the total current is always weaker than the source current when Σ_W / Σ_P=10. If an artificial heating experiment took place in such a situation, the signal strength detected by a ground based pulsation magnetometer would be lower than the strength of the heating signals. Thus in order to obtain clear and strong respond signals on the ground in an artificial heating experiment, it is necessary to investigate not only the Alfvén velocity profile but also the ratio between the wave conductivity and the height integrated Pedersen conductivity. However, for a specified time interval, the ratio between the wave conductivity and the height integrated Pedersen conductivity is determined by the ionospheric conditions, particularly the conditions of the E region. Hence it is necessary to find a method to estimate the values of Σ_W / Σ_P.

Equation 6.2 illustrates the relationship between the height integrated Pedersen conductivity and the plasma density. Equation 6.3 illustrates the equation of the Alfvénic wave conductivity at the E peak. Equation 6.4 is the Alfvén velocity at the E peak.

$$\Sigma_P \propto N_E \tag{6.2}$$

$$\Sigma_W(z_E) = \frac{1}{\mu_0 V_A(z_E)} \tag{6.3}$$

$$V_A(z_E) = \frac{B}{\sqrt{\mu_0 m_i(z_E) N_E}} \tag{6.4}$$

where N_E is the plasma density in the E region, z_E is the altitude of the E peak, μ_0 is the vacuum permeability, V_A is the Alfvén velocity, m_i is the mean mass density for

ions and B is the geomagnetic field strength.

According to equation 6.2, 6.3 and 6.4, the relation between Σ_W / Σ_P and the plasma density at the E peak can be obtained, which is shown in equation 6.5.

$$\Sigma_W / \Sigma_P \propto 1/\sqrt{N_E} \tag{6.5}$$

The vertical profile of the Pedersen conductivities is difficult to obtain. Thus it assumed that the height integrated Pedersen conductivity is proportional to the conductivity at the E peak. Based on this assumption, Σ_W / Σ_P is proportional to the reciprocal of the root of the plasma density at the E peak. The hourly variation range of the ratio between the wave conductivity and the height integrated Pedersen conductivity is from 0.1 to 10 [Belyaev et al, 1990]. Thus the hourly values of Σ_W / Σ_P can be estimated, and based on the estimated values of Σ_W / Σ_P, the best time intervals in a single day for a specified artificial heating experiment can be worked out. There was a heating experiment to stimulate an artificial IAR on 08/10/98 at Tromsø by EISCAT Tromsø heating facility in Norway. The geographic latitude and longitude of the heating facility, which was constructed in 1979, is $69°35'N, 19°14'E$. This experiment will be taken for example to estimate the best time interval for artificial heating experiment on that day.

Fig 6.10 illustrates the hourly Alfvén velocity profiles at Tromsø on 08/10/98. The profiles were worked out based on the data generated by IRI2007 and the magnetometer data which is available on the website of Tromsø Geophysical Observatory (TGO) (http://flux.phys.uit.no/cgi-bin/geodata.cgi?site=tro2a). The observatory is operated by University of Tromsø. The x-axis in Fig 6.10 is the universal time. The y-axis is the altitude, which covers the range from 110km to 2000km. The color bar on the right illustrates the scale of the Alfvén velocities in the unit of m/s. According to the plasma density profile generated by IRI2007, the altitude of the E peak was at 110km during the whole day. The local time was 2 hours prior the universal time on that day at Tromsø. The period shown in this figure covers 0 UT to 23 UT on 08/10/98, which means it is 2 LT on 08/10/98 to 1 LT on 09/10/98. The EISCAT Tromsø heating facility was heating the ionosphere continuously during the interval of 20:15 UT to 20:45 UT [Robinson et al, 2000], which is 22:15 LT to 22:45 LT. Tromsø is inside the Arctic Circle, thus it was polar dusk on that day. In Fig 6.10 it can be seen that the Alfvén velocities are higher in the area above 1000km and close to the E peak around the local midnight. That was

caused by the decreases of the plasma density at night. The effective size of the resonance cavity change with the variation of the Alfvén velocity profile. Thus eigenfrequencies of the ionospheric Alfvénic resonance cavity change with the effective size of the cavity. The heating frequency was fixed at 3Hz in the experiment. Thus the frequency taken into account in this study will be 3Hz as well. According to Fig 6.9, the ratio between total current densities and source current densities changes with frequency. So the frequency of 3Hz could be the frequency of peak or trough, or the frequencies in between at different time of the day. That would have some impacts on the signal intensity detected on the ground if the heating experiment took place at different time intervals. Those impacts will be taken into account in the numerical computation.

According to equation 6.5 and the hourly Alfvén velocity profiles, the value of Σ_W / Σ_P for each hour could be estimated. The hourly variation of $1/\sqrt{N_E}$ is illustrated in panel a of Fig 6.11. It can be seen that the maximums are at night time, including the intervals of 0 UT to 4 UT and 19 UT to 23 UT. The minimum is around the noon. The maximum value of Σ_W / Σ_P is about 10, and the minimum is about 0.1 [Belyaev et al, 2000]. There are several factors could affect the values of Σ_W / Σ_P, particularly the Σ_P. However, in order to estimate the hourly values of Σ_W / Σ_P on 08/10/98 at Tromsø, all the factors are ignored except the reciprocal of the root N_E. That means in order to estimate Σ_W / Σ_P, a purely linear relation between Σ_W / Σ_P and $1/\sqrt{N_E}$ is assumed. Thus according to equation 6.5, the hourly variation of Σ_W / Σ_P could be estimated. Due to this linear relation, the ratio between Σ_W / Σ_P and $1/\sqrt{N_E}$ is a constant during the whole day. Then the hourly variation of Σ_W / Σ_P could be obtained. It can be seen in panel b of Fig 6.11. The minimum and the maximum are 0.1 and 10, respectively.

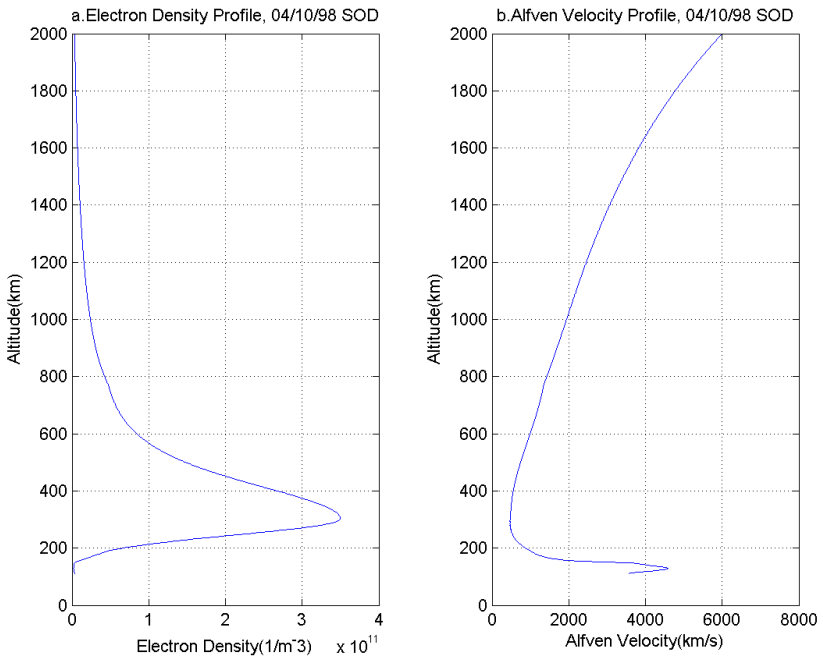

Fig 6.5 The plot illustrates the electron density profile and the Alfvén velocity profiles of 18UT, 4 Oct 1998 in Sodankylä. The density profile shown in panel a was generated by IRI2007. The Alfvén velocity profile was worked out based on the density profile and the percentage profile of ion species, which was also generated by IRI2007.

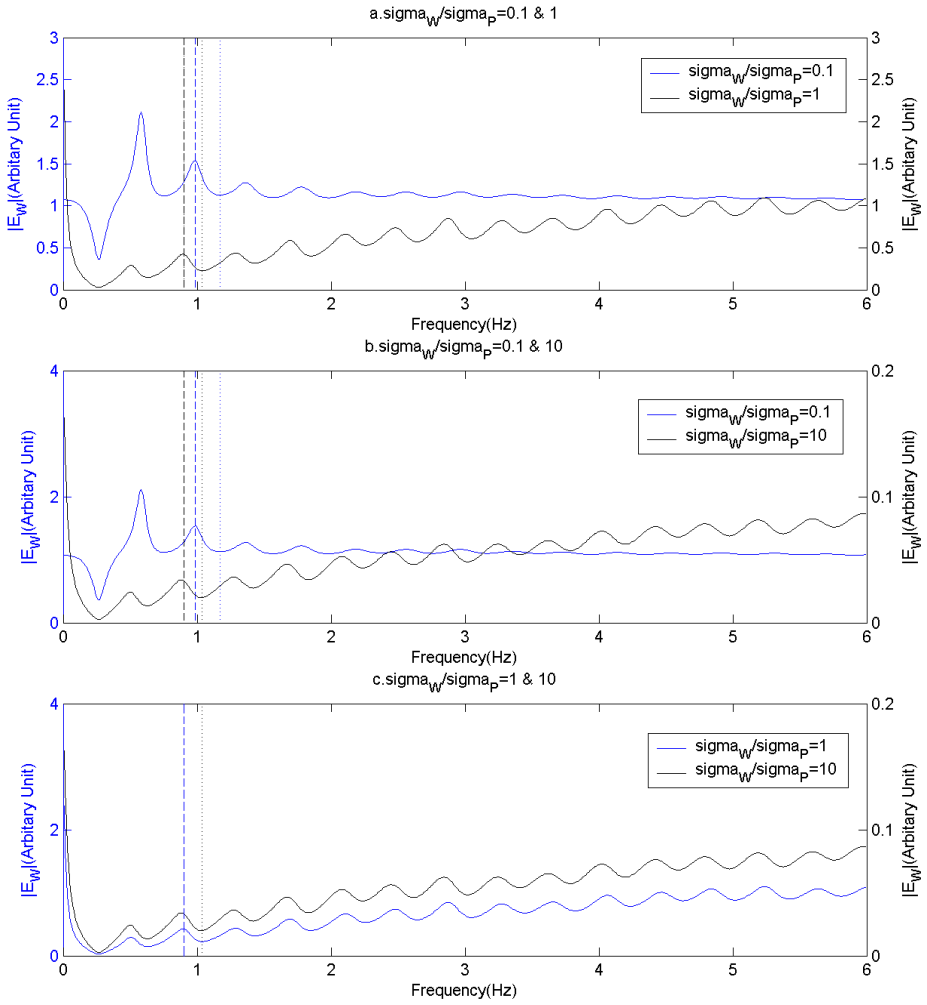

Fig 6.6 The comparisons of different ratios between Σ_W and Σ_P are illustrated in the figure. The blue and red solid lines illustrate the wave field intensities. The blue and the red dashed lines highlight the peak frequencies of the same colour of the solid lines in each panel; the dotted lines highlight the trough frequencies of the same colour of the solid lines in each panel. Left axes always represent the scale of the wave intensity of the smaller Σ_W / Σ_P and the right axes always represent the scale of the wave intensity of the greater Σ_W / Σ_P in this figure.

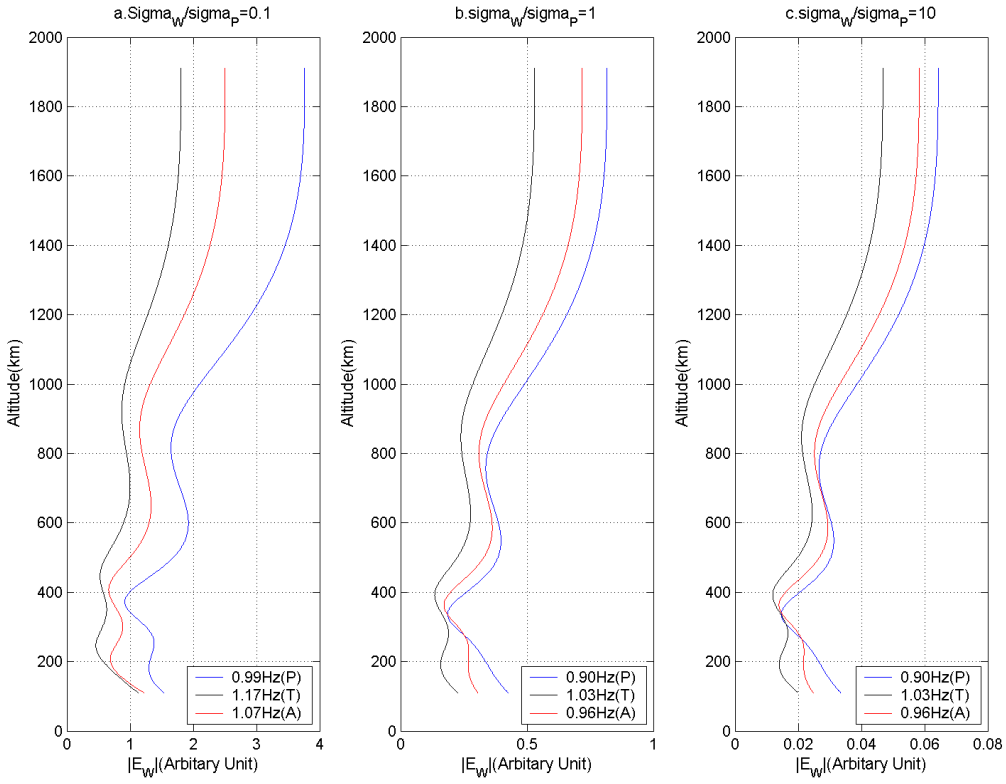

Fig 6.7 The comparisons of the spatial structures of different frequencies. In panel a, 0.99Hz and 1.17Hz are peak and trough frequencies of Σ_W / Σ_P =0.1; 1.07Hz is an arbitrary frequency in between. In panel b and c, 0.90Hz and 1.03Hz are peak and trough frequencies of Σ_W / Σ_P =1 and 10; 1.03Hz is an arbitrary frequency in between.

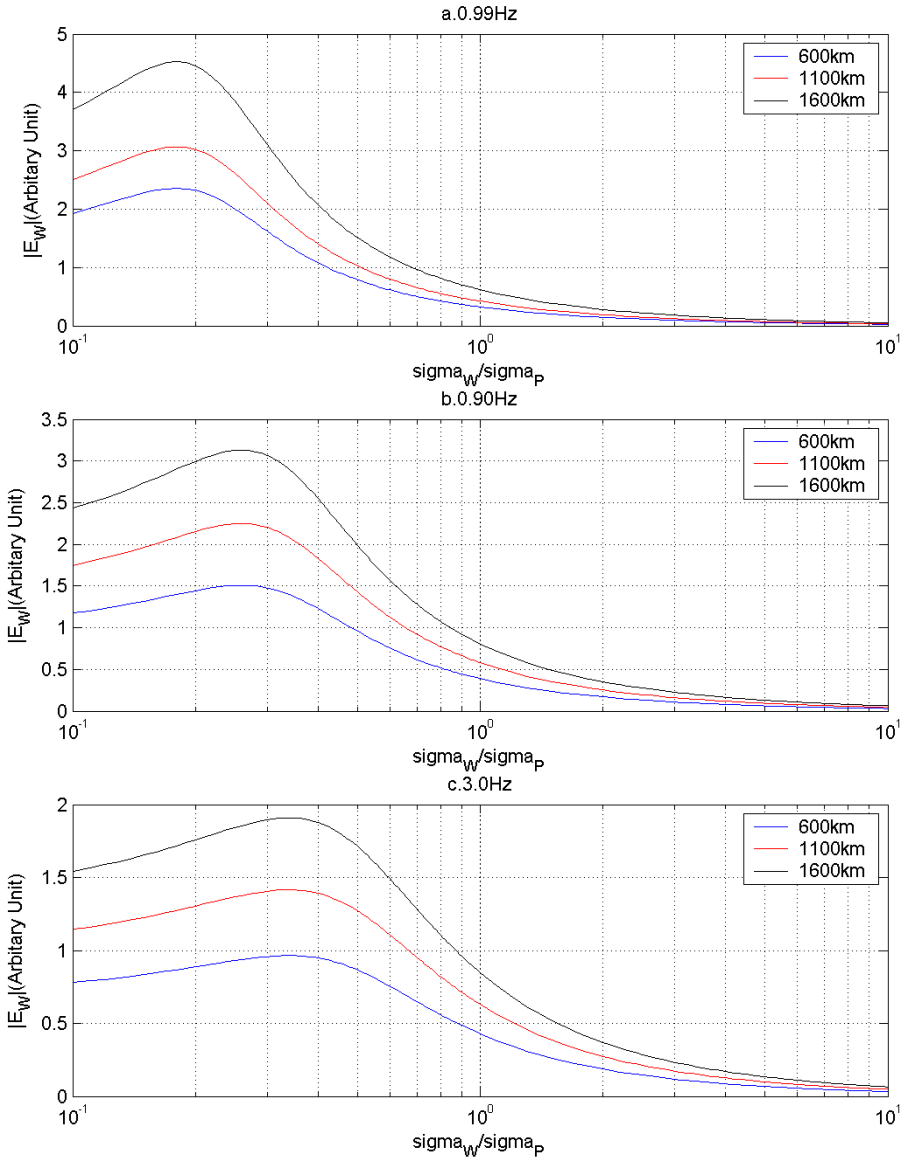

Fig 6.8 The figure illustrates the wave field intensity against Σ_W / Σ_P for specified frequencies and altitudes. The x axes are logarithmic. The blue, red and black lines illustrate the wave intensities at 600km, 1100km and 1600km, respectively. 0.99Hz and 0.90Hz are resonance frequencies for Σ_W / Σ_P =0.1 and 1, respectively. 3.0Hz is frequently used for artificial heating experiments.

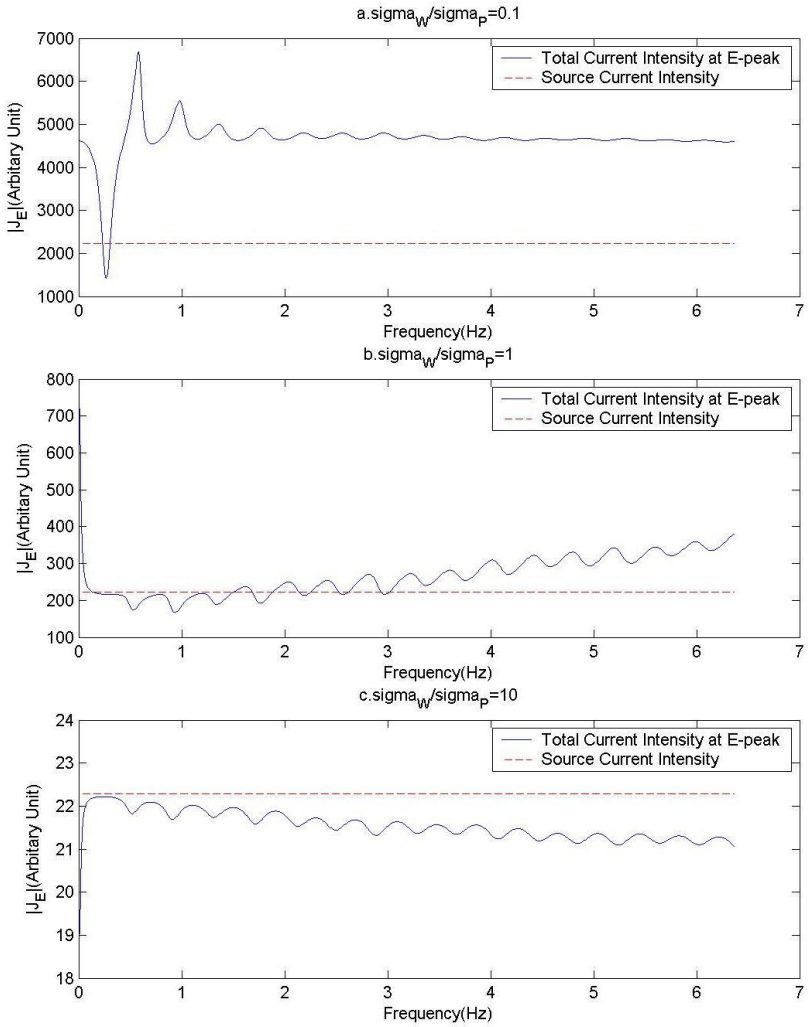

Fig 6.9 The total Pedersen current and source current intensities are illustrated in the figure. In panel a, b and c, Σ_W / Σ_P =0.1, 1 and 10, respectively. The solid lines illustrate the total current intensities. The dashed lines illustrate the intensities of source current. The Alfvén velocity profile utilized in this figure is shown in Fig 6.5.

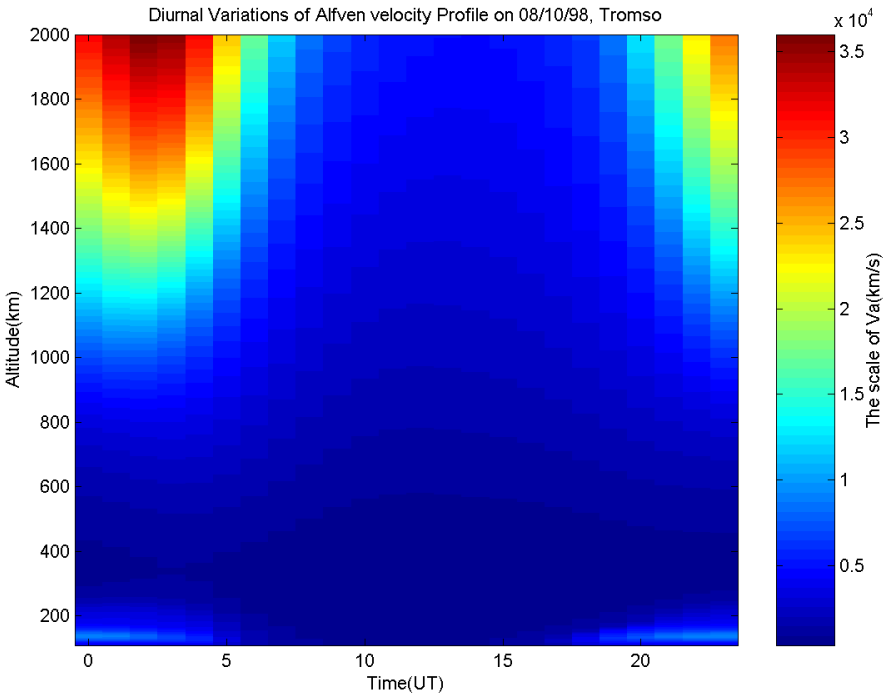

Fig 6.10 The daily Alfvén velocity profiles of 08/10/98, Tromsø. The profiles were generated by IRI2007. The color bar on the right illustrates the scales of the Alfvén velocities. The unit of the color bar is m/s.

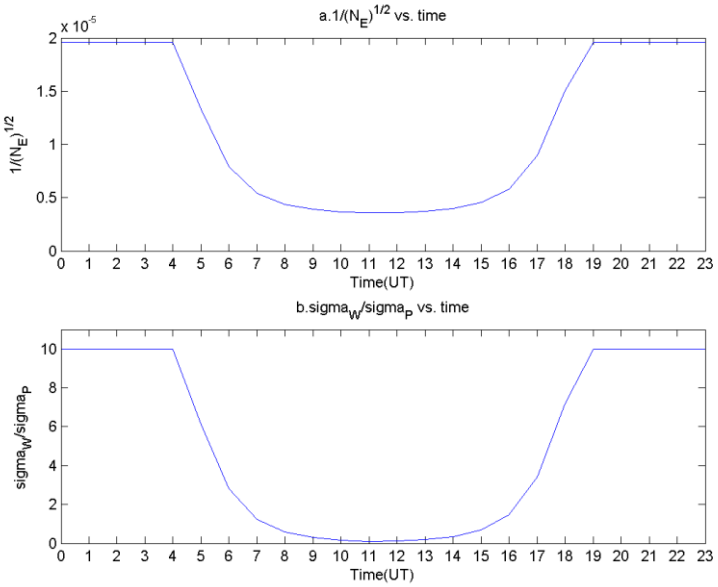

Fig 6.11 Panel a illustrates the reciprocal of the root N_E against the universal time on 08/10/98 at Tromsø. Panel b shows the ratio between the Alfvénic wave conductivity and the height integrated Pedersen conductivity at the E peak.

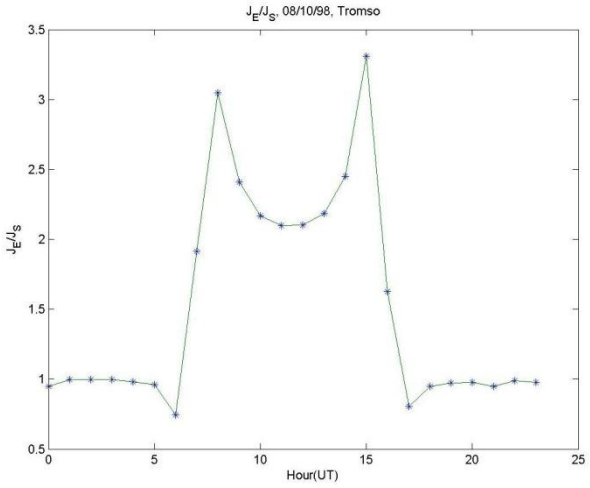

Fig 6.12 The ratios between the total current intensity and the source current intensity during the whole day of 08/10/98 at Tromsø. The maximum responds appear at 8UT and 15UT.

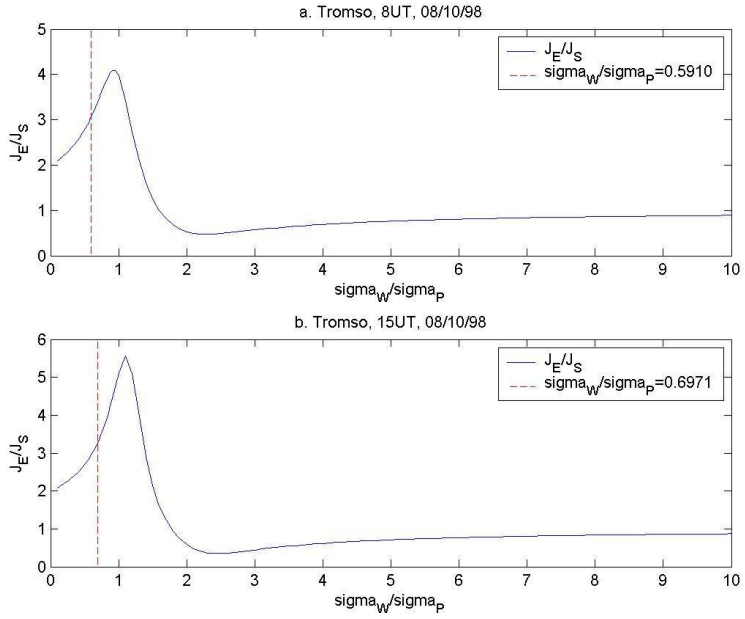

Fig 6.13 The figure illustrated the time intervals of the maximum ratio between the total current intensities and the source current intensities at the E peak on 08/10/98 at Tromsø. The solid lines represent the different ratios against Σ_W / Σ_P in the range from 0.1 to 10. The dashed lines illustrate the estimated ratios of the corresponding Σ_W / Σ_P.

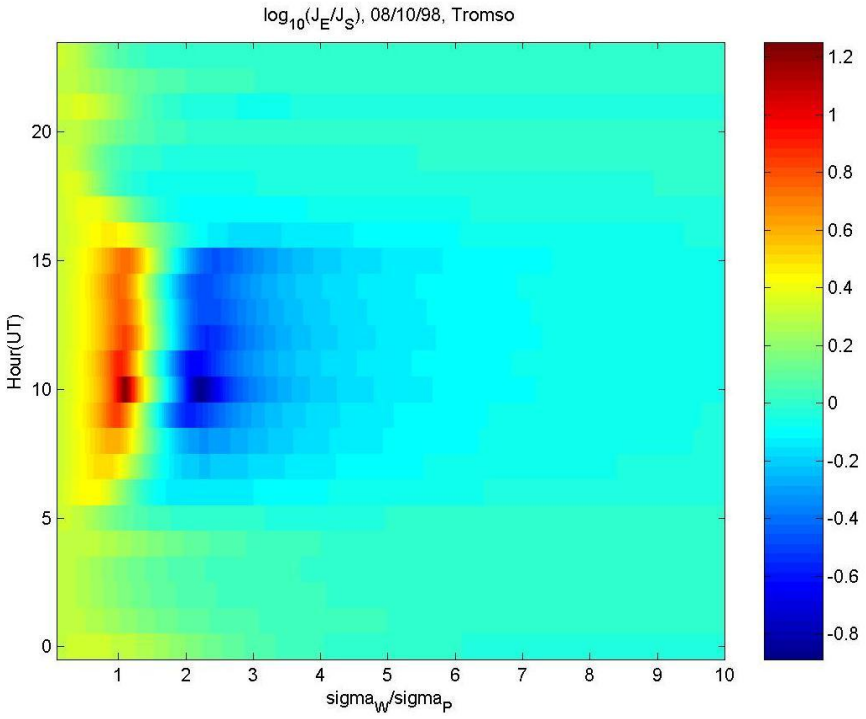

Fig 6.14 The figure illustrates the ratio between the Alfvén wave conductivity and the height integrated Pedersen conductivity and the ratio between the total electric field intensity and the source field intensity for the whole day of 08/10/98 at Tromsø. The color bar is shown to the right of the plot, which is a logarithmic scale.

Based on the hourly variation of Σ_W / Σ_P, the hourly ratio between the total current intensity and the source current intensity can be obtained, which is illustrated in Fig 6.12. J_E is the intensity of the total current at the E peak; J_S is the intensity of the source current intensity. The E peak is the bottom boundary of the IAR. The maximum ratios shown in this plot appear at 8 UT and 15 UT, which are 10 LT and 17 LT, respectively. The ratios are lower or close to 1 in the intervals of 0 UT to 6 UT and 17 UT to 23 UT. During those intervals, the power of the total respond signals would be smaller than the power of the heating signals that reach the heating patch due to the signal diffusion [Trakhtengerts, 2000a]. In Fig 6.12 it can be seen that the ratio slightly decreases from 5 UT until 6 UT, then it increase quickly until it reaches the maximum at 8 UT. After that the ratio decreased till about 12 UT. The second variation of the ratio in the second half of the day is almost symmetric with respect to the noon in universal time. According to Fig 6.10 it can be seen that the variation of the Alfvén velocity profile at high altitudes is symmetric with respect to about 13 UT. However, at lower altitudes the profile variation is symmetric with respect to about 11 UT, particularly at the altitudes close to the E peak. By comparing the symmetry in Fig 6.10 and Fig 6.12, the Alfvén velocity profile close to the E region makes more contribution to the ratio between the total current density and the source current density for an IAR.

Thus, according to the computation results shown in Fig 6.12, in order to obtain more observable and stronger respond signals, the best time intervals for artificial heating experiment on 08/10/98 at Tromsø should be around 8 UT and 15 UT, which are 10 LT and 17 LT, respectively. Particularly, interval around 15 UT could be better than 8 UT due to the greater ratio between the total current density and the source current density. The worst time intervals for artificial heating experiments on that day are around 6 UT and 17 UT because of the minimum respond. On the other hand, both of the two maximum ratios are greater than 3. That means the intensities of the response signals in the near the E peak are slightly greater than three times of the heating signal intensity that could reach the E region. The signals spread and weakened in the process of propagation from the E region to the ground. As the results the signal detected on the ground should be weaker than the signals in the E region. Thus, the signals received by the pulsation magnetometer would be much smaller than 3 times the heating signal emitted by the heating facility on 08/10/98 at Tromsø. According to the results, the

natural SRS signals should be most observable around 10 LT and 17 LT, and it should be with the highest observability around 17 LT. Though there is no natural IAR event on that day in Tromsø, however, that roughly agrees with the results of the statistical study on the IAR events observed by the pulsation magnetometer in Sodankylä Geomagnetic Observatory - which is 400km away from Tromsø - during the whole October in 1998. According to the statistical study, the SRS should be least observable around 12 LT. That does not agree with the computation results shown in Fig 6.12. It could be caused by the errors of the method of estimating the hourly Σ_W / Σ_P. By assuming the Σ_W / Σ_P varies between 0.1 and 10, the least square fitting shows Equation 6.5 is not satisfied. The fitted line does not cross the origin. That implies the value of Σ_W / Σ_P is not exactly in the range between 0.1 and 10. It could lead to errors.

Fig 6.13 shows more details of the maximum ratios at 8 UT and 15 UT. Panel a shows J_E / J_S against Σ_W / Σ_P of 8 UT; panel b shows J_E / J_S against Σ_W / Σ_P of 15 UT. The solid lines illustrate the ratio variation with Σ_W / Σ_P; the dashed lines highlight the estimated ratios. The values of Σ_W / Σ_P are 0.5910 and 0.6971 at 8 UT and 15 UT, respectively. It can be seen that both of the maximum ratios of the two are around Σ_W / Σ_P=1. However, neither of them reaches the maximum ratio of Σ_W / Σ_P. Both of the values of Σ_W / Σ_P are smaller than 1. It implied that the value of J_E / J_S could be even greater in more favourable conditions. It monotonically increases with Σ_W / Σ_P before it reaches the maximum. That means if the ionospheric condition is such as to make the value of Σ_W / Σ_P closer to 1, the ratio between the total respond and the effective heating signal could be greater.

However, the method introduced in this chapter for estimating the values of Σ_W / Σ_P is not quite accurate, and currently there is not enough observational evidence to compare with the numerical results. It should be noticed that other factors also make contribution to the height integrated Pedersen conductivity, e.g., the electron temperature in the E region. Every factor is not constant during the whole day. Thus the ratio between Σ_W / Σ_P and $1/\sqrt{N_E}$ is not really constant. In realistic cases, the variation of Σ_W / Σ_P is not exactly in the range of 0.1 to 10. For example, the maximum of Σ_W / Σ_P could be

greater than 10, or the minimum could be smaller than 10 in a specified day. In such a case, there are errors on each Σ_W/Σ_P estimated based on the method introduced in this chapter. Thus it is necessary to investigate the relation between J_E/J_S and Σ_W/Σ_P in more details to find the features of the relation. Fig 6.14 illustrates the hourly relation between $\log_{10}(J_E/J_S)$ and Σ_W/Σ_P for 08/10/98 at Tromsø. This figure was produced by calculating the value of $\log_{10}(J_E/J_S)$ in the whole range of Σ_W/Σ_P=0.1 to 10 for each hour. The color bar is to the right of the figure, which illustrates the scales of $\log_{10}(J_E/J_S)$. The x-axis of the plot is Σ_W/Σ_P. The y-axis of the plot is the universal time. The relation between $\log_{10}(J_E/J_S)$ and Σ_W/Σ_P is illustrated for each hour.

In Fig 6.14 it can be seen that the maximum values of $\log_{10}(J_E/J_S)$ appear when Σ_W/Σ_P is close to 1, particularly in the period from 5 UT to 16 UT. In the same period, when $\log_{10}(J_E/J_S)$ reaches the maximum, it decrease with $\log_{10}(J_E/J_S)$ and reach the minimum between 2 and 3. In addition, $\log_{10}(J_E/J_S)$ reaches its maximum when Σ_W/Σ_P=0.1 during the periods of 0 UT to 5 UT and 16 UT to 23 UT. The maximum values for the periods of 5 UT to 16 UT is greater than the other two periods. In other words, in order to obtain stronger respond signals, the heating experiments should be in the period of 5 UT to 16 UT on 08/10/98 at Tromsø. In the numerical estimation in this section, it was found that the best time intervals for artificial heating experiments are around 8 UT and 15 UT, which are within the period of 5 UT to 16 UT. However, referring to the data shown in Fig 6.11 and Fig 6.13, the values of Σ_W/Σ_P are closer to 1 at 7 UT, which is 1.23. It implies that for an artificial heating experiment, whether the value of Σ_W/Σ_P is close enough to 1 is not the only factor need to be taken into account to select the time intervals of the experiment. In order to obtain the strongest respond signal, both the value of Σ_W/Σ_P and the Alfvén velocity profile variation need to be taken into account.

On the other hand, it should be noticed that there has been a substorm occurred on 08/10/98. That means there are nonlinear processes in the magnetosphere, which could significantly change the plasma density profile in the ionosphere. This situation was not simulated by the IRI2007 quite well. Thus the numerical model cannot deal with this

event well. The numerical result is just a sample of the estimation for the best artificial heating interval by the numerical model introduced in Chapter 5.

6.5. Summary and Conclusion

In this chapter the relation between the features of IARs at high latitudes and Σ_W / Σ_P at the bottom boundary was investigated based on the numerical model introduced in Chapter 5. Particularly, the relation between Σ_W / Σ_P and the IAR eigenfrequencies and the relation between Σ_W / Σ_P and the spatial structures of the Alfvénic electric field were focused on. The best time intervals of ionospheric heating experiments to stimulate artificial IARs were estimated based on the numerical computation. The artificial heating experiment on 08/10/98 was taken for example for the time interval estimation.

According to the study, the eigenfrequencies of IARs are affected by the bottom boundary conditions of the ionospheric Alfvén resonance cavity, particularly the ratio between the Alfvénic wave conductivity and the height integrated Pedersen conductivity in the E region, which is the bottom boundary of the IAR. The value of Σ_W / Σ_P is in the range of 0.1 to 10. According to the numerical study in this chapter, the eigenfrequencies of IARs when Σ_W / Σ_P=0.1 are different from the eigenfrequencies when Σ_W / Σ_P=1 or 10. However, the eigenfrequencies when Σ_W / Σ_P=1 are same as the condition when Σ_W / Σ_P=10. In such a case, the eigenfrequencies detected by ground based pulsation magnetometers are affected by not only the structure of the Alfvénic resonance cavity but also the bottom boundary condition, particularly the ratio between the Alfvénic wave conductivity and the height integrated Pedersen conductivity at the bottom.

The theoretical study by numerical computation revealed that the eigenfrequencies observed by satellites could be different from those detected on the ground by pulsation magnetometers for an individual IAR event. Also, the signal intensities of resonance frequencies strongly depend on the values of Σ_W / Σ_P.

Chapter 7. Plasma Density Perturbation and IAR Eigenfrequency Shifts

7.1. Introduction

In Chapter 3, it has been discussed that the eigenfrequencies of IARs could change frequently and intensively. An example was shown in Chapter 3 (Section 3.6 and Fig 3.16). According to the analysis and the discussion in Chapter 3, the IAR eigenfrequency variations were dominated by variations and perturbations of the ionospheric plasma density. Previous studies [Prikner et al, 2007] revealed that there could be intensive plasma density perturbations, and the plasma density perturbations changed the exponential plasma density profile above the F2 peak. Fig 7.1 illustrates an example of plasma density perturbation above the F2 peak. The ionospheric plasma density data plotted in Fig 7.1 was obtained by EISCAT Tromsø radar on 7 Mar 2001 when the radar system was working in CP1 and CP7 modes. The altitude range extended up to 2300km. Ideally the plasma density profile above the F2 peak should be an exponential function. However, clear and intensive density perturbations can be seen above the F2 peak in Fig 7.1. It should be noticed that the axis are logarithmic. The Alfvénic wavelengths in the region of a plasma density perturbation are different from their original status. Thus the effective size of the resonance cavity changes due to the existence of the perturbation, which leads to variations of IAR eigenfrequencies. Based on the profiles shown in Fig 7.1 Prikner et al investigated the expected eigenfrequencies of the IAR numerically, and then compared the numerical results with data. In Chapter

3, an example of non-uniform eigenfrequency distribution was shown. In practice this phenomenon appears quite frequently, thus it is necessary to investigate how the plasma density perturbations affect the eigenfrequency distributions in more details. In Chapter 5, the results of the numerical computation and the observed eigenfrequencies of 18 UT 04/10/98 were compared, and they match quite well. In this chapter, the eigenfrequencies of the IAR will be further investigated based on the same Alfvén velocity profile using the method (but different model) similar to Prikner's.

In the modelling which follows, some of the parameters of the numerical computation were fixed. Those parameters are listed in Table 7.1. All the units of the calculated variables based on the numerical model were arbitrary in this chapter because they had been rescaled. However, the real value of the calculated variables can be estimated based on the ratio of the rescaling. The unit of length in the numerical study was the kilometre, and the spatial grid sizes were set to be 1km in most of the numerical computations.

7.2. Eigenfrequency Shifts Respond to Density Perturbations

Plasma density perturbations below the F2 peak could be monitored easily by ionosondes or incoherent scatter radar systems. In other words, the IAR eigenfrequency shifts can be investigated in detail based on observations and data interpretations. However, there are not too many incoherent scatter radar systems over the whole world. The plasma density profile could be monitored continuously just by incoherent scatter radars. Thus the study in this chapter would focus on the density perturbations above the F2 peak. The study aimed at qualitatively investigating the relations between plasma density perturbations above the F2 peak and the IAR eigenfrequency shifts. Furthermore, the study investigated that whether it is possible to roughly estimate the plasma density perturbations above the F2 peak according to the IAR eigenfrequency shifts observed by pulsation magnetometers on the ground.

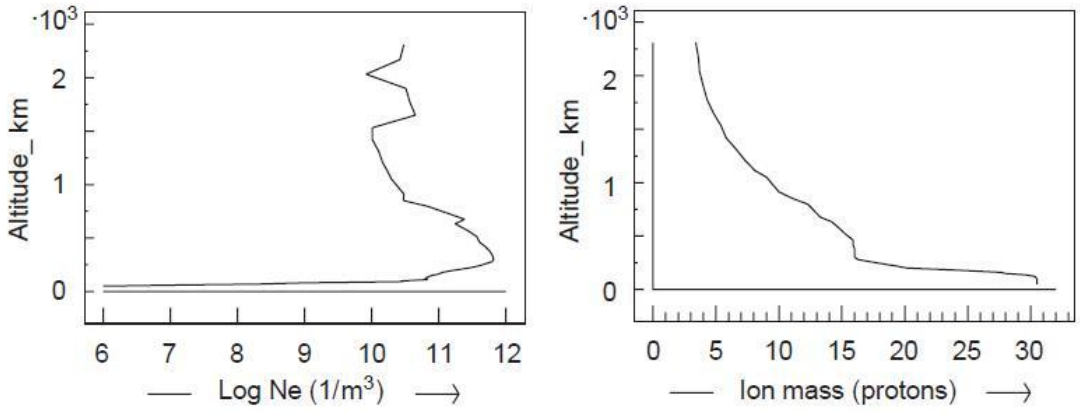

Fig 7.1 The plasma density profile and the average mass profile obtained by EISCAT Tromsø radar on 7 Mar 2001 [Prikner et al, 2007]. The figure illustrates an example of density perturbations above the F2 peak.

Altitude of E peak	$H_{E_{\max}} = 110km$(fixed according to IRI2007)
Range of angular frequency	$\omega \in [0.10,40] rad/s$
Angular frequency resolution	$\Delta\omega = 0.10 (\Delta f \approx 0.0159 Hz)$
Source Electric Field	$E_b = 1$
Source current	$J_S = E_b \Sigma_P \delta(z - H_{E_{\max}})$
Vacuum permeability	$\mu_0 = 4\pi \times 10^{-7} H/m$

Table 7.1 Fixed parameters for the numerical study.

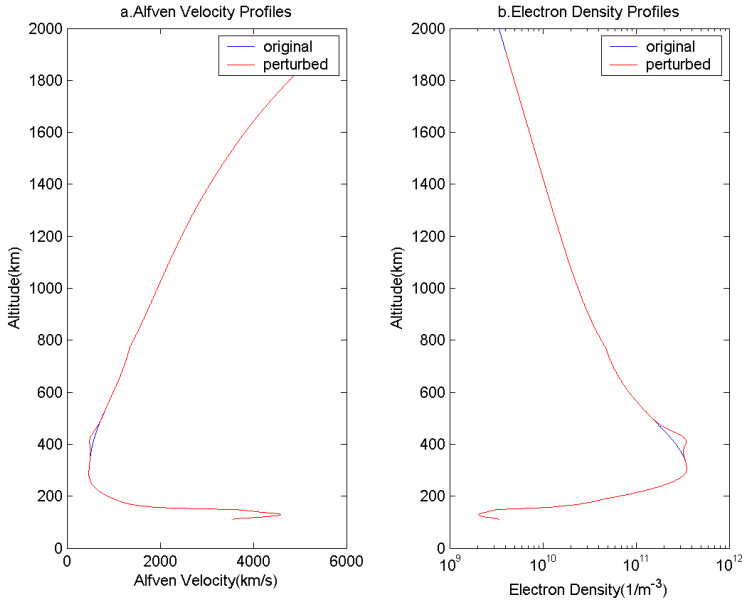

Fig 7.2 The blue line in panel a illustrates the Alfvén velocity profiles of 18 UT, 04/10/98 at Sodankylä. The profile was generated by IRI2007. The red line illustrates the perturbed Alfvén velocity profile. The perturbation is centred at 425km. Panel b illustrates the corresponding electron density profiles. The blue line and the red line in panel b illustrate the original and perturbed profiles, respectively. The x-axis of panel b is logarithmic.

In order to investigate how the density perturbations above the F2 peak impact the eigenfrequencies of the IAR, the model introduced in chapter 5 was utilized. The data utilized as the non-perturbed profile was the Alfvén velocity profile of 18UT on 4 Oct 1998 in Sodankylä, which was generated by IRI2007. The altitude of the F2 peak was 292km in the profile. The altitude of the E peak was automatically fixed at 110km by IRI2007, and it can be seen in Table 7.1. Different types of density perturbations would be set based on the non-perturbed profile.

The density perturbations in this chapter were set directly on the Alfvén velocity profiles. All the perturbations were set to be Gaussian functions as equation 7.1.

$$\Delta V_A = a V_A|_{z=h_0} \exp\left(\frac{-(z-h)^2}{b}\right) \qquad (7.1)$$

where ΔV_A is the Alfvén velocity perturbation, a and b are constants, $V_A|_{z=h_0}$ is the non-perturbed Alfvén velocity at the altitude of h_0, z is the variable of altitude, h is the altitude of the centre of the perturbation. Normally h_0 was selected to be the altitude of the F2 peak, which was 292km. The value of a was normally selected to be smaller than or equal to 0.3. The percentage of each species of ions in this chapter was supposed to be constant. In such a case the perturbations on the Alfvén velocity profile were simply caused by plasma density perturbations.

In chapter 6 the boundary condition dependence of IARs was investigated numerically based on the same numerical model. Particularly, it was found that the IAR eigenfrequencies depend on Σ_W / Σ_P , where Σ_W is the Alfvénic wave conductivity at the E peak, and Σ_P is the height integrated Pedersen conductivity of the E layer. The value of Σ_W / Σ_P varies in the range of 0.1 to 10 during a single day [Belyaev et al, 1990]. Thus in this chapter, every individual plasma density perturbations will be investigated based on the condition of Σ_W / Σ_P=0.1, 1 and 10, separately. Fig 7.2 and Fig 7.3 show an example of IAR eigenfrequency shifts in different boundary conditions. Fig 7.2 illustrates the original and perturbed Alfvén velocity and electron density profiles. The blue line and the red line in panel a illustrate the non-perturbed and

perturbed Alfvén velocity profiles, respectively. Panel b illustrates the corresponding non-perturbed and perturbed density profiles. The perturbation is a density enhancement, which is centred at 425km. The maximum of the perturbation, which is at the centre, is 30% of the Alfvén velocity at the F2 peak. Thus it is 316km above the F2 peak. Fig 7.3 illustrates the total current intensities at the E peak. In panel a, b and c the blue lines and the red lines illustrate the total current intensities of non-perturbed and perturbed profiles, respectively. Σ_W / Σ_P equals to 0.1, 1 and 10 in panel a, b and c, respectively. In Fig 7.3 it can be seen that although the values of Σ_W / Σ_P are different in the three panels, the peaks and troughs of the perturbed total current intensities shifts towards low frequency bands referring to the non-perturbed total current intensities. It indicates that the plasma density perturbations could impact the peaks and troughs of the signals detected by pulsation magnetometers on the ground, regardless of the value of Σ_W / Σ_P.

Moreover, Fig 7.4 illustrates the spatial structures of the differences between the electric field intensities of perturbed and non-perturbed profiles. The scales of the differences can be seen to the right of each panel. The value of Σ_W / Σ_P for panel a, b and c are 0.1, 1 and 10, respectively. The differences are the responses on the electric field caused by the plasma density perturbation. In Fig 7.4 it can be see that the differences are distributed over the whole space of the resonance cavity. The differences could lead to eigenfrequency shifts in observations, particularly by satellites. Thus it indicates that the IAR eigenfrequency shifts can be observed by not only the pulsation magnetometers on the ground but also the satellites which are at proper positions. According to the study on the boundary condition dependence of the IAR eigenfrequencies and spatial field structures, the eigenfrequency shifts observed simultaneously by ground magnetometers and satellites could be different. However, in this chapter, the study on the eigenfrequency shifts respond to plasma density perturbations will mainly focus on ground observations, thus the in-situ observations and the comparison with the simultaneous ground observations will not be investigated in more details in this chapter. It would be a future task.

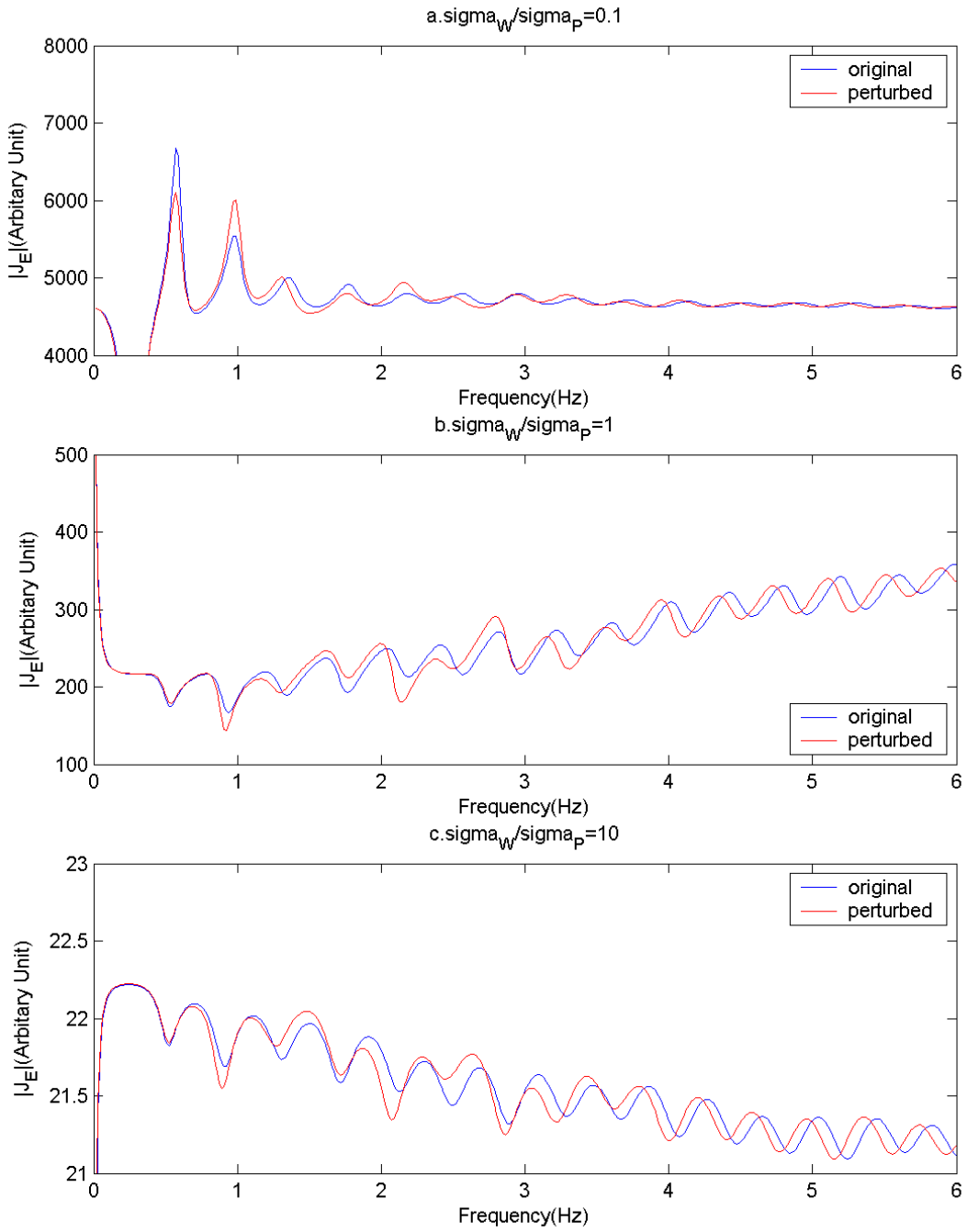

Fig 7.3 The figure illustrates the total current intensities at the E peak. The blue lines and red lines illustrate the current intensities of original and perturbed profiles, respectively. In panel a, b and c, Σ_W / Σ_P equals to 0.1, 1 and 10, respectively.

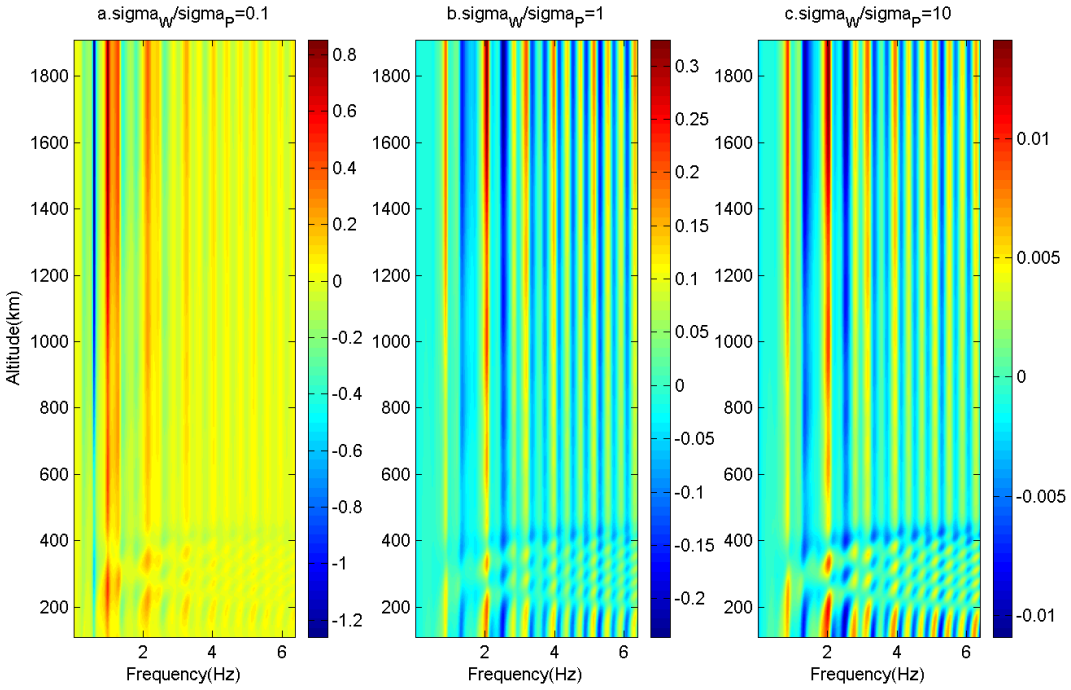

Fig 7.4 The differences between the perturbed and the original electric field intensities are illustrated. The x-axes are frequency axes; the y-axes are altitudes, which cover the range from 110km to 1910km. In panel a, b and c Σ_W / Σ_P equals to 0.1, 1 and 10, respectively.

There could be both plasma density depletion and enhancement above the F2 peak due to particle precipitations, vertical motions of plasma or instabilities at high altitudes. Fig 7.5 illustrates the comparison between the plasma density depletion and the plasma density enhancement. The absolute values of the perturbations are equivalent and centred at 475km. The intensities of the perturbations were 20% of the minimum Alfvén velocity of the non-perturbed profile over the whole space of the resonance cavity. The upper panel and the lower panel show the response of the Pedersen current to density depletion and enhancement, respectively. Blue lines and red lines demonstrate the Pedersen current at the E peak without any perturbation and with perturbation, respectively. By comparing the red line with the blue line in each panel, it can be seen that the density depletion and the density enhancement above the F2 peak shift the eigenfrequencies in different ways. For example, in the upper panel, the sixth eigenfrequency of the red line is higher than the blue line; in the lower panel, the sixth eigenfrequency of the red line is lower than the blue line. That implies that density depletions and density enhancements above the F2 peak shift the eigenfrequencies towards different bands. Density depletions shift the eigenfrequencies towards higher bands. Density enhancements shift the eigenfrequencies towards lower bands.

Fig 7.6 illustrates two different plasma density perturbations, which were based on the original plasma density profile. The responses of the intensity of the electric field and the total current intensity at the E peak were shown in the figure. The plasma density perturbations of different intensities are shown in panel a. The perturbations were set based on equation 7.1. The blue line and the red line represent the perturbations of a=0.3 and a=0.1, respectively. That means the maximums of the perturbations shown in panel a are 30% and 10% of the Alfvén velocity at the F2 peak of the original Alfvén velocity profile, respectively. Both of the two perturbations centred at the altitude of 425km, which is 34km above the F2 peak. Referring to the left panel of Fig 6.1, the density perturbations shown in Fig 7.6 are relatively weak. Panel b, c and d show the responses of the total current intensities at the E peak to the density perturbations shown in panel a. The intensity of the magnetic pulsation signals observed by pulsation magnetometers on the ground is proportional to the Pedersen current intensity in the E region. Also, in this numerical study the source oscillation field was set to be constant and renormalized to be 1. Thus the structure of the IAR oscillations detected on the

ground should be dominated by the oscillating Pedersen current structure. Panel b, c and d correspond to the boundary conditions of Σ_W / Σ_P=0.1, 1 and 10, respectively. The black lines, the blue lines and the red lines denote the total current intensities without perturbation, with the perturbation of a=0.3 and the perturbation of a=0.1, respectively. Comparing the three panels, it can be seen that the eigenfrequencies of the IAR shifted due to the density perturbations. Generally the eigenfrequencies were shifted towards lower frequency bands in all of the three panels. More intensive density perturbations have greater impact on the eigenfrequency shifts regardless of the value of Σ_W / Σ_P. It indicates that the IAR eigenfrequency shifts are sensitive to the intensities of the plasma density perturbations above the F2 peak.

Also, when density perturbations of the same intensity occurred above the F2 peak centred at different altitudes, the responses of the Pedersen current were also different. The results of different values of Σ_W / Σ_P were shown in Fig 7.7, Fig 7.8 and Fig 7.9, respectively. The effective size of the resonance cavities is 1800km. The perturbations, which were 20% of the Alfvén velocity at the F2 peak, were set on the Alfvén velocity profile. In the three figures, from panel a to panel c, the centre altitudes of the perturbations were 375km, 525km and 675km, respectively. The altitude differences are 150km. The blue lines and red lines illustrate the Pedersen current without and with perturbations, respectively. It can be seen that when the altitude of the density perturbation is higher, the shifts of the eigenfrequencies start at higher frequency bands. For example, the eigenfrequency shifts started on the first peak in panel a of Fig 7.7, while they started on the third peak in panel c. And the eigenfrequency shifts are similar in Fig 7.8 and Fig 7.9. Those indicate that plasma density perturbations at different altitudes lead to different eigenfrequency shifts. Perturbations at higher altitudes shift eigenfrequencies at higher frequency bands, and vice versa. However, the difference of the centre altitudes of the perturbations in panel c and panel a is 300km, and the differences on the eigenfrequency shifts are slightly greater than 1Hz. That indicates the eigenfrequency shifts are not very sensitive to the centre altitude of density perturbations above the F2 peak.

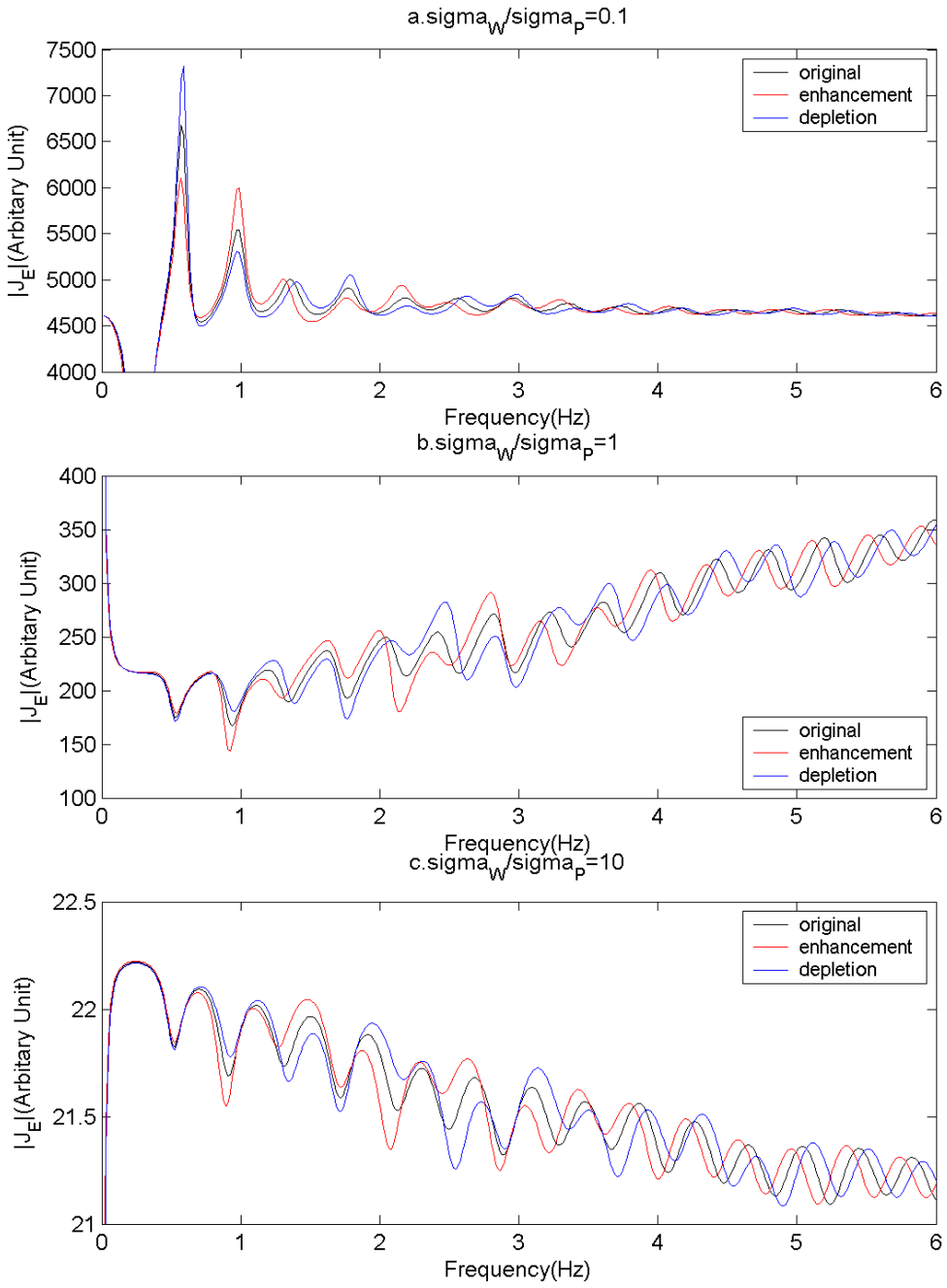

Fig 7.5 The perturbation on the Alfvén velocity profile is centred at 425km. The maximum of the perturbation is 20% of the Alfvén velocity at the F2 peak. Panel a, b and c illustrate the total current intensities at the E peak while Σ_W / Σ_P equals to 0.1, 1 and 10, respectively. The black lines illustrate the current intensities without perturbation; the red lines illustrate the current intensities with plasma density enhancements; the blue lines illustrate the current intensities with plasma density depletions.

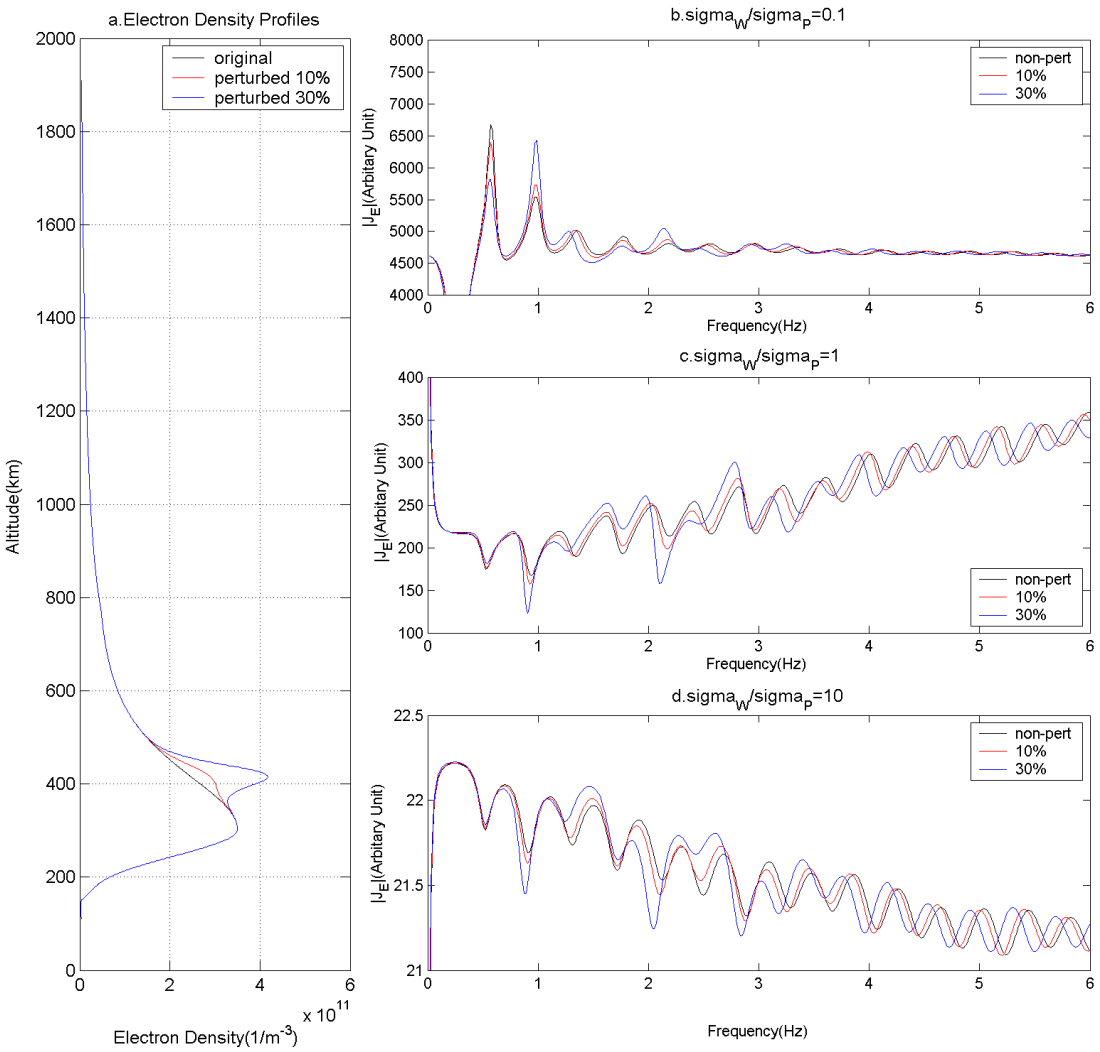

Fig 7.6 The non-perturbed and perturbed electron density profiles are illustrated in panel a. The black line is the non-perturbed profile; the red line is the weakly perturbed profile; the blue line is the strongly perturbed profile. The total current intensities at the E peak are illustrated in panel b, c and d. The values of Σ_W / Σ_P in panel a, b and c are 0.1, 1 and 10, respectively.

The widths of all the density perturbations utilized above were fixed. Thus it is worth seeing that how the width of density perturbations influence the eigenfrequencies of the IAR. Fig 7.10 illustrates the density perturbations of different widths. The perturbations were centred at 375km. The perturbations were set on the Alfvén velocity profiles in the form which is shown in equation 7.1. The maximum intensities of the perturbations are 30% of the Alfvén velocity at the F2 peak. According to equation 7.1, different values of b lead to different widths of perturbations. The blue lines illustrate the original Alfvén velocity profiles, and the red lines illustrate the perturbed profiles. Vpmax is the maximum of the perturbation; $V_A(183)$ is the Alfvén velocity at the F2 peak. The effective size set for the computations is 1800km, which covers the altitudes of the range from 110km to 1910km. However, in order to show the perturbations more clearly, the scale of the y-axes in Fig 7.10 is just 1200km. There are not any perturbations above the altitude of 1200km, thus the Alfvén velocity profiles above this altitude are not shown in Fig 7.10. The range of the altitudes of the narrowest perturbation, which is shown in panel a, covers about 70km, while the broadest perturbation shown in panel c covers about 120km, which is almost two times of the narrowest.

Fig 7.11, Fig 7.12 and Fig 7.13 show the total current intensities at the E peak respond to the perturbations shown in Fig 7.10. Σ_W / Σ_P=0.1, 1 and 10 in Fig 7.11, Fig 7.12 and Fig 7.13, respectively. In each figure, panel a illustrates the original (without perturbation) and the perturbed current intensities. Panel b illustrates the comparison between different widths of perturbations which corresponding to b=600 and b=1200. Panel c illustrates the comparison between different widths of perturbations which corresponding to b=600 and b=2200. Similar features of the eigenfrequency shifts can be seen in these three figures. Take Fig 7.12 for example, clear variations of eigenfrequency shifts and current intensities can be seen in panel a. In the frequency band between the two green lines in panel a, the current intensities with the perturbation increase intensively. For the red line, there are three peaks in this band. However, the source current in this computation was a constant for all the components of frequencies, and in realistic cases, the source current is not a constant, it varies with frequency. That indicate in realistic cases, the three peaks could look like a single peak, which means the separations of the eigenfrequencies could be strongly non-uniform, some of the

separations could be several times of the others due to the merge of several peaks or troughs. In panel c, it can be seen that the merge of the peaks on the blue line between the green lines is much clearer than on the red line. The merge of the peaks is almost invisible in the same band. In panel b, the features of the merge of peaks are similar on the red and blue lines in relatively lower frequency band in the band that higher than 2.5Hz. However, the features of the merges on the red line are not quite clear compare to the blue line. According to Fig 7.10, the perturbation corresponding to the red line is much broader than the perturbation corresponding to the blue line. That indicates the trough between two peaks could disappear, and one of the two peaks becomes indistinguishable. The harmonic structure of the peaks and the trough disappear and merge with the adjacent harmonic structure. Narrower perturbations lead to clearer merges.

7.3. Summaries and Conclusions

Plasma density perturbations were set on the non-perturbed Alfvén velocity profiles above the F2 peak in order to investigate the relationship between plasma density perturbations above the F2 peak and the IAR eigenfrequency shifts. The numerical studies in this chapter are based on the numerical model introduced in Chapter 5. Ideally the plasma density profile above the F2 peak of the ionosphere should be an exponential function. However, there could be plasma density perturbations above the F2 peak. Fig 7.1 shows an example of such perturbations. When there is density perturbation above the F2 peak of the ionosphere, the perturbation can influence the Pedersen current at the E peak, which leads to the impacts on the signals detected by pulsation magnetometers on the ground. Also, the numerical study shows that the eigenfrequency shifts led by plasma density perturbations could be detected by in-situ observations above the bottom boundary of the IAR. However, it was not investigated in details in this chapter. The study in this chapter mainly focused on the impacts that could be observed by pulsation magnetometers on the ground.

The non-perturbed Alfvén velocity profile utilized in this study is the profile of 18 UT, 04/10/98 generated by the IRI2007 model. In this study, some of the parameters were fixed. Those fixed parameters are listed in Table 7.1. It should be noticed that the altitude of the E peak was fixed automatically by the IRI2007 model.

According to the study, the eigenfrequency shifts respond different features of plasma density perturbations in different ways. Plasma density depletions shift the eigenfrequencies of the IAR towards high frequency bands. Density enhancements shift the eigenfrequencies towards low frequency bands. The eigenfrequency shifts are sensitive to the intensities of the plasma density perturbations. Stronger perturbations affect the eigenfrequencies more intensively. Plasma density perturbations at different altitudes lead to different eigenfrequency shifts. Perturbations at higher altitudes shift eigenfrequencies at higher frequency bands, and vice versa. Also, the differences of the widths of perturbations could lead to the merge of the peaks. Narrower perturbations lead to clearer merges. In realistic cases, it could lead to the situation that some of the observed eigenfrequency separations are several times of the other separations during a single time interval. However, according to the study, the eigenfrequency shifts are not quite sensitive to the altitudes and the size of the perturbations.

Therefore, probably the plasma density perturbations could roughly monitored continuously on the ground according to the eigenfrequency shifts observed by pulsation magnetometers. The study in this chapter is just the initial step. There are still a lot of difficulties, e.g., the intensity of the source current is unknown for a natural IAR event. In addition, this method is not quite sensitive to the altitudes and the size of the perturbations. It just shows very general and imprecise results of the perturbations. In addition, this chapter just shows the qualitative study. In order to roughly estimate the plasma density perturbations above the F2 peak based on the eigenfrequency shifts of the IARs observed on the ground, the relationship between density perturbations and eigenfrequency shifts need to be further investigated.

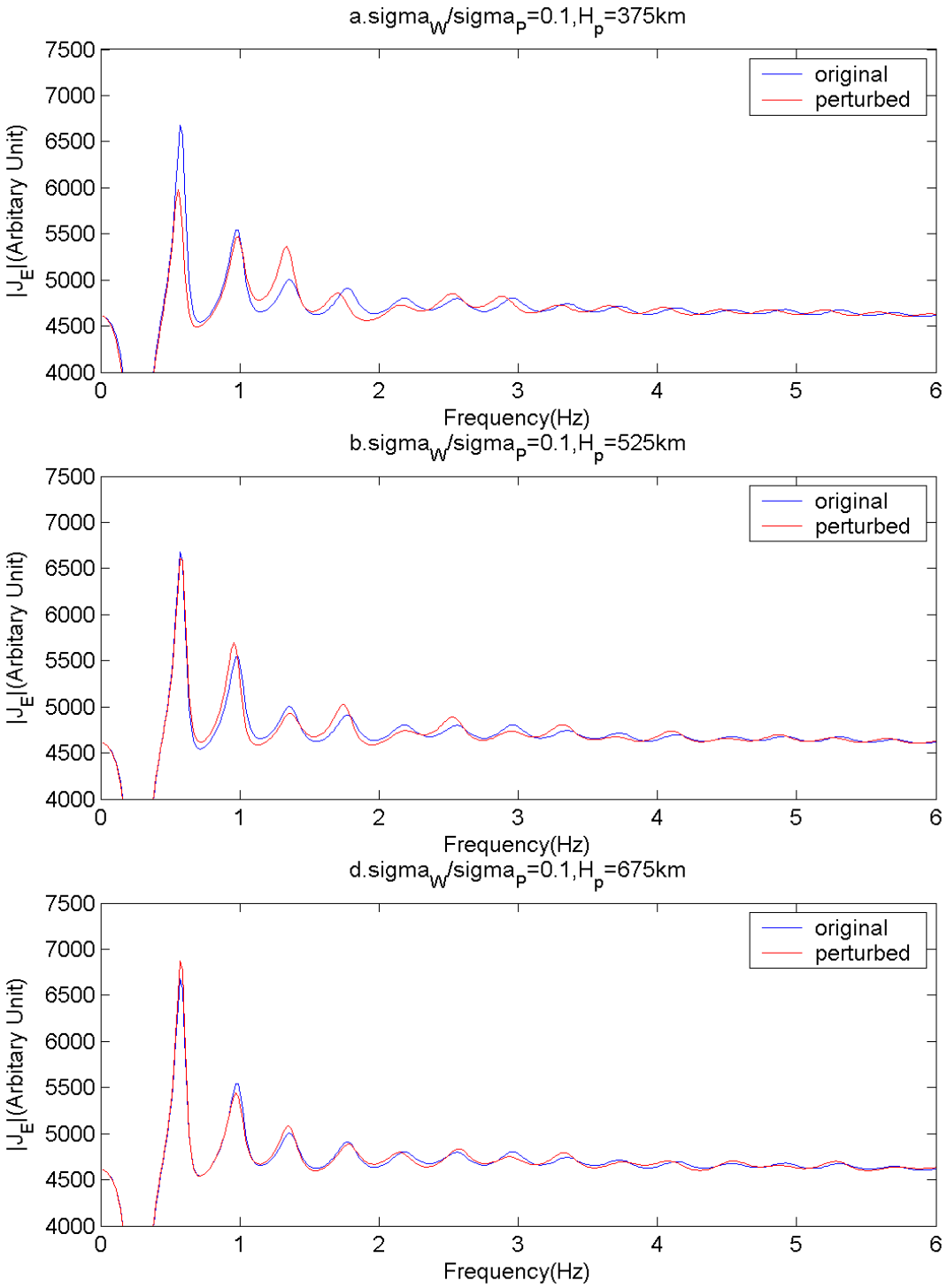

Fig 7.7 The figure illustrates the eigenfrequency shifts respond to the plasma density perturbations at different altitudes. The blue lines and the red lines are total current intensities at the E peak without and with perturbations, respectively. Σ_W / Σ_P equals to 0.1.

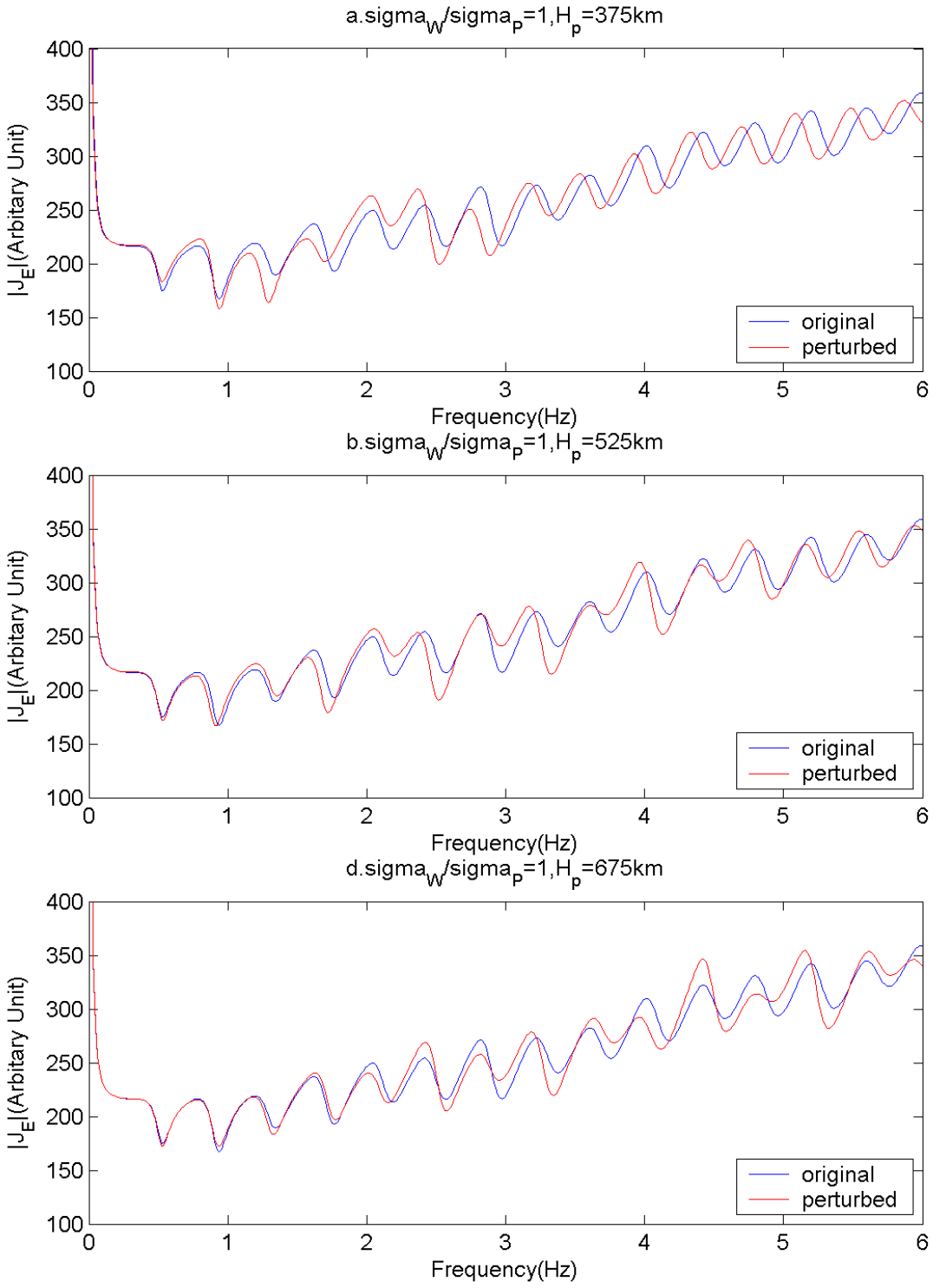

Fig 7.8 The figure illustrates the eigenfrequency shifts respond to the plasma density perturbations at different altitudes. The blue lines and the red lines are total current intensities at the E peak without and with perturbations, respectively. Σ_W / Σ_P equals to 1.

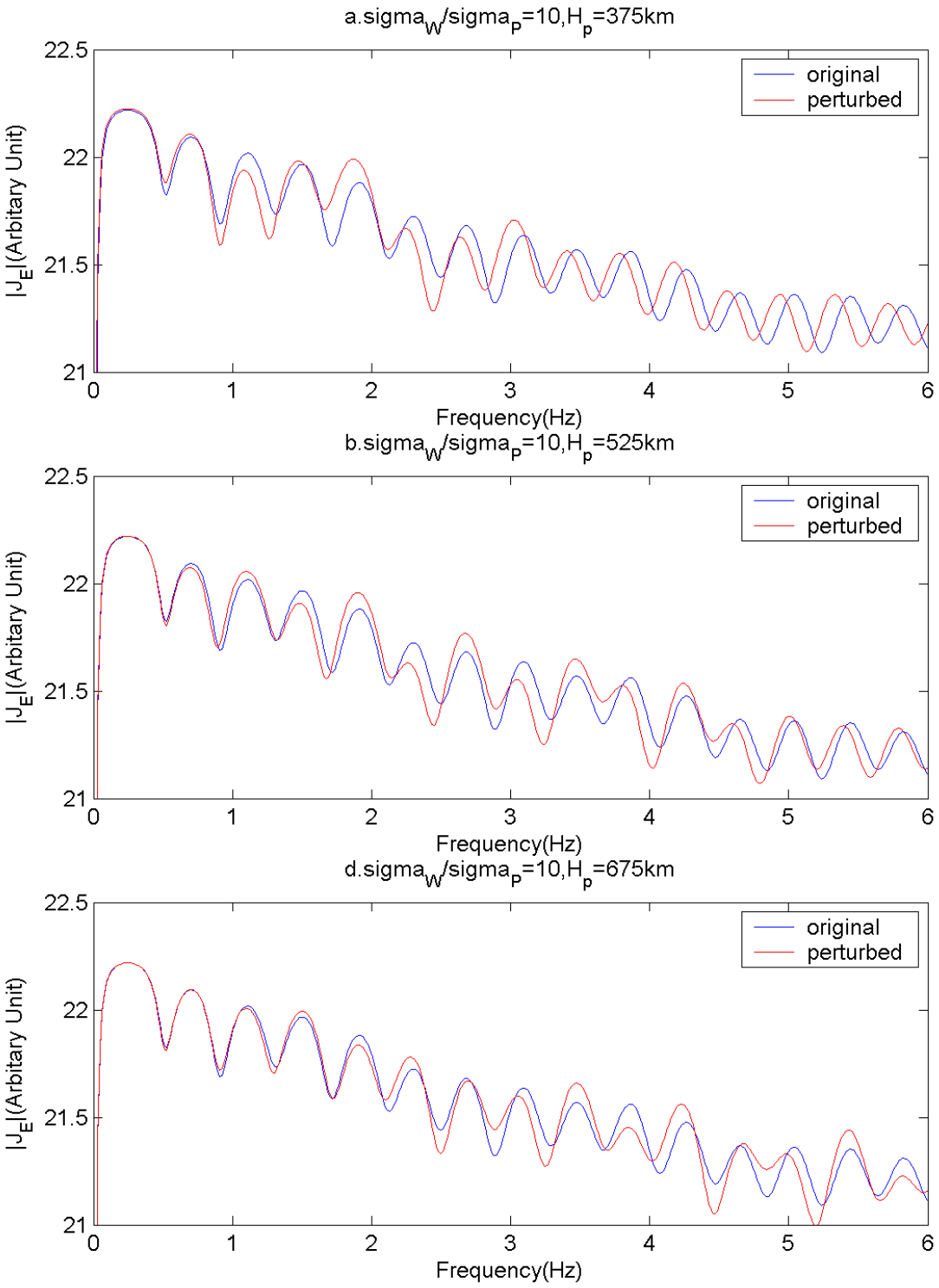

Fig 7.9 The figure illustrates the eigenfrequency shifts respond to the plasma density perturbations at different altitudes. The blue lines and the red lines are total current intensities at the E peak without and with perturbations, respectively. Σ_W / Σ_P equals to 10.

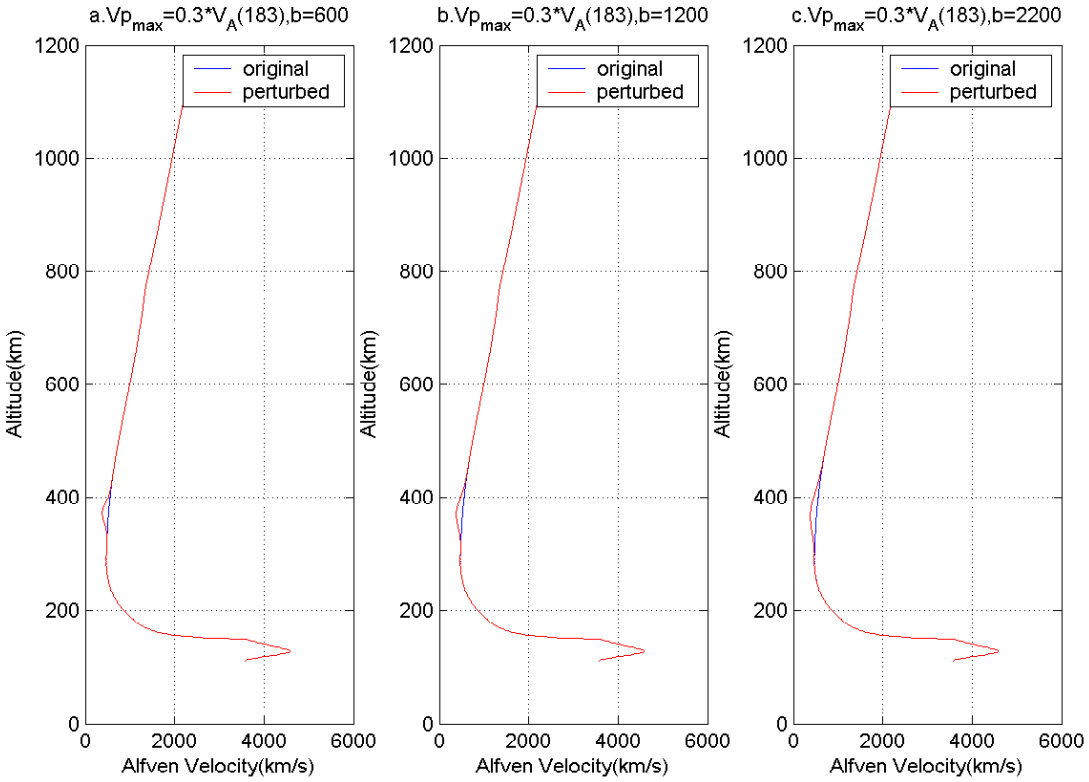

Fig 7.10 The figure illustrates the different widths of perturbations. The blue lines are the non-perturbed profiles; the red lines are the perturbed profiles. Vp_{max} is the maximum of the perturbation. $V_A(183)$ is the Alfvén velocity at the F2 peak. The maximums of the perturbations are same, which are 30% of the Alfvén velocities at the F2 peak. The perturbations were set according to equation 7.1. Different values of b lead to different widths of perturbations.

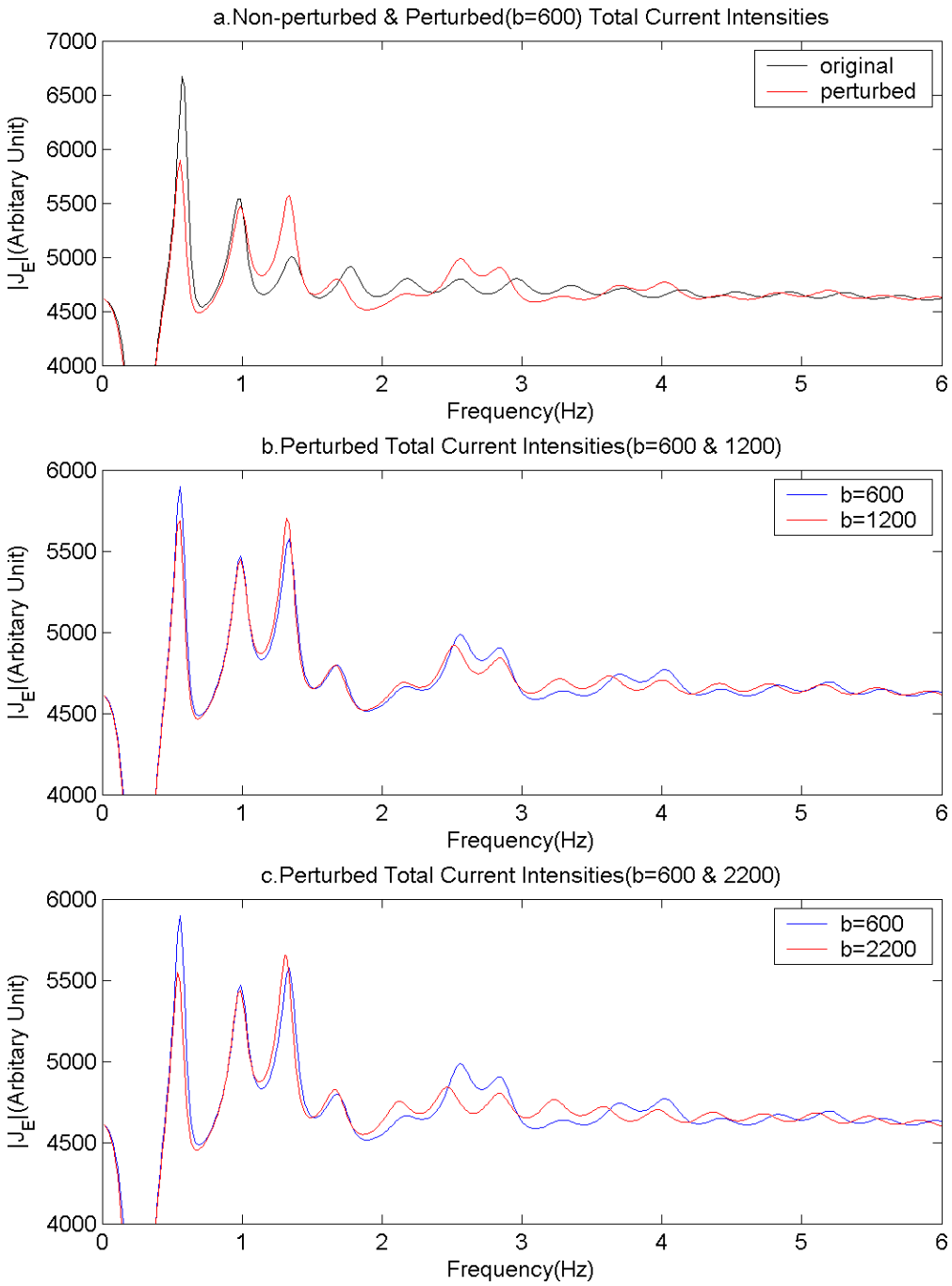

Fig 7.11 The figure shows the total current intensities at the E peak respond to the perturbations shown in Fig 7.10. Σ_W / Σ_P=0.1. Panel a illustrates the original (without perturbation) and the perturbed current intensities. Panel b illustrates the comparison between different widths of perturbations which corresponding to b=600 and b=1200. Panel c illustrates the comparison between different widths of perturbations which corresponding to b=600 and b=2200.

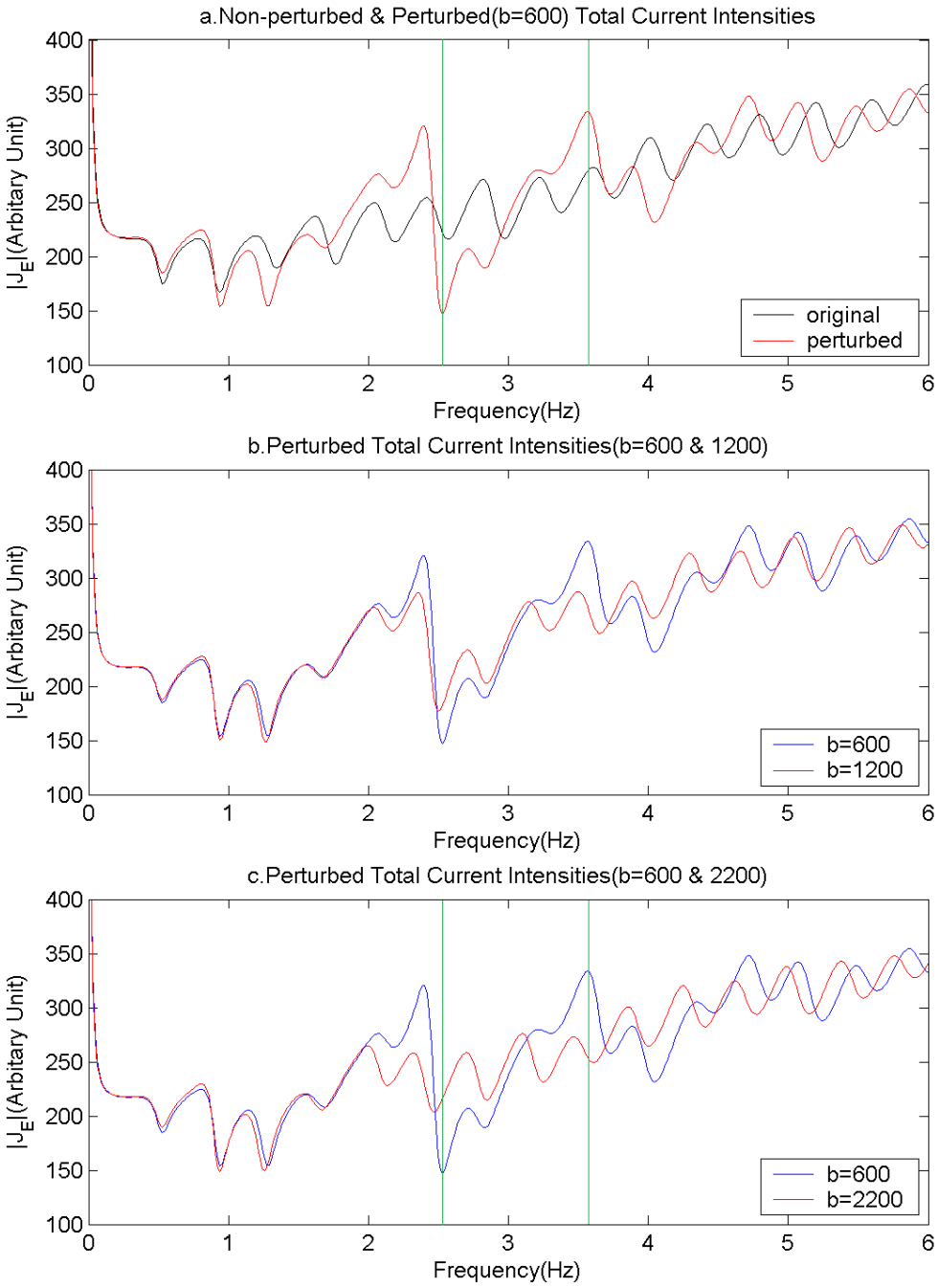

Fig 7.12 The figure shows the total current intensities at the E peak respond to the perturbations shown in Fig 7.10. Σ_W / Σ_P=0.1. Panel a illustrates the original (without perturbation) and the perturbed current intensities. Panel b illustrates the comparison between different widths of perturbations which corresponding to b=600 and b=1200. Panel c illustrates the comparison between different widths of perturbations which corresponding to b=600 and b=2200.

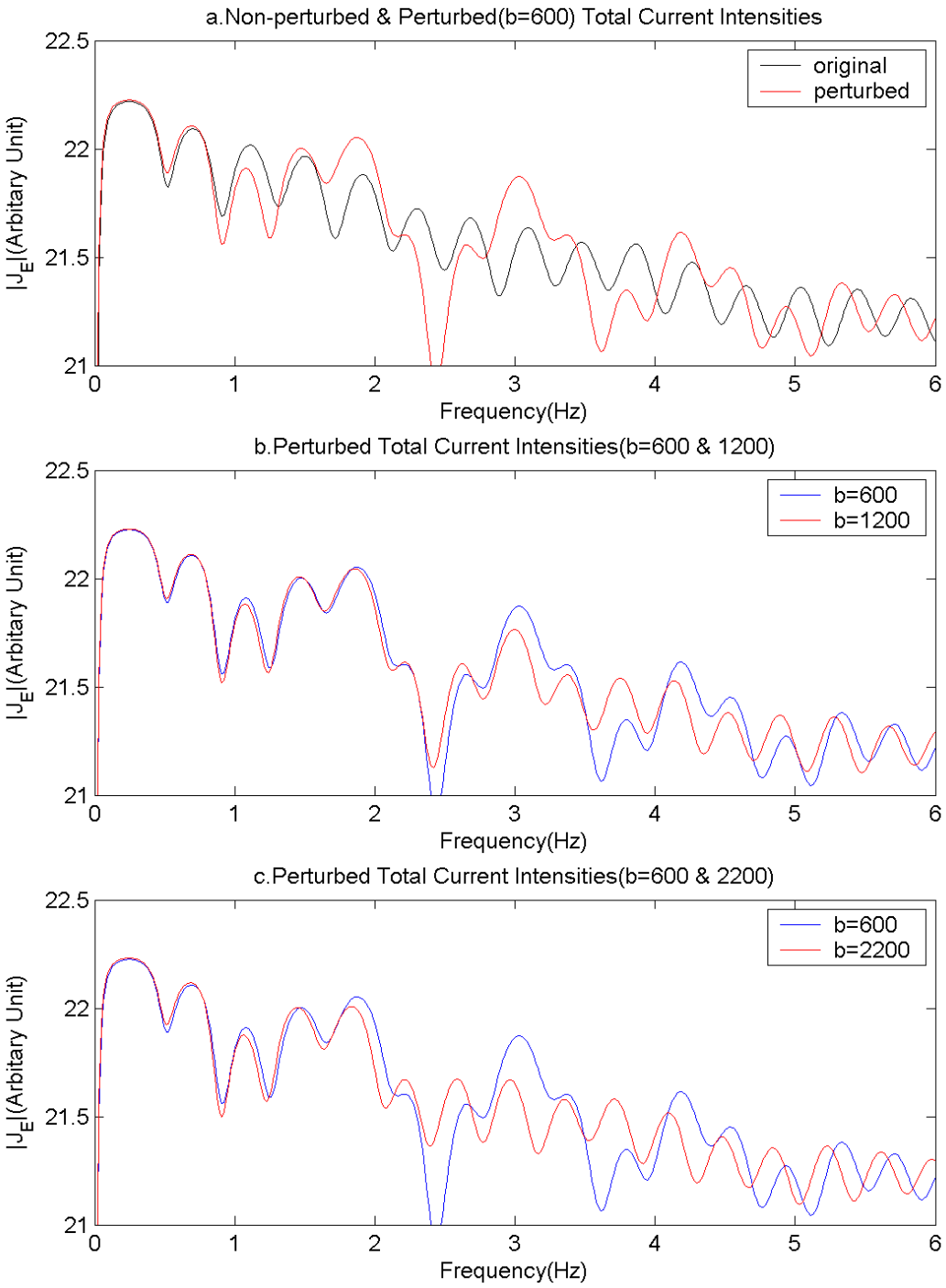

Fig 7.13 The figure shows the total current intensities at the E peak respond to the perturbations shown in Fig 7.10. Σ_W / Σ_P=0.1. Panel a illustrates the original (without perturbation) and the perturbed current intensities. Panel b illustrates the comparison between different widths of perturbations which corresponding to b=600 and b=1200. Panel c illustrates the comparison between different widths of perturbations which corresponding to b=600 and b=2200.

Chapter 8. Summary and Future Works

8.1. Summary of the Results

In this thesis, the Ionospheric Alfvén Resonator has been studied both theoretically and experimentally. 13 IAR events were observed in October 1998 at Sodankylä. Four of those were selected to be analysed. The dates of the four events are 04/10/98, 05/10/98, 14/10/98 and 30/10/98, respectively, which cover the beginning, the middle and the end of the October. For all of those events, the period of 16UT to 19UT was the common interval that IARs existed. The double running average and the sinusoidal curve fitting methods were utilized to find the eigenfrequency separations of the events. By investigating the eigenfrequency separations of the five IAR events, it is found that the IAR eigenfrequencies increase in the afternoon generally. However, there are fluctuations on the eigenfrequencies. On 14/10/98, the eigenfrequency separations increased for around 60% in 17:45:00UT to 18:00:00UT. For all of those events, the eigenfrequency separations could fluctuate in less than 10 minutes.

In addition, on 09/11/02, a single IAR event was observed by 5 Finnish pulsation magnetometers simultaneously. It was found that the eigenfrequency separations are different at different locations. Also, the eigenfrequency separations fluctuated. The fluctuation could lead to the invisibility of SRS structures on dynamic spectra. According to the dynamic spectra of the five events, the threshold of the rate of eigenfrequency separation fluctuation is between 0.020Hz/min and 0.025Hz/min, i.e.,

the SRS would be invisible when the fluctuation of eigenfrequency separations is higher than 0.025Hz/min though there is IAR detected. Weaker fluctuations make the SRS more visible.

For the events observed in October 1998 studied in this chapter, the results implied that the ionospheric plasma density at high latitudes could change by 30% in 10 minutes. Additionally, the scale of the horizontal ionospheric plasma density structure is smaller than 200km at high latitudes. On the other hand, the scale of the nonuniformity of ionospheric plasma density structure in 1000km above the E peak at high latitudes is less than 200km according to the data analysis in Chapter 3.

All the previous studies on IARs at high latitudes are in northern hemisphere. In this thesis, the statistical study on IAR in Antarctica was carried out. The data obtained at Halley Bay in the period of 2005 to 2009 was surveyed. The period covers five years including a solar minimum which is in 2008. There were 37 IAR events observed based in SRS signals in dynamic spectra in total. According to the study, more than 95% (35/37) of all the IAR events occurred in one month prior or after equinoxes. There are two gaps for the IAR occurrence in a whole year in 2005 to 2009, which are November to January and May to August, respectively. The instrument upgrade was not taken into account in this study. The data coverage rate of the surveyed data of the whole period is 96.28%, which is relatively high. The IAR occurrence after spring equinoxes and prior to autumn equinoxes is higher than the other two periods. The IAR occurrence reached the maximum in 2009, which has passed the solar minimum in 2008. That indicates that the IAR occurrence is not simply dominated by solar activities but also some other factors. According to the study by Trakhtengerts et al [2000b], the IAR occurrence is anti-correlated to the solar activity. However, all the previous studies about the IAR occurrences just investigated the IARs in northern hemisphere. In this study it revealed that the solar activity dominates the IAR occurrence in Antarctica. However, considering that the IAR is basically controlled by the ionospheric conditions directly, which is dominated by not only the solar activity but also some local factors, it is obvious that local factors which could influence the ionospheric conditions also make contribution to the IAR occurrence.

In addition, according to the statistical study of the directions of magnetic field vector measured by the pulsation magnetometer in Halley Bay Station and the field intensity variations of the IAR in chapter 3, the oscillation source of the IAR could be the noise of the electromagnetic field pulsations in the ionosphere. Moreover, there are always the resonance cavity structures of IARs in the ionosphere, thus there should be a threshold for the noise intensity to excite IARs.

For the numerical study in this thesis, a model was introduced and tested in Chapter 5. By comparing the numerical results of this model and other analytical models, and comparing the simulation results with observed data, the model could be utilized to simulate the eigenfrequencies of the IAR.

According to the study in Chapter 6, the eigenfrequencies of IARs significantly depend on the bottom boundary conditions of the resonance cavity. The ratio between the Alfvénic wave conductivity and the height integrated Pedersen conductivity in the E region has significant impacts on the eigenfrequencies of IARs. The ratio between the Alfvénic wave conductivity and the height integrated Pedersen conductivity is in the range between 0.1 and 10. In addition, the eigenfrequencies of Σ_W / Σ_P =0.1 is different from Σ_W / Σ_P =1 or 10. However, the eigenfrequencies of Σ_W / Σ_P =1 are same to Σ_W / Σ_P =10. In such a case, the eigenfrequencies observed by pulsation magnetometers depend on not only the structure of the Alfvénic resonance cavity but also the bottom boundary condition, particularly the ratio between the Alfvénic wave conductivity and the height integrated Pedersen conductivity. There are also in-situ observations on IARs by space crafts. The theoretical study by numerical computation revealed that the eigenfrequencies observed by satellites could be different from those detected on the ground by pulsation magnetometers for an individual IAR event. Also, the signal intensities of resonance frequencies strongly depend on the values of Σ_W / Σ_P.

According to the numerical study in Chapter 7, when there is density perturbation above the F2 peak of the ionosphere, the perturbation can influence the Pedersen current at the E peak, which leads to the impacts on the signals detected by pulsation magnetometers on the ground. The eigenfrequency shifts respond to different features of plasma density perturbations in different ways. Plasma density depletions shift the eigenfrequencies of the IAR towards high frequency bands. Density enhancements shift the eigenfrequencies towards low frequency bands. The eigenfrequency shifts are sensitive to the intensities of the plasma density perturbations. Stronger perturbations affect the eigenfrequencies more intensively. Furthermore, plasma density perturbations at different altitudes lead to different eigenfrequency shifts. Perturbations at higher altitudes shift eigenfrequencies at higher frequency bands, and vice versa. Also, the differences of the widths of perturbations could lead to the joint of the peaks. Narrower perturbations lead to clearer joints. In realistic cases, it could lead to the situation that some of the observed eigenfrequency separates are several times of the other separates during a single time interval due to the elimination of some troughs which lead to the joint of peaks. However, according to the study, the eigenfrequency shifts are not very sensitive to the altitudes and the size of the perturbations. Therefore, the plasma density perturbations could be roughly monitored continuously on the ground according to the eigenfrequency shifts observed by pulsation magnetometers. However, this method is not quite sensitive to the altitudes and the size of the perturbations. It just shows very general and imprecise results of the perturbations.

8.2 Future Tasks

In this thesis, both data interpretation and theoretical study by numerical computations were carried out. Based on the study in this thesis, there could be several works to do in future.

For data interpretations, the plasma density profiles need to be investigated with the eigenfrequency statistical work to see that whether the IAR eigenfrequency shifts occur

simultaneously with the plasma density perturbation. On the other hand, the IAR occurrence in Antarctica needs to be further investigated to find out the factors that make significant contributions in order to explain why the occurrence of the IAR in Antarctica is clearly different from the occurrence in northern hemisphere. For numerical studies, data of artificial heating experiments need to be investigated to compare with the results of the response ratio in Chapter 6. This numerical model could be utilized to study the field line resonance. Furthermore, the relations between IAR eigenfrequency shifts and plasma density profiles need to be further investigated quantitatively. Then the study of the numerical results should be compared with observations.

APPENDIX

A1. Abbreviations

AE: Autumn Equinox

BAS: British Antarctica Survey

DFT: Discrete Fourier Transform

EISCAT: European Incoherent SCATter radar

ESR: EISCAT Svalbard Radar

FT: Fourier Transform

FFT: Fast Fourier Transform

FLR: Field Line Resonance

IAR: Ionospheric Alfvén Resonator

IRI2007: International Reference Ionosphere 2007

KIL: Kilpisjärvi

LHC: Left Hand Circular

LT: Local Time

MHD: MagnetoHydroDynamics

M-I: Magnetosphere-Ionosphere

NUR: Nurmijärvi

OUL: Oulu

RHC: Right Hand Circular

ROV: Rovaniemi

SE: Spring Equinox

SOD: Sodankylä

SPEAR: Space Plasma Exploration by Active Radar

SRS: Spectrum Resonance Structure

TGO: Tromsø Geophysical Observatory

ULF: Ultra Low Frequency

UT: Universal Time

A2. The table list of the IAR dates at Halley Research Station

2005			
097 (7 Apr)			
2006			
049 (18 Feb)	056 (25 Feb)	063 (4 Mar)	
2007			
080 (21 Mar)	280 (7 Oct)	281 (8 Oct)	282 (9 Oct)
2008			
272 (28 Sep)	280 (6 Oct)	281 (7 Oct)	282 (8 Oct)
283 (9 Oct)	295 (21 Oct)		
2009			
050 (19 Feb)	055 (24 Feb)	056 (25 Feb)	060 (1 Mar)
061 (2 Mar)	262 (19 Sep)	263 (20 Sep)	264 (21 Sep)
265 (22 Sep)	266 (23 Sep)	267 (24 Sep)	268 (25 Sep)
274 (1 Oct)	275 (2 Oct)	276 (3 Oct)	277 (4 Oct)
278 (5 Oct)	279 (6 Oct)	284 (11 Oct)	285 (12 Oct)
287 (14 Oct)	289 (16 Oct)	292 (19 Oct)	

A3. Error Estimation of Gaussian Elimination

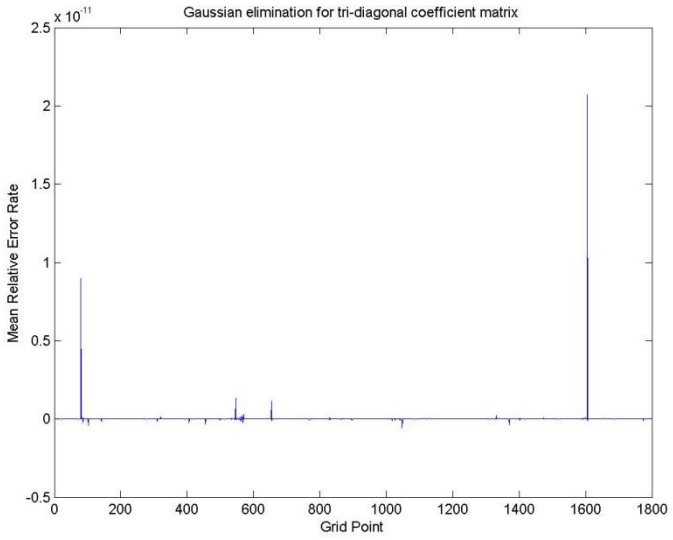

Fig A3.1 The plot shows the mean relative errors of the Gaussian elimination that would be utilized to solve the numerical model introduced in Chapter 5. The y-axis shows the scale of the relative errors. The x-axis shows the grid point.

The left end and the right end of the x-axis are the boundaries of the simulation box. The relative errors close to the boundaries are relatively greater than in the middle of the simulation box. It was caused by the algorithm of the Gaussian elimination. And it should be noticed that the greatest relative error is still smaller than 2.5×10^{-11}. There is no nonlinear process in the model introduced in Chapter 5. Thus the errors caused by the Gaussian elimination could be ignored in the numerical study in this thesis.

A4. Tests on double running average and sinusoidal curve fitting

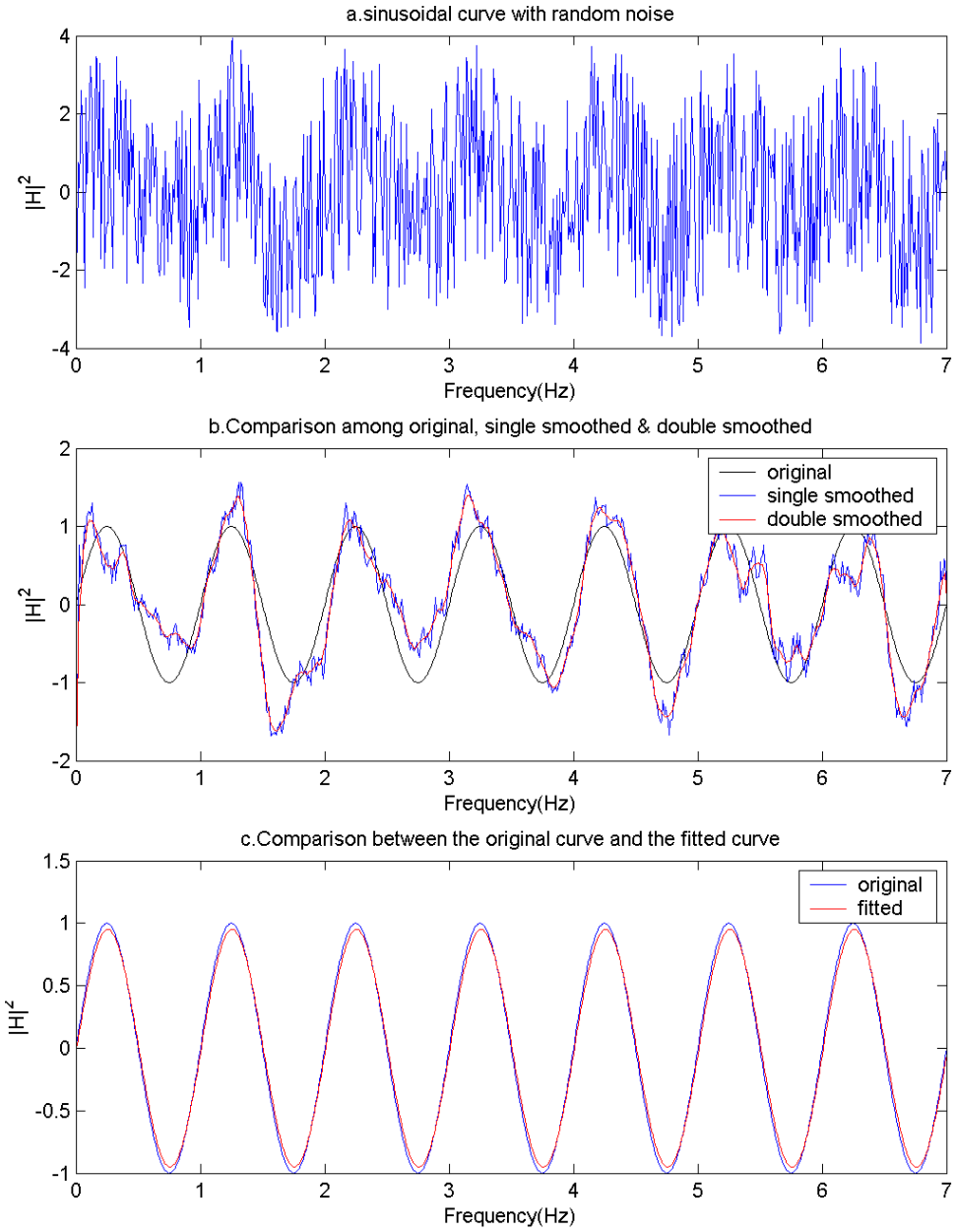

Fig A4. Panel a illustrates a sinusoidal curve with much greater noises. The relation between the sinusoidal curve and the noise is showed in Equation A4.1. Panel b illustrates the original, the single smoothed and the double smoothed curve. Panel c illustrates the original sinusoidal curve which is the first term in Equation A4.1, and the fitted curve by utilizing the sinusoidal curve fitting method.

$$|H^2|=\sin(a*f+2*a)+3R \quad \text{(A4.1)}$$

where $|H^2|$ is the artificially generated power of the magnetic field, f is the frequency, R is the random number between -1 and 1, and a was set to be 2π.

Table A4.1 shows the curve fitting results, which is plotted as the red line in panel c.

Variable	**a**	**R**
Real Value	2π	[-1,1]
Fitted Result	6.283	[-0.983,1.007]

Table A4.1 The real values of the parameters and the values from the curve fitting.

REFERENCE

Alfvén, H. (1942). Existence of electromagnetic-hydrodynamic waves, Nature **150** (3805): 405–406.

Allan, W., A. Wright, and **D. McDiarmid** (1997), Spacecraft transits across simulated field line resonance regions, J. Geophys. Res., 102(A7), 14407-14414.

Belcher, J. W., L. Davis Jr., and **E. J. Smith** (1969), Large-Amplitude Alfvén Waves in the Interplanetary Medium: Mariner 5, J. Geophys. Res., 74(9), 2302–2308

Belyaev, P.P., Polyakov, S.V., Rapoport, V.O., Trakhtengerts, V.Y., (1990). The ionospheric Alfvén resonator, Journal of Atmospheric and Terrestrial Physics 52 (9), 781-788.

Belyaev, P.P., S.V. Polyakov, E.N. Ermakova, S.V. Isaev (2000). Solar cycle variations in the ionospheric Alfvén resonator 1985-1995, Journal of Atmospheric and Solar-Terrestrial Physics 62, 239-248.

Bond, G., Kromer, B., Beer, J., Muscheler, R., Evans, M.N., Showers, W., Hoffmann, S., Lotti-Bond, R., Hajdas, I., Bonani, G. (2001). Persistent solar influence on North Atlantic climate during the Holocene. Science 294, 2130–3136.

Bösinger, T., C. Haldoupis, P. P. Belyaev, M. N. Yakunin, N. V. Semenova, A. G. Demekhov, and V. Angelopoulos, Spectral properties of the ionospheric Alfvén resonator observed at a low-latitude station (L = 1.3), J.Geophys.Res., VOL. 107, NO. A10, 1281.

Boyd, T.J.M. and **J.J.Sanderson** (1969). "PLASMA DYNAMICS", THOMAS NELSON AND SONS LTD., London, pg83

Cattell, C., et al (1998). The association of electrostatic ion cyclotron waves, ion and electron beams and field-aligned currents: FAST observations of an auroral zone crossing near midnight, GEOPHYSICAL RESEARCH LETTERS, VOL. 25, NO. 12, PAGES 2053-2056.

Chaston, C. C., J. W. Bonnell, C. W. Carlson, M. Berthomier, L. M. Peticolas, I. Roth, J. P. McFadden, R. E. Ergun, and R. J. Strangeway (2002), Electron acceleration in the ionospheric Alfvén resonator, J. Geophys. Res., 107(A11), 1413

Chmyrev, V.M. et al, (1988), Alfvén Vortices and Related Phenomena in the Ionosphere and the Magnetosphere, Physica Scripta, Vol. 38, 841-854

Cummings, W. D., R. J. O'Sullivan, and **P. J. Coleman Jr.** (1969), Standing Alfvén Waves in the Magnetosphere, J. Geophys. Res., 74(3), 778–793.

Demekhov, A.G. (2007). Recent progress in understanding Pc1 pearl formation, Journal of Atmospheric and Solar-Terrestrial Physics 69, 1609–1622.

Eliasson, B. (2003). Numerical modelling of the two-dimensional Fourier transformed Vlasov–Maxwell system, Journal of Computational Physics 190 (2003) 501–522.

Ermakova, E.N., P.P. Belyaev, N.I. Belova, V.Yu Trakhtengerts (2000). A sunset effect in variations of the eigenfrequencies of the ionospheric Alfvén resonator, Journal of Atmospheric and Solar-Terrestrial Physics 62, 249-252.

Ermakova, E.N. and **Kotik, D.S.** (2008). A STUDY OF THE LOCAL AND GLOBAL PROPERTIES OF THE SPECTRAL RESONANCE STRUCTURE OF THE ULF MAGNETIC NOISE ON THE BASIS OF MEASUREMENTS IN TWO POINTS SEPARATED MORE THAN 1000 KM, "Physics of Auroral Phenomena", Proc. XXXI Annual Seminar, Apatity, pp. 141- 144.

Goertz, C.K. (1984). KINETIC ALFVÉN WAVES ON AURORAL FIELD LINES, Planer. Space Sci., Vol. 32, No 11, pp. 1387-1392.

Green, C.A. (1984). THE SEMIANNUAL VARIATION IN THE MAGNETIC ACTIVITY INDICES A_a and A_p, Planet. Space Sci., Vol 32, No. 3, pp 297-305.

Grzesiak, M. (2000), Ionospheric Alfvén resonator as seen by Freja satellite, *Geophys. Res. Lett.*, 27(7), 923–926, doi:10.1029/1999GL010747.

Gulyaeva, T.L. and **Gulyaev, R.A.** (1993). Climate change in the ionosphere parameters dependent on solar and geomagnetic activity. Adv. Space Res., Vol.13, No.3, pp(3)63-(3)66

Haigh, J.D. (1996). The impact of solar variability on climate, Science 272, 981-984.

Hebden, S.R., T. R. Robinson, D. M. Wright, el al (2005). A quantitative analysis of the diurnal evolution of Ionospheric Alfvén resonator magnetic resonance features and calculation of changing IAR parameters, Annales Geophysicae, 23, 1711–1721.

Hirose, A. and **Lonngren, K.E.** (1985), "**Introduction to wave phenomena, Wiley-Interscience**", **Chichester, New York, pg95.**

Hysell, D.L., Kudeki, E., and **Chau, J.L.** (2005). Possible ionospheric preconditioning by shear flow leading toequatorial spread F, Annales Geophysicae, 23, 2647–2655.

Kelley, M. C., and **Heelis, R. A.,** "*The Earth's Ionosphere: Plasma Physics and Electrodynamics*". Academic Press, 1989.

Lanzerotti, L.J., Thomson, D.J., and **Maclennan, C.G.** (1997). Wireless at high altitudes--environmental effects on space-based assets, Vol.2, Issue 3

Lastovicka, J., et al. (2008) Emerging pattern of global change in the upper atmosphere and ionosphere. Ann. Geophys., 26, 1255–1268.

Laut, P. (2003). Solar activity and terrestrial climate: an analysis of some purported correlations, Journal of Atmospheric and Solar-Terrestrial Physics 65, 801– 812

Lockwood, M., et al (1993). Ionospheric signatures of pulsed reconnection at the Earth's magnetopause, Nature, 361 (6411), 424-428.

Lysak, R. (1988). Theory of Auroral Zone PiB Pulsation Spectra, J. Geophys. Res., 93(A6), 5942-5946.

Lysak, R. (1991). Feedback Instability of the Ionospheric Resonant Cavity, J. Geophys. Res., 96(A2), 1553-1568.

Lysak, R. L., and Y. Song (2008), Propagation of kinetic Alfvén waves in the ionospheric Alfvén resonator in the presence of density cavities, Geophys. Res. Lett., 35, L20101, doi:10.1029/2008GL035728.

Matsumoto, H. and **Omura, Y** (Eds.) (1993). "Computer Space Plasma Physics: Simulation

Techniques and Software", Terra Scientific Pub. Co., Tokyo.

Mathews, J.H. (1987). "**Numerical methods for mathematics, science, and engineering**", **Prentice Hall International, pg452.**

Molchanov, O.A., De Franceschi, G., Gulyaeva, T.L., L Perrone, L. and **Zolesi, B.** (2004). Ionospheric Alfvén resonance at middle latitudes: results of observations at Kamchatka, Physics and Chemistry of the Earth 29, 649–655.

Mursula, K. , Prikner, K., Feygin, F.Z., et al (2000) Non-stationary Alfvén resonator: new results on Pc1 pearls and IPDP events, Journal of Atmospheric and Solar-Terrestrial Physics 62, 299-309.

Odzimek, A., A. Kułak, A. Michalec, and **J. Kubisz** (2006). An automatic method to determine the frequency scale of the ionospheric Alfvén resonator using data from Hylaty station, Poland, Ann. Geophys., 24, 2151–2158.

Orlowski, D., C. Russell, and **R. Lepping** (1992), Wave Phenomena in the Upstream Region of Saturn, J. Geophys. Res., 97(A12), 19187-19199.

Pang, Y., Y. Lin, X. H. Deng, X. Y. Wang, and B. Tan (2010), Three-dimensional hybrid simulation of magnetosheath reconnection under northward and southward interplanetary magnetic field, J. Geophys. Res., 115.

Parent, A., I. R. Mann, and **I. J. Rae** (2010), Effects of substorm dynamics on magnetic signatures of the ionospheric Alfvén resonator, J. Geophys. Res., 115, A02312

Pokhotelov, O., D. Pokhotelov, A. Streltsov, V. Khruschev, and **M. Parrot** (2000), Dispersive ionospheric Alfvén resonator, J. Geophys. Res., 105(A4), 7737-7746.

Polyakov, S.V. and **Rapoport, V.O.**, (1976). On the properties of the ionospheric Alfvén resonator, KAPG Symposium on Solar-Terr phys., 3, Nauka, Moscow, 72-73.

Prikner, K., Mursula, K., Kangas, J., Kerttula, R., Feygin, F.Z., (2004). An effect of the ionospheric Alfve′n resonator on multiband Pc1 pulsations. Annales de Geophysicae 22, 643–651.

Prikner, K., Mursula, K., Bosinger, T., Feygin, F.Z., Raita, T. (2007). The effective altitude range of the ionospheric Alfvén resonatorstudied by high-altitude EISCAT

measurements, Journal of Atmospheric and Solar-Terrestrial Physics 69 (2007) 1657–1667.

Robinson, T.R., et al (2000). FAST observations of ULF waves injected into the magnetosphere by means of modulated RF heating of the auroral electrojet, GEOPHYSICAL RESEARCH LETTERS, VOL. 27, NO. 19, PAGES 3165-3168.

Russell, C., and **R. McPherron** (1973). Semiannual Variation of Geomagnetic Activity, J. Geophys. Res., 78(1), 92-108.

Sangalli, L., D. J. Knudsen, M. F. Larsen, T. Zhan, R. F. Pfaff, and D. Rowland (2009). Rocket-based measurements of ion velocity, neutral wind, and electric field in the collisional transition region of the auroral ionosphere, J. Geophys. Res., 114.

Scoffield, H. C. , T. K. Yeoman, T. R. Robinson, L. J. Baddeley, R. S. Dhillon, D. M. Wright, T. Raita, and T. Turunen (2006), First results of artificial stimulation of the ionospheric Alfvén resonator at 78°N, *Geophys. Res. Lett.*, 33, L19103, doi:10.1029/2006GL027384.

Semenova, N.V. and **Yahnin, A.G.** (2008). Diurnal behaviour of the ionospheric Alfvén resonator signatures as observed at high latitude observatory Barentsburg (L=15), Ann. Geophys., 26, 2245–2251.

Shalimov, S. and **T. Bösinger** (2008), On distant excitation of the ionospheric Alfvén resonator by positive cloud-to-ground lightning discharges, J. Geophys. Res., 113.

Shimazaki, T. (1962). A Statistical Study of Occurrence Probability of Spread F at High Latitudes, J. Geophys. Res., 67(12), 4617-4634.

Shukla, P.K. and Eliasson, B. (2003). Trapping of Plasmons in Ion Holes, JETP Letters, **77**(12), pp. 647-652.

Song, P., H. Singer and **G. Siscoe** (Eds) (2001). "Space weather effects on technologies, in Space Weather", American Geophysical Union, Washington, pg11

Steel, R. G. D. and **Torrie, J. H.,** *Principles and Procedures of Statistics,* New York: McGraw-Hill, 1960, pp. 187, 287.

Streltsov, A. V. and W. Lotko (2004), Multiscale electrodynamics of the ionosphere-magnetosphere system, J. Geophys. Res., 109, A09214.

Surkov, V. V., M. Hayakawa, A. Y. Schekotov, E. N. Fedorov, and O. A. Molchanov (2006), Ionospheric Alfvén resonator excitation due to nearby thunderstorms, J. Geophys. Res., 111.

Trakhtengerts, V.Y., Feldstein, A.Y. (1981). Influence of Alfvén velocity inhomogeneous profile on magnetospheric convection stratification. Geomagnetism and Aeronomy, 21, 951-953.

Trakhtengerts, V.Y., et al. (2000a). Excitation of Alfvén waves and vortices in the ionospheric Alfvén resonator by modulated powerful radio waves, Journal of Atmospheric and Solar-Terrestrial Physics, 62, 267-276.

Trakhtengerts, V.Y., et al. (2000b). A mechanism of anticorrelation in the occurrence of ULF electromagnetic noise resonance structure and Pc 1 magnetic pulsations through the solar activity cycle, Journal of Atmospheric and Solar-Terrestrial Physics, 62, 253-256.

Velli, M. and **Pruneti, F.** (1997). Alfvén waves in the solar corona and solar wind, Plasma Phys. Control. Fusion 39, B317–B324.

Yeoman, T.K., H.C. Scoffield, D.M. Wright, L.J. Baddeley, A.N. Vasilyev, N.V. Semenova. (2008), Investigation of natural and artificial stimulation of the ionospheric Alfvén resonator at high latitude, Advances in Space Research, Volume 42, Issue 5, Pages 957-963, ISSN 0273-1177, DOI: 10.1016/j.asr.2007.03.083.